Photometric and Spectroscopic Properties of Void Galaxies in the Sloan Digital Sky Survey

A Thesis

Submitted to the Faculty

of

Drexel University

by

Randall R. Rojas

in partial fulfillment of the

requirements for the degree

of

Doctor of Philosophy

March 2004

Dedication

I dedicate this thesis to my mother, Arelys Rojas, for all her hard work in my upbringing. Her love, efforts, support, and encouragement made this thesis possible. I will always be grateful to her for her guidance and dedication with which she raised me. *Mami, un millón de gracias, te amo!*

Acknowledgments

This is perhaps the most difficult part of the thesis because so many people have contributed in so many ways that proper acknowledgment would require a substantial amount of documenting and thinking back. Nevertheless, I will do my best to give proper credit to everyone but do apologize if I missed anyone.

I must first thank my advisor, Michael S. Vogeley who's high expectations, sharp thinking, and thought provoking questions brought out the best in me. I am eternally grateful to him for giving me the opportunity and honor to work under his supervision, and for the support he provided all throughout my graduate career. His genuine interest in the subject inspired me to carry out this work and instilled in me a greater appreciation for astrophysics. Under his supervision I matured as a researcher, learned more astrophysics than I thought I would, and experienced science at a whole new level.

I thank Fiona Hoyle (Dr. Inventa) for being a wonderful mentor and above all a great friend. Since the days of the vino-trio to the present she has helped me in both the academics and personal sanity by answering all my endless Fortran (I'll never forget to use `implicit none`) and astronomy questions and providing endless amounts of entertainment all these years. I'll definitely miss her vivid personality and British humor. In the end I still owe you gtrilions of pints!

I would also like to thank Ernest N. Mamikonyan (Ernie) and Jimin Gao for the countless times they helped me with my computer problems. Their help allowed me

to concentrate on my work rather than being consumed for hours sorting out my computer problems. The astro group certainly deserves special recognition for providing the intellectual atmosphere that complemented the development of my understanding of astrophysics. Thanks to our weekly 'astro tea talks', I filled many gaps in my understanding. However, my training would not have been complete without the help from Dave Goldberg and Steve McMillan who where always available to answer my questions and provided many useful conversations.

My efforts and accomplishments would not have been possible without the support, encouragement, and love of my family. I thank my parents, Arelys and Rodrigo, for believing in me and encouraging me to pursue my intellectual flights of fancy. My brother in law and sister, John and Vanessa, have definitely been influential in my success. I thank them both for always being there when I needed them and taking care of me in every way they could. Vane, you have been like a second mother to me, and John, you have gone beyond the call of duty. I am really grateful for everything you have done for me. John, now we get to catch up on six years of drinking and chess playing, and Vane, get ready for grad school.

Janelle deserves special recognition and several awards for not only enduring our almost 6 years apart but also for supporting me in every way. She provided the motivation I needed to finish and made all my efforts worth while. Now that I am at the end of this journey I look forward to the beginning of a great future by her side. 'Pelota', you are the best! To her family, Don Raimundo, Doña Caridad, and Vicky and I am grateful for their sincere concern of my well being and help they provided in so many ways all these years.

I also wish to thank Toño and Doña Flor for the intellectual guidance they provided early on in my career. Their help and support made a great difference in my life. Finally, I thank Elgir Saborío (Maicero) who's intellectual curiosity and friendship led me to pursue a career in physics. Without our philosophical conversations and frequent experiments my interest in science would never have developed.

Table of Contents

List of Tables

List of Figures

Abstract

Photometric and Spectroscopic Properties of Void Galaxies in the Sloan Digital Sky Survey

Randall R. Rojas

Michael S. Vogeley, Ph.D.

Using a nearest neighbor analysis, we construct a sample of void galaxies from the Sloan Digital Sky Survey (SDSS) and compare the photometric and spectroscopic properties of these galaxies to the population of non-void (wall) galaxies. We trace the density field of galaxies using a volume-limited sample with $z_{max} = 0.089$. Galaxies from the flux-limited SDSS with $z \leq z_{max}$ and fewer than three volume-limited neighbors within $7h^{-1}$Mpc are classified as void galaxies. This criterion implies a density contrast $\delta\rho/\rho < -0.6$ around void galaxies. From 155,000 galaxies, we obtain a sub-sample of 13,742 galaxies with $z \leq z_{max}$, from which we identify 1,010 galaxies as void galaxies. To identify an additional 194 faint void galaxies from the SDSS in the nearby universe, $r \lesssim 72h^{-1}$Mpc, we employ volume-limited samples extracted from the Updated Zwicky Catalog and the Southern Sky Redshift Survey with $z_{max} = 0.025$ to trace the galaxy distribution. Our void galaxies span a range of absolute magnitude from $M_r = -13.5$ to $M_r = -22.5$. Using SDSS photometry, we compare the colors, concentration indices, and Sersic indices of the void and wall samples. Void galaxies are on average significantly bluer than galaxies lying at higher densities. The population of void galaxies with $M_r \lesssim M^* + 1$ and brighter is on average bluer and more concentrated (later type) than galaxies outside of voids. The latter behavior is only partly explained by the paucity of luminous red galaxies

in voids. These results generally agree with the predictions of semi-analytic models for galaxy formation in cold dark matter models, which indicate that void galaxies should be relatively bluer, more disklike, and have higher specific star formation rates. Analysis of their spectroscopic properties confirms that void galaxies have a higher specific star formation rate than wall galaxies and although they have comparable metallicities to galaxies in higher density regions, there is a deficiency of metal-poor galaxies in dense environments (Hao et al. 2003). From the luminosity function (LF) of void galaxies (Hoyle et al. 2003) we infer that voids are not filled with a large population of dwarf galaxies based on the similarities of the faint end slopes of void and wall galaxy LFs. In addition, the fainter value of M_r^* for void galaxies is consistent with our analysis of their photometric properties. Our results show that void galaxies differ from wall galaxies in most of the properties under consideration with a high statistical significance. This seems to indicate that void galaxies do occupy a special region of the parameter space manifold of galaxy properties.

Chapter 1: Introduction

1.1 Why Study the Most Underdense Regions?

Voids are the most prominent feature in the large-scale distribution of matter in the universe. A typical void is about $30h^{-1}$Mpc in diameter, has a density contrast of $\delta = -0.9$ and they occupy about 40% of the total volume of the universe. Since the discovery of the void in Boötes (Kirshner et al. 1981), with a diameter of $50h^{-1}$Mpc, and subsequent discoveries of voids in larger redshift surveys (Geller & Huchra 1989; Pellegrini, da Costa & de Carvalho 1989; da Costa et al. 1994; Shectman et al. 1996; El-Ad, Piran & da Costa 1996, 1997; Müller et al. 2000; Plionis & Basilakos 2002; Hoyle & Vogeley 2002), these structures have posed an observational and theoretical challenge. Because the characteristic scale of large voids was comparable to the depth of early redshift surveys, few independent structures were detected, making statistical analysis of their properties difficult. Likewise, the limitations of computing technology constrained early cosmological simulations to include only a few voids per simulation.

One of the primary goals of the study of void galaxies is to determine whether void galaxies are fundamentally different from galaxies in denser environments. Recent studies of the photometric properties of void galaxies (Grogin & Geller 1999, 2000;

Rojas et al. 2003) have demonstrated that there are significant differences between void and non-void galaxies. However, much needed complementary spectroscopic studies of void galaxies have been hindered by the lack of large and homogeneous samples of void galaxies and high signal-to-noise spectroscopic observations. Recent advances in void finding algorithms and the quality of large redshift surveys have made it possible to probe many independent voids (SSRS2; El-Ad & Piran 1997, PSCz and UZC; Hoyle & Vogeley 2002, 2dFGRS; Hoyle & Vogeley 2003, SDSS; Hoyle & Vogeley 2004) and identify larger samples of void galaxies. At the present our sample of more than 10^3 void galaxies from the SDSS provides an excellent testbed for gauging the spectroscopic and photometric properties of galaxies in underdense regions.

Careful examination of the matter content in underdense environments can help clarify the apparent discrepancy between current Cold Dark Matter (CDM) model predictions and observations. Voids in the real universe appear to contain less structure than voids in the CDM scenario (Dekel & Silk 1986; Hoffman, Silk & Wyse 1992). CDM predicts many dark matter halos inside voids (Klypin et al. 1999a; Moore et al. 1999; Gottlöber et al. 2003), yet observations do not support these predictions. According to Peebles, (2001) "the apparent inconsistency between the theory and observations of voids is striking enough to be classified as a crisis for the CDM model". This *crisis* has lead to the development of alternative models such as the warm dark matter (WDM) scenario (Bode, Ostriker, & Turok, 2000). We may discover that a substantial fraction of dark matter resides well inside the voids. If so, the implications would significantly change the course of our search for dark matter. It would suggest that galaxies are not fair tracers of matter and it would constrain competing cosmo-

logical models of structure formation. Despite the success that previous studies have achieved in studying underdense environments many unresolved issues still remain to be addressed. For example, the 'Void Phenomena' (Peebles 2001) i.e., the fact that both gas clouds and ordinary galaxies of different morphologies seem to respect the interior of voids is still an open and important problem in cosmology.

In models of hierarchical galaxy formation, it is assumed that galaxies form as a bottom-up process. First, small galaxies form, then they merge together and over time form the large galaxies we see today. It is also assumed that the initial density fluctuations that give rise to galaxies are Gaussian and adiabatic. Therefore, the evolution of structure is due to gravitational instability. In low density environments like voids, matter evacuates these regions and flows out towards higher density regions where some of it eventually collapses to form galaxies. Thus, galaxies found in clusters and filamentary regions will probably have undergone many mergers, or at the very least been harassed by neighboring galaxies. This merging process disrupts the flow of gas and can squelch star formation (Benson et al. 2002). Over time, voids grow and become emptier, therefore, the dark matter halos had to form at early times before the void expands and matter flows out. Because of this, one expects the properties of void galaxies to be different from galaxies elsewhere, especially given that the dark matter halo mass functions in voids is different. Since interactions between galaxies in voids are rare the properties of void galaxies may reflect those of the primeval galaxies. Verde et al. (2002) show that L^* galaxies are fair tracers of mass clustering (i.e., the bias, $b = \delta_{\rm galaxies}/\delta_{matter}$ is close to unity) and Blanton et al. (1999) show that young galaxies are not as highly biased ($b < b_{L^*}$) as older galaxies at all scales.

In addition, observations of different types of galaxies show that late-type galaxies are biased relative to early-type galaxies. However, currently it is not well understood where void galaxies fit in this picture. If galaxies are not biased tracers of the mass distribution then L^* galaxies in voids (which are fainter) might trace the mass inside them, i.e., L^* void galaxies may trace the distribution of mass in voids.

Observed properties of void galaxies are being confirmed by Semi-Analytical Models (Benson et al. 2002; Mathis & White 2002) and theoretical work on the initial conditions for running large N-body simulations inside voids (Goldberg & Vogeley, 2003; Gottlöber et al. 2003) are opening the doors to a new era of cosmological simulations. However, both theory and experiment rely on detailed observations of different environments and quantitative assessment of their contents. Until now the small samples of void galaxies available did not lend themselves to reliable quantitative results, let alone comparisons between void and non-void galaxies of similar luminosities and morphological types. Whether the morphology-SFR and morphology-density relation are independent still remains inconclusive. Detailed comparisons of the properties of void and non-void galaxies can help explain the mechanisms by which galaxies lose gas. Currently these mechanisms are not implemented in models of hierarchical galaxy formation (White & Frenk 1991; Kauffmann et al. 1993; Heyl et al. 1995; Baugh, Cole & Frenk 1996a,b; Somerville & Primack 1999; Cole et al. 2000; Kauffmann et al. 2004). Proposed mechanisms for different environments include ram-pressure stripping (Gun & Gott 1972; Abadi et al. 1999; Quilis et al. 2000), harassment (Moore et al. 1996a; Moore et al. 1999), and tidal disruption (Byrd & Valtonen 1990) in rich environments and halo gas stripping (Larson et al. 1980; Balogh et al. 2000; Diaferio

et al. 2001) and low-velocity interactions (Mihos & Hernquist 1996) for poor systems.

The role that environment plays on the properties of galaxies has been given careful consideration since the influential work of Dressler (1980) and subsequent studies by Postman & Geller (1984), Zabludoff & Mulchaey (1998), Tran et al. (2001), and, Dominguez et al. (2001) among others. It has been well established that red early-type galaxies are more common in dense regions and blue late-type galaxies in less dense regions. Many studies have also shown that there is a strong dependence of star formation on environment. High star formation rates (SFR) are usually found in low density environments while lower SFRs are more commonly seen in higher density regions. (Dressler, Thompson & Shectman 1985; Couch & Sharples 1987; Balogh et al. 1997, 1998, 1999, 2002a; Hashimoto et al. 1998; Poggianti et al. 1999; Couch et al. 2001; Solanes et al. 2001; Lewis at al. 2002a; Gomez et al. 2002).

However, only recently was it possible to show that there is a strong dependence of SFR on local galaxy density in large enough samples to include a fair mix of morphological types. Gomez et al. 2002, using a volume-limited sample from the SDSS Early Data Release (EDR), showed that there is a decrease in SFR from galaxies in the field to galaxies in denser environments (e.g. in rich clusters). Independently, Lewis et al. (2002a) in the 2dF Galaxy Redshift Survey found the same strong correlation between environment and SFRs. In the Las Campanas Redshift Survey, Hashimoto et al. (1998) noticed that regardless of the concentration index, galaxies in clusters have on average lower SFRs than field galaxies.

Tremendous efforts in extrapolating the *density-sfr* relation (Gomez et al. 2002) down to lower densities have met with success. However, none have been able to probe

the very low densities that we examine in this work since very large surveys are needed to yield enough void galaxies. Balogh et al. 2003 show that Hα emission has a strong dependence on local density and revealed that the brightest isolated galaxies have either weak or no Hα emission at all. They also concluded that on average isolated galaxies have SFRs similar to galaxies in more common environments. Gomez et al. 2002 show that considerable differences exist between star-forming (H$\alpha > 5$Å) late-type galaxies in dense regions and similar galaxies in the field. Tanaka et al. (2003), using the $g-i$ color and Hα equivalent width as star formation indicators, show that in the low density regions faint galaxies are more actively forming stars than bright galaxies. They also noticed that for faint galaxies the $g-i$ and Hα equivalent width distributions as a function of local density show a prominent break in surface density at $\log\Sigma_{\rm crit} \sim 0.4\,{\rm galaxies\,h_{75}^{2}Mpc^{-2}}$.

In this work we are able to probe lower density environments (beyond field galaxies) and fainter absolute magnitudes than previous works . Our large sample of more than 10^3 void galaxies has a density contrast of $\delta\rho/\rho < -0.6$ and spans a broad range of absolute magnitude from $M_r = -13.5$ to $M_r = -22.5$. Therefore, this sample allows us to quantitatively extend the study of star formation history down to the lowest densities possible and compare the spectroscopic and photometric properties of our void galaxies with non-void galaxies of similar luminosities and surface brightness profiles. These comparisons are crucial in order to constrain models of galaxy formation and evolution.

Chapter 2: The Data

The search for void galaxies requires a large 3-dimensional map of the galaxy density field. We extract a volume-limited sample (see Figure 2.1)from the SDSS data to map the galaxy density field and look for void galaxies in the full magnitude-limited (see Figure 2.2) sample. As the SDSS currently has a slice-like geometry, with each slice only $\sim 6^\circ$ thick, large voids of radius $\sim 10h^{-1}$Mpc ($h \equiv H_o/100$km s^{-1}Mpc^{-1}) can only be detected at comoving distances of $r \gtrsim 10^2 h^{-1}$Mpc using the SDSS data alone. Therefore, to trace the local voids, we also extract a volume-limited sample from the combined Updated Zwicky Catalog (UZC; Falco et al. 1999) and Southern Sky Redshift Survey (SSRS2; da Costa et al. 1998). It should be noted that nearby void galaxies are not selected from the UZC and SSRS2 surveys. These surveys are only used to define the density field around SDSS galaxies that lie at distances $r \leq 72h^{-1}$Mpc.

To recap, we have two volume-limited samples, one from the SDSS and one from the combined UZC+SSRS2. These samples are used to define the galaxy density field only. Void galaxies are found from the magnitude-limited SDSS sample. We define the Distant sample to be the SDSS magnitude-limited sample truncated at $100 \leq r \leq 260h^{-1}$Mpc. The Nearby sample is the SDSS magnitude-limited sample

truncated at $r = 72h^{-1}$Mpc. Both magnitude-limited samples (Nearby and Distant) are constructed using the SDSS r-band. In this section we describe each of the surveys and samples in detail.

2.1 The Sloan Digital Sky Survey

The SDSS is a wide-field photometric and spectroscopic survey. The completed survey will cover approximately 10^4 square degrees. CCD imaging of 10^8 galaxies in five colors and follow-up spectroscopy of 10^6 galaxies with $r < 17.77$ will be obtained. York et al. (2000) provides an overview of the SDSS and Stoughton et al. (2002) describes the early data release (EDR) and details about the photometric and spectroscopic measurements made from the data. Abazajian et al. (2003) describes the First Data Release (DR1) of the SDSS. Technical articles providing details of the SDSS include descriptions of the photometric camera (Gunn 1998), photometric analysis (Lupton et al. 2002), the photometric system (Fukugita et al. 1996; Smith et al. 2002), the photometric monitor (Hogg et al. 2001), astrometric calibration (Pier et al. 2002), selection of the galaxy spectroscopic samples (Strauss et al. 2002; Eisenstein et al. 2001), and spectroscopic tiling (Blanton et al. 2001). A thorough analysis of possible systematic uncertainties in the galaxy samples is described in Scranton et al. (2002). The spectra are obtained with two fiber-fed spectrographs. Each fiber subtends $3''$ on the sky and the spectra covers the rest-frame wavelength range from $\sim$ 3500 to 8500Å at the median redshift. With the 45 minute exposure time, 640 spectra are obtained with high signal-to-noise ($\lambda/\Delta\lambda \sim 2000$).

We examine a sample of 155,126 SDSS galaxies (Blanton et al. 2002; `sample10`) that have both completed imaging and spectroscopy. The area observed by `sample10` is approximately 1.5 times that of the DR1 (Abazajian et al. 2003). To a good approximation, the sample we analyze consists of roughly three regions covering a total angular area of 1,986 deg^2. Due to the complicated geometry of the SDSS sky coverage, the survey regions are best described in the SDSS coordinate system (see Stoughton et al. 2002 and Appendix C for details). Where possible in this section we describe approximate limits in the more familiar equatorial coordinates. The first region is an equatorial stripe in the North Galactic Cap (NGC). This stripe has a maximum extent of 7.5° in the declination direction over the R.A. range $21^{\rm h}30^{\rm m} \lesssim \alpha \lesssim 4^{\rm h}10^{\rm m}$ and maximum length of 120° over the R.A. range $8^{\rm h} \lesssim \alpha \lesssim 16^{\rm h}$. The second region is in the South Galactic Cap (SGC). There are three stripes, the boundaries of which are defined in the SDSS coordinate system. Each stripe is 2.5° wide in SDSS survey coordinates. One stripe is centered at $\delta = 0°$ and covers the R.A. range $20^{\rm h}40^{\rm m} \lesssim \alpha \lesssim 2^{\rm h}20^{\rm m}$. The other two stripes are above and below the equator and cover similar R.A. ranges. In survey coordinates these two stripes cover the range $-28° \lesssim \lambda \lesssim 41°$, $130° \lesssim \eta \lesssim 135°$ and $-57° \lesssim \lambda \lesssim 58°$, $155° \lesssim \eta \lesssim 160°$. The third large region is in the North Galactic Cap. In SDSS survey coordinates it covers the range $-48° \lesssim \lambda \lesssim 50°$, $75° \lesssim \eta \lesssim 85°$. There are additional smaller stripes at $-37° \lesssim \lambda \lesssim -22°$, $60° \lesssim \eta \lesssim 70°$ and $2° \lesssim \lambda \lesssim 60°$, $90° \lesssim \eta \lesssim 100°$ (the boundary is an approximation because of the tiling geometry).

We correct the velocities of galaxies to the Local Group frame according to

$$\Delta v = V_{\rm apex}[\sin(b)\sin(b_{\rm apex}) + \cos(b)\cos(b_{\rm apex})\cos(l - l_{\rm apex})] \tag{2.1}$$

where $l_{\rm apex} = 93°$, $b_{\rm apex} = -4°$, and $V_{\rm apex} = 316\,{\rm km\,s^{-1}}$ (Karachentsev & Makarov 1996). The magnitudes of the galaxies are K-corrected as described in Blanton et al. (2003) and corrections for Galactic extinction are made using the Schlegel, Finkbeiner, & Davis (1998) dust maps. Finally, to convert redshifts into comoving distances we adopt an $(\Omega_{\rm m}, \Omega_\Lambda) = (0.3, 0.7)$ cosmology.

The decrease of observed galaxy density with distance in an apparent magnitude-limited galaxy sample might cause us to erroneously detect more voids at large distances. Therefore, we use a volume-limited sub-sample of the SDSS to define the density field of galaxies. This sample consists of galaxies with redshifts less than the redshift limit, z_{max}, and SDSS r-band absolute magnitudes brighter than $M_{\rm crit}$, where

$$M_{\rm crit} = r_{\rm lim} - 25 - 5{\rm log}_{10}[d_l({\rm z_{max}})] \tag{2.2}$$

$r_{\rm lim}$[1], is the magnitude limit of the survey and d_l, is the luminosity distance in units of h^{-1}Mpc at $\rm z_{max}$. We form a volume-limited sample of the SDSS with $\rm z_{max} = 0.089$, with corresponding absolute-magnitude limit $M_{\rm crit} = -19.87$ (in the SDSS r-band). The redshift limit $\rm z_{max} = 0.089$ allows us to construct the largest possible volume-

[1]We use $r_{\rm lim} = 17.5$ instead of $r_{\rm lim} = 17.77$, in the construction of volume-limited catalog to ensure we have a uniform limit across all the data since earlier stripes were only observed to $r_{\rm lim} = 17.5$.

limited sample from the current SDSS sample. This volume-limited sample contains 22,866 galaxies where the mean separation between these galaxies is $\sim 5.3h^{-1}$Mpc. For a ($\Omega_{\rm m} = 0.3, \Omega_\Lambda = 0.7$) cosmology, the redshift limit of $z_{\rm max}$=0.089, corresponds to a comoving distance of $260h^{-1}$Mpc. The lower bound of $100h^{-1}$Mpc on the comoving distance is necessary due to the slice-like geometry of the early SDSS slices. Recall that voids of radii $\gtrsim 10h^{-1}$Mpc can only be found at $r \gtrsim 100h^{-1}$Mpc as discussed in Section 2.

2.2 The Updated Zwicky Catalog

The Updated Zwicky Catalog (Falco et al. 1999) includes a re-analysis of data taken from the Zwicky Catalog and Center for Astrophysics surveys (Zwicky et al. 1961-1968; Geller & Huchra 1989; Huchra et al. 1990; Huchra, Geller, & Corwin 1995; Huchra, Vogeley, & Geller 1999) together with new spectroscopic redshifts for some galaxies and coordinates from the digitized POSS-II plates. Improvements over the previous catalogs include estimates of the accuracy of the CfA redshifts and uniformly accurate coordinates at the $< 2''$ level.

The UZC contains 19,369 galaxies. Of the objects with limiting apparent magnitude $m_{\rm Zw} \leq 15.5$, 96% have measured redshifts, giving a total number of 18,633 objects. The catalog covers two main survey regions: $8^h < \alpha_{1950} < 17^h, 8.5^\circ < \delta_{1950} < 44.5^\circ$ in the North Galactic Cap and $20^h < \alpha_{1950} < 4^h, -2.5^\circ < \delta_{1950} < 48^\circ$ in the South Galactic Cap. We correct the velocities of the galaxies with respect to the Local Group as discussed in Section 2.1. The magnitudes of the galaxies are corrected

for Galactic extinction using the Schlegel, Finkbeiner & Davis (1998) dust maps and the magnitudes are K-corrected assuming $K = 3$, which is appropriate for the B filter and the median galaxy morphological type Sab (Park et al. 1994; Pence 1976; Efstathiou, Ellis & Peterson 1988).

We construct a volume-limited UZC sample with $z_{max} = 0.025$ since this is the redshift at which the largest volume-limited sample can be obtained. This volume-limited sample contains 4924 galaxies, has a co-moving depth of $\sim 76h^{-1}$Mpc and absolute-magnitude limit of $M_{lim} \leq -18.96$ (B_{Zw}). To compare this limit to that of the SDSS, we translate a B-band magnitude into an approximate r-band magnitude of $M_r = -20.06$ using $g - r = 0.66$ and $g - B = -0.45$ from Fukugita et al. (1995). The absolute magnitude limit of the UZC sample is therefore, slightly brighter than the SDSS limit. To ensure that this sample and the SSRS2 described below are equally deep, we cut back this sample to $r \leq 72h^{-1}$Mpc with the same absolute magnitude limit $M_{lim} = -18.96$.

2.3 The Southern Sky Redshift Survey

The SSRS2 galaxy sample (da Costa et al. 1998) was selected from the list of nonstellar objects in the Hubble Space Telescope Guide Star Catalog (GSC). The SSRS2 contains 3489 galaxies in the SGC over the angular region: $\delta_{1950} \leq -2.5°$ and $b \leq -40°$, covering a total of 1.13 sr with $m_{SSRS2} \leq 15.5$, where the zero-point offset from the Zwicky magnitude system used in the UZC is approximately $m_{SSRS2} - m_{Zwicky} \sim 0.10$ mag (Alonso et al. 1994).

We construct a volume-limited sample with the same redshift limit as for the UZC, $z_{max} = 0.025$ (same reason as discussed in Section 2.2) and (after adjustment of the zeropoint), $M \leq -18.96$. For our chosen cosmology, the depth of the sample is $\sim 73h^{-1}$Mpc which we also cut back to $72h^{-1}$Mpc as discussed in the case for the UZC sample. Therefore, both SSRS2 and UZC volume-limited samples have the same co-moving depth.

As above (Section 2.1), we correct galaxy velocities to the Local Group frame, apply the Galactic dust corrections based on the Schlegel, Finkbeiner, & Davis (1998) dust maps, and assume $K = 3$ to K-correct the observed magnitudes. This volume-limited sample includes 725 galaxies.

The SSRS2 provides angular coverage in the South Galactic Cap. The combined UZC+SSRS2 sample contains 5649 galaxies and sky coverage of ~ 4.25 sr.

2.4 Summary of Surveys

In Figure 2.3 we show an Aitoff projection of the three surveys. The black points show the SDSS galaxies and the gray dots show the UZC+SSRS2 galaxies. This figure demonstrates that in terms of area, the SDSS is almost totally embedded in the UZC+SSRS2 data apart from along the bottom edge of the northern equatorial slice and a small part of the southern most slice. Therefore, the combined UZC+SSRS2 survey is useful for defining the large-scale galaxy density field around the SDSS sample out to a distance of approximately $72h^{-1}$Mpc.

Figure 2.4 shows a cone diagram of the SDSS data with $|\delta| \lesssim 15°$. The inner

circle is drawn at $72h^{-1}$Mpc, which is the co-moving depth of the combined UZC and SSRS2 volume-limited sample. The outer circle is drawn at $260h^{-1}$Mpc, which is the co-moving depth of the SDSS volume-limited sample. Far beyond $72h^{-1}$Mpc, the selection function (number of observed galaxy density with distance) of these shallower surveys drops and the thickness (in the declination direction) of the SDSS itself is adequate to define the density field around the SDSS galaxies.

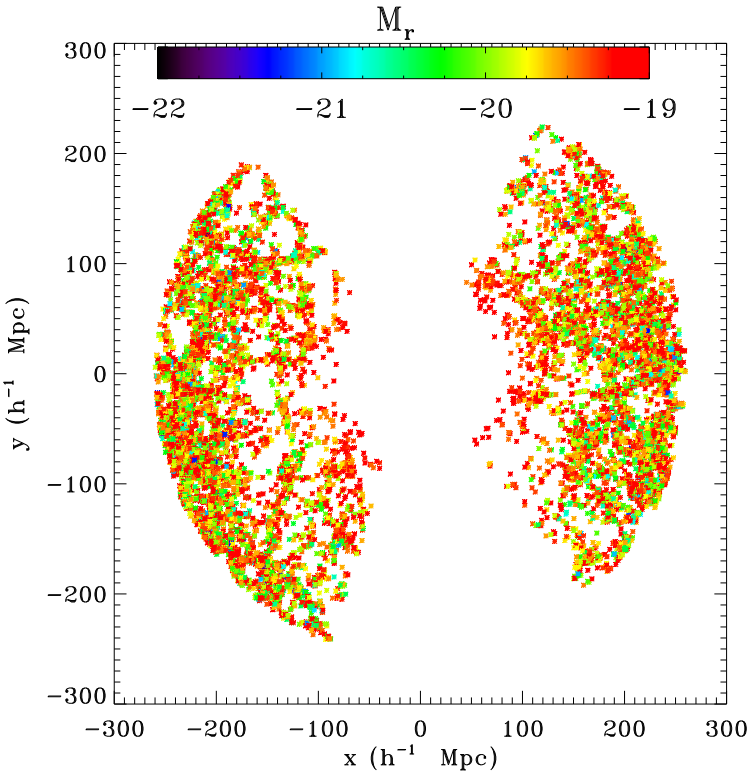

Figure 2.1: Two-dimensional projection of the volume-limited SDSS data with $|\delta| \lesssim 15°$. This sample is complete to $z_{max} = 0.089$, with corresponding absolute-magnitude limit $M_{crit} = -19.87$ (in the SDSS r-band).

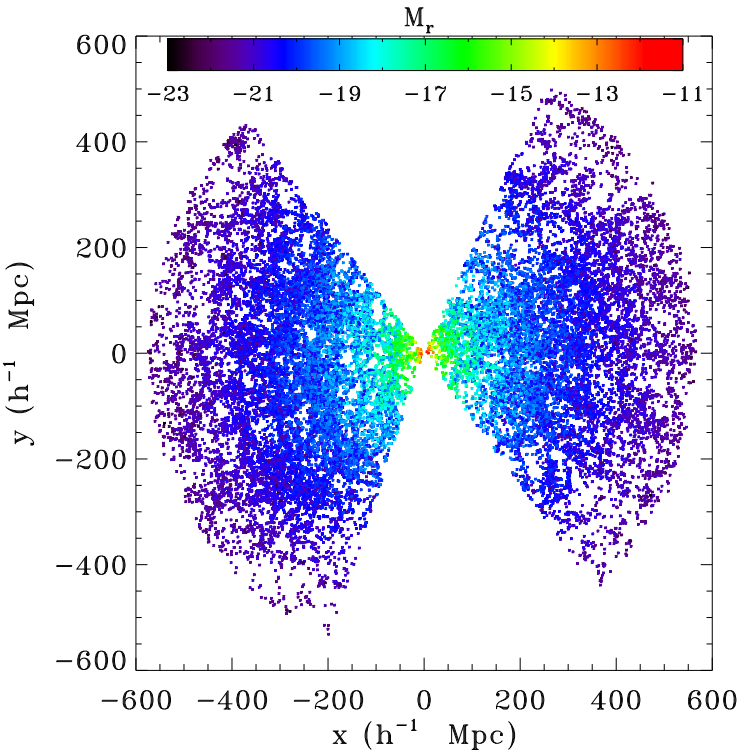

Figure 2.2: Two-dimensional projection of the flux-limited SDSS data with $|\delta| \lesssim 15°$. The range of absolute magnitudes probed is $-22.0 \lesssim M_{\rm r} \lesssim -17.2$.

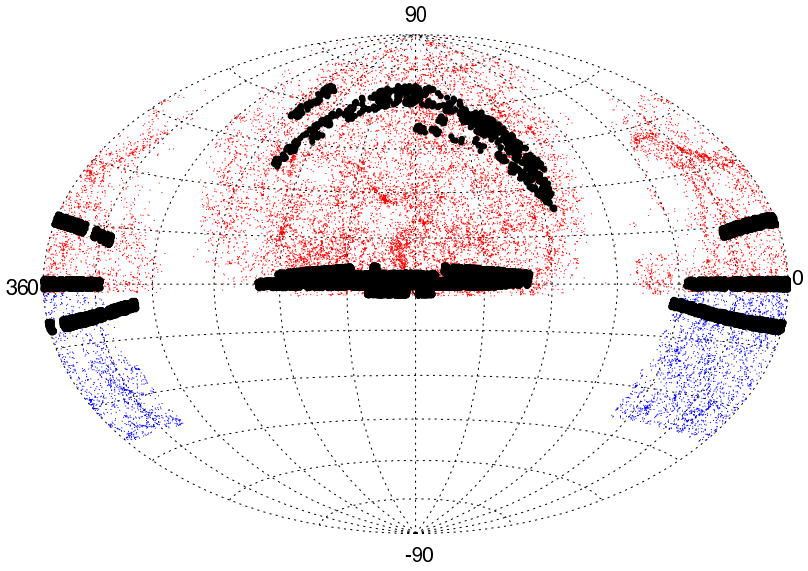

Figure 2.3: Aitoff projection in celestial coordinates of the current SDSS galaxy redshift survey data (black points) and the combined Updated Zwicky Catalog (red) and Southern Sky Redshift Survey (blue). Approximate coordinates of each region are given in the text in Section 2.1 .

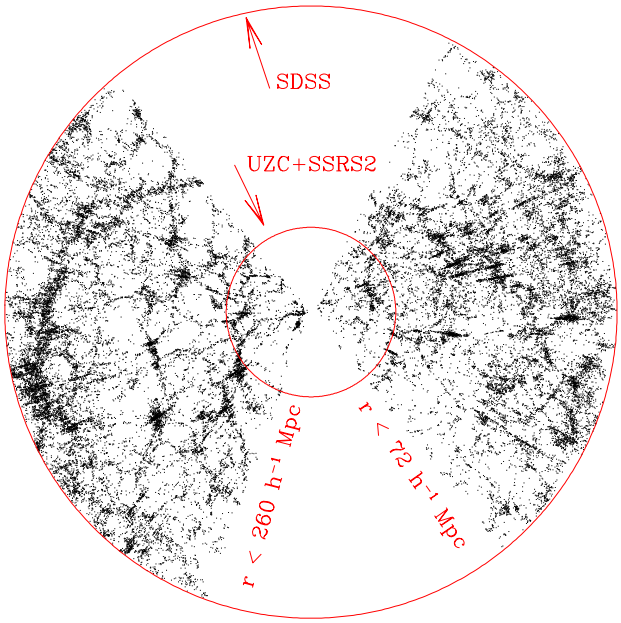

Figure 2.4: Cone diagram of the flux-limited SDSS data with $|\delta| \lesssim 15°$. The inner circle is drawn at $72h^{-1}$Mpc, which is the depth of the combined UZC and SSRS2 volume-limited sample. The outer circle is drawn at $260h^{-1}$Mpc, which is the depth of the SDSS volume-limited sample. In the region $100 < r < 260h^{-1}$Mpc we use the SDSS data to trace the distribution of the voids. However, nearby the SDSS currently is limited in volume as only narrow strips have been observed. Therefore, nearby we use the UZC+SSRS2 to trace the voids out to $72h^{-1}$Mpc. An interesting feature in this figure is the Sloan Great Wall of galaxies (left side near the outer circle). This is the largest observed structure in the universe.

Chapter 3: Finding Void Galaxies

Given the size of our data and the SDSS survey geometry we search for void galaxies in the SDSS using the nearest neighbor (nn) statistic. Because of the SDSS observing strategy to observe large ranges of RA and smaller ranges in declination, large voids of radius $\sim 10h^{-1}$Mpc at the present can only be detected in the equatorial stripe (see Section 2.1). Therefore, for the current status of the SDSS the nn statistic is the best tool for finding void galaxies because it allows us to search all regions, even small volumes where more sophisticated algorithms like `VOIDFINDER` (Hoyle & Vogeley 2002) and Delaunay tessellations (Icke & van de Weygaert 1987; Hoyle & Vogeley 2004) cannot be applied. This nn statistic consists of counting the number of neighboring galaxies around each galaxy in one sample (test sample, in our case the magnitude-limited sample) from another sample (density field tracer, the volume-limited sample). We then classify each magnitude-limited galaxy according to the number of volume-limited galaxy neighbors. The two volume-limited samples (SDSS and UZC+SSRS2) are used to trace the voids. Any magnitude-limited galaxy that lies away from the boundary of the volume-limited sample and has less than 3 volume-limited sample neighbors in a sphere of radius $7h^{-1}$Mpc is considered a void galaxy. Before identifying void galaxies we must first remove those galaxies that lie near the

boundary of the survey from the magnitude-limited samples. The nearest neighbor statistic is then applied to these 'edge corrected' samples to find the respective void galaxies. We expand on each of these steps below.

3.1 Proximity to Survey Boundary

Galaxies in the magnitude-limited SDSS samples that lie near the boundaries of the volume-limited samples have systematically larger distances to their third nearest neighbors than galaxies that lie deep in the volume-limited samples. This is because potentially closer neighbors have not been observed/included in the sample. These galaxies have a higher probability of being selected as void galaxies than the galaxies inside the survey. We correct for this bias in the following way: We generate a random catalog with the same angular and distance limits as the corresponding volume-limited sample (SDSS and UZC+SSRS2) but with no clustering. We count how many random points lie around each of the magnitude-limited SDSS galaxies. If the density around a galaxy is less than a certain value, we reject it from the SDSS samples. This is explained further below.

To remove galaxies near the boundary of the survey we:

- go to a galaxy from the magnitude-limited sample
- count how many random points (N) lie in a sphere of size, $r = 3.5h^{-1}$Mpc around this galaxy
- compute the respective number density, $\rho = N/V$, where, $V = (\frac{4\pi}{3}r^3)$

- we know the expected number density in the random sample ($\rho_{random} = N_{random}/\frac{\Omega}{3}r^3$)
- if $\rho < \rho_{\rm random}$, remove this galaxy from the magnitude-limited sample (its proximity to the sample's boundaries causes $\rho < \rho_{\rm random}$)
- repeat steps above until every magnitude-limited galaxy has been tested.

We apply this procedure twice, once when we compare the distant SDSS magnitude-limited sample with the SDSS random catalog and again when we compare the nearby SDSS magnitude-limited sample with the UZC+SSRS2 random catalog. The distant SDSS sample is reduced from 65,186 galaxies to 13,742 galaxies, the nearby SDSS sample is reduced from 3784 galaxies to 2,450 galaxies. The nearby SDSS sample is cut less drastically as the UZC+SSRS2 sample covers a greater area, thus fewer of the SDSS galaxies are near edges of the volume-limited catalog to which they are compared.

Because of the process of designing tiles for spectroscopy (tiling) and because the SDSS is not finished, the angular selection function is complicated (see Figure 2.3). An algorithm to quantify the fraction of galaxies that have been observed in any given region, i.e. the completeness, has been developed and is described in Tegmark, Hamilton, & Xu (2002). The completeness for any given (α, δ) coordinate is returned, allowing a random catalog with the same angular selection function to be created. For the SDSS, the completeness within the regions that have been observed is typically $> 90\%$. The angular selection function for the combined UZC+SSRS2 sample is easier as the surveys are finished and the completeness for the UZC is $\sim 96\%$.

3.2 Nearest Neighbor Statistic

We identify galaxies with a large distance to their nth nearest neighbor as void galaxies. We follow the work of El-Ad & Piran (1997) and Hoyle & Vogeley (2002) and use $n = 3$ rather than $n = 1$ in the nearest neighbor analysis. It is a fact that galaxies cluster, therefore, it is not unreasonable to expect that void galaxies might also be found in small groups. If we used $n = 1$ then a pair of galaxies in an otherwise low density environment would not be classified as void galaxies, hence we set $n = 3$. Note that we do not make any corrections for peculiar velocities along the line of sight. Therefore, we might underestimate the density of systems with large velocity dispersions which could pollute the void galaxy population. This could lead to a slight underestimate of the differences between the void and wall populations.

We find the third nearest neighbor distance for each galaxy in the SDSS magnitude-limited samples to galaxies from the corresponding volume-limited samples, then compute the average separation distance $\bar{d}_{sep}^{(3)}$ and the standard deviation, $\sigma_{sep}^{(3)}$ of this distance. We fix the search radius $d_{\rm crit}$ to be $7h^{-1}$Mpc which is approximately equal to $\bar{d}_{sep}^{(3)} + 1.5\sigma_{sep}^{(3)}$ found from the two samples, (the actual values are given in Sections 3.3 and 3.4). This also agrees with the criterion for defining wall and void galaxies in `VOIDFINDER` (Hoyle & Vogeley 2002), which is an algorithm designed to search for large $r > 10h^{-1}$Mpc regions of the universe that have $\delta\rho/\rho < -0.9$. i.e., find the location of true voids in a galaxy distribution. Galaxies that have their third nearest neighbor at a distance $\geq d_{\rm crit} = 7h^{-1}$Mpc are classified as void galaxies. The galaxies that we classify as void galaxies are then removed from the parent SDSS sample. This

yields two mutually exclusive catalogs which we will refer to from now on as void and wall galaxies. The average number of volume-limited galaxies in a sphere of $7h^{-1}$Mpc around a wall galaxy is 25 compared to 2 around a void galaxy, demonstrating that void galaxies really are in highly underdense regions. To test for possible bias in the redshift distribution of void and wall galaxies, we construct ten mock volume and flux-limited samples with geometry identical to the SDSS survey, using mock galaxies drawn from the Virgo Consortium's Hubble Volume z=0 ΛCDM simulation (Frenk et al. 2000). In Figure 3.2 we show the number of galaxy distribution as a function of comoving distance for the void (solid line) and wall (dotted line) mock samples. The error bars are the 1σ errors on the mock void galaxy samples. It can be clearly seen that since the two curves agree within the error bars, our procedure for identifying void galaxies and removing objects (both void and wall) near the survey boundaries does not produce any bias in the redshift distribution of void and wall galaxies.

In Figure 3.3 we show the redshift distribution for the void and wall(nearby and distant) data samples. The difference in the distribution of redshifts between the wall and void galaxy samples can be explained by the fact that for a flux-limited sample, the fraction of void galaxies at large distances must be smaller, because there are relatively fewer very bright void galaxies. It is important to point out that the comparison between wall and void galaxies does not rely on their redshift distributions being identical. Because the distributions of luminosities are different, the redshift distributions of these two flux-limited samples are not the same. Recall that we are not comparing their spatial distributions, we are comparing their intrinsic properties. When we compare the surface brightness profiles and colors, we select sub-samples

with the same range of luminosity, to control for the difference in luminosity functions. Here, this is done with rather broad bins of absolute magnitude, but tests with much narrower bins yield the same trends, albeit with much noisier results, as expected for the smaller number of galaxies/bin. The difference in redshift distributions could affect these results if the surface brightness and color properties of all galaxies strongly vary along the line of sight because of large-scale structure or evolution. The former adds noise to this measurement, not a bias. It is a sampling effect due to the finite volume of the survey. Regarding the latter, although Blanton et al. (2001) find that the SDSS luminosity function does show evolution of M*, it is very small over the range $100 - 260h^{-1}$Mpc.

To test that our procedure has identified genuine void galaxies, we compute the mean, median and upper bound of the density contrast ($\delta\rho/\rho$) around void galaxies and compare these values to the emptiness of voids as defined by `VOIDFINDER`. The number of galaxies in the SDSS volume-limited sample is 22,866 and the respective volume, $V = \frac{\Omega}{3}(r^3 - r_o^3) = \frac{0.6}{3}(260^3 - 100^3) = 3.32 \times 10^6 h^{-3}\mathrm{Mpc}^3$, therefore, the mean density is $\bar{\rho} = 6.84 \times 10^{-3} h^3 \mathrm{Mpc}^{-3}$. The void galaxies contain less than three neighbors in a sphere of $7h^{-1}$Mpc, thus, the density around the void galaxies is $\rho_v \leq 4/(\frac{4\pi}{3})7^3 = 2.78 \times 10^{-3} h^3 \mathrm{Mpc}^{-3}$. Therefore, the density contrast around void galaxies in the distant sample is $\delta\rho/\rho \equiv (\rho_v - \bar{\rho})/\bar{\rho} \leq -0.6$. This number is very similar for the nearby sample. It is an upper bound, as the median third nearest neighbor distance to the void galaxies is closer to $8h^{-1}$Mpc, giving values for the density contrast closer to $\delta\rho/\rho = -0.8$. This value is low, although not as low as that found by `VOIDFINDER` for the density contrast of the voids. Because density estimates

around void galaxies are centered on a galaxy and galaxies are clustered, we expect the density around void galaxies (ρ_{vg}) to be higher than the mean density of a void ($\bar{\rho}_{void}$). Recall that the mean density of a void is about $0.1\times$ mean density of the universe ($\bar{\rho}_{universe}$) and since fluctuations in galaxy density in spheres of radius $8h^{-1}$Mpc is ~ 1 ($\sigma_8 \sim 1$), then: $\rho_{vg}(r \leq 7h^{-1}\mathrm{Mpc}) = \bar{\rho}_{void} \times (1 + \bar{\xi}(r = 7h^{-1}\mathrm{Mpc})) \sim 2 \times \bar{\rho}_{void}$.

It is important to keep in mind that since most of the void galaxies will lie near the edges of voids, the typical density contrast around void galaxies is less extreme than the density contrast of the whole void region (see Figure 11 in Benson et al. 2003).

3.3 Distant Void Galaxies

For SDSS galaxies that lie in the distant SDSS sample, we use the SDSS volume-limited sample to define the galaxy density field. Using the third nearest neighbor ($n = 3$), we obtain $(\bar{d}^{(3)}_{sep}, \sigma^{(3)}_{sep}) = (3.6, 2.10)h^{-1}$Mpc, from which we obtain $d_{\mathrm{crit}} = 6.75h^{-1}$Mpc, which we round up to $7h^{-1}$Mpc. From the distant SDSS sample of 13,742 galaxies we find 1010 void galaxies. This sample of void galaxies will be referred to as VGD (as in Void Galaxy Distant). The sample of 12,732 non-void galaxies we label WGD (as in Wall Galaxy Distant). The fraction of void galaxies in the distant sample is $\sim 8\%$. This is only slightly higher than the fraction of void galaxies found by `VOIDFINDER` (Hoyle & Vogeley 2002) and by El-Ad & Piran (1997).

Figure 3.1 shows a redshift cone diagram of the SDSS wall galaxies (gray dots) and the corresponding void galaxies, VGD (red points). We plot only galaxies with

$|z| < 5h^{-1}$Mpc. Note that some of the void galaxies appear to be close to wall galaxies. This is merely a projection effect. All the void galaxies have less than three neighbors within a radius of $7h^{-1}$Mpc.

After obtaining the WGD and VGD samples, we split each void and corresponding wall galaxy sample into approximately equal halves by applying an absolute magnitude cut. In this case, the magnitude cut is done at $M_r = -19.5$, from which we obtained the corresponding sub-samples, [WGD_b, VGD_b] ($M_r \leq -19.5$, b=bright) and [WGD_f, VGD_f] ($M_r > -19.5$, f=faint). The approximate range of absolute magnitudes covered by the sub-samples are, $-22 \lesssim M_r \leq -19.5$, for the bright and $-19.5 < M_r \leq -17.77$, for the faint half. Figure 3.4 shows the distribution of absolute magnitudes for the distant samples. Note that the terms *bright* and *faint* in this context are used to describe the sub-samples relative to their parent sample.

3.4 Nearby Void Galaxies

To find faint void galaxies, which are present in the SDSS sample only at small comoving distances, we use the UZC+SSRS2 volume-limited sample to trace the voids because the slice-like SDSS samples are too thin to detect three-dimensional voids in this nearby volume.

The number of galaxies in the SDSS nearby sample, after applying the boundary corrections, is 2456. We measure the distance to the third nearest UZC+SSRS2 volume-limited galaxy and obtain the values $(\bar{d}^{(3)}_{sep}, \sigma^{(3)}_{sep}) = (3.9, 1.9)h^{-1}$Mpc, hence the choice of $d_{\rm crit} = 7h^{-1}$Mpc is still applicable. In this case we find 194 void galaxies.

We refer to this void galaxy sample as VGN (N for nearby) and the respective wall galaxy sample (after removing the respective void galaxies) as WGN.

We again apply an absolute magnitude cut to the VGN and WGN samples. For the nearby sample, this cut is done at $M_r = -17.0$ (see Figure 3.5). This cut divides the wall and respective void galaxy samples into approximately equal halves which we label [WGN_b, VGN_b] ($M_r \leq -17.0$, b=bright) and [WGN_f, VGN_f] ($M_r > -17.0$, f=faint). The range of absolute magnitudes included in each sub-sample is $-19.7 \lessapprox M_r \leq -17.0$ for the bright half and $-17.0 < M_r \lessapprox -13.0$ (see Figure 3.5), for the faint half. In this case the percent of void galaxies found is 8.6%.

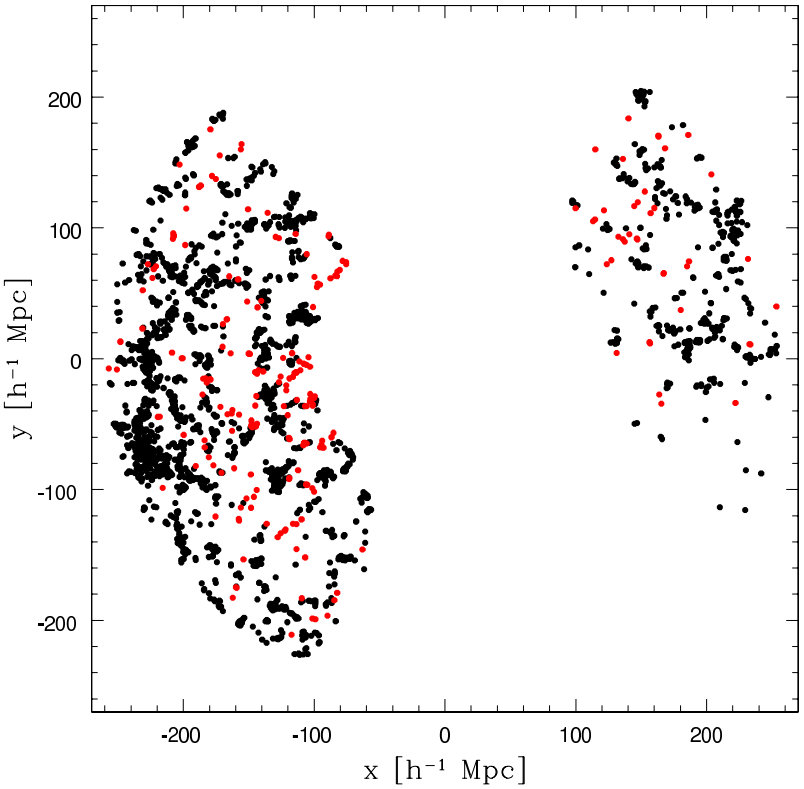

Figure 3.1: Redshift space distribution of void and wall galaxies. The black points show a cone diagram of the SDSS wall galaxies ($100 < r < 260h^{-1}$Mpc, $M_r \lesssim -17.5$). The red points show the void galaxies from the apparent magnitude-limited sample ($r < 17.5$). We only plot galaxies with $|z| < 5h^{-1}$Mpc. Note that some of the red points appear to be close to wall galaxies. This is, however, just a projection effect (we suppress the z direction) and all void galaxies have less than three neighbors within a 3-dimensional radius of $7h^{-1}$Mpc.

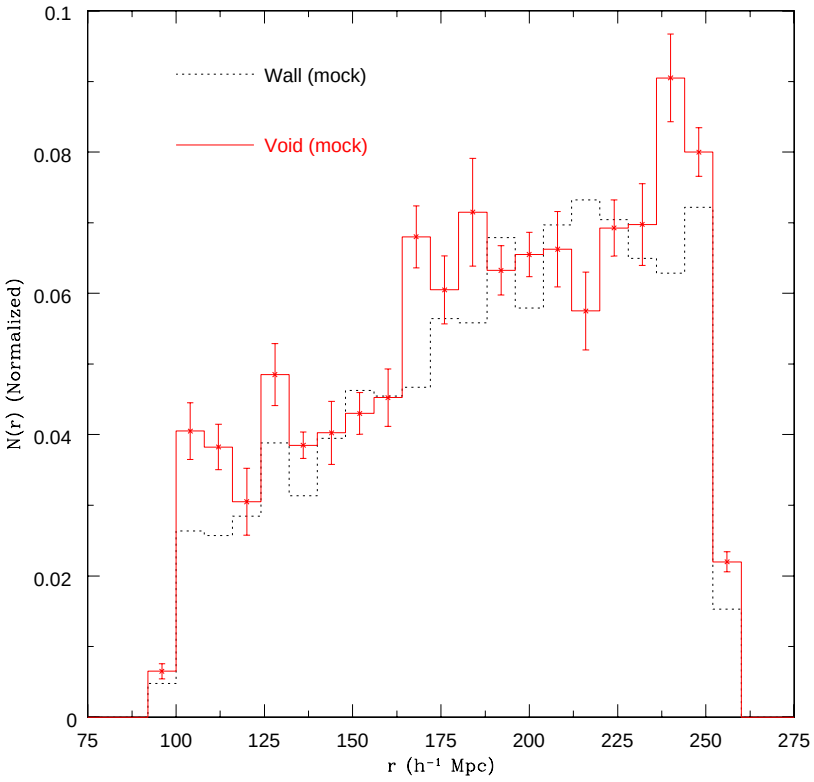

Figure 3.2: Number of galaxies as a function of comoving coordinate distance for the void (solid line) and wall (dotted line) mock samples averaged over the 10 realizations. The error bars are the 1σ errors on the mock void galaxy samples. The ten independent realizations are made in the SDSS equatorial stripe (discussed in Section 2.1) from the Virgo Consortium's Hubble Volume $z = 0$ ΛCDM simulation (Frenk et al. 2000).

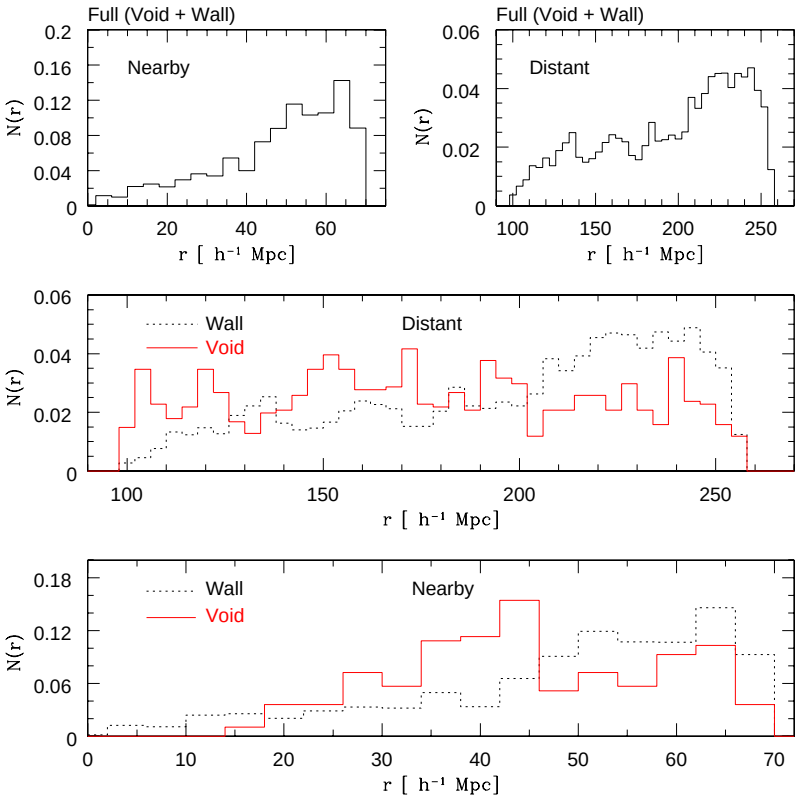

Figure 3.3: Number of galaxies as a function of comoving coordinate distance for the void (solid line) and wall (dotted line) samples respectively. The top row shows the full (void and wall) Nearby and Distant samples. The middle row shows the Distant void (solid) and wall (dotted) samples and the bottom row the case for the Nearby samples. The y-axis is the respective normalized fraction and the x-axis the comoving coordinate distance using an $(\Omega_\Lambda, \Omega_{\rm matter})$=(0.7,0.3) cosmology.

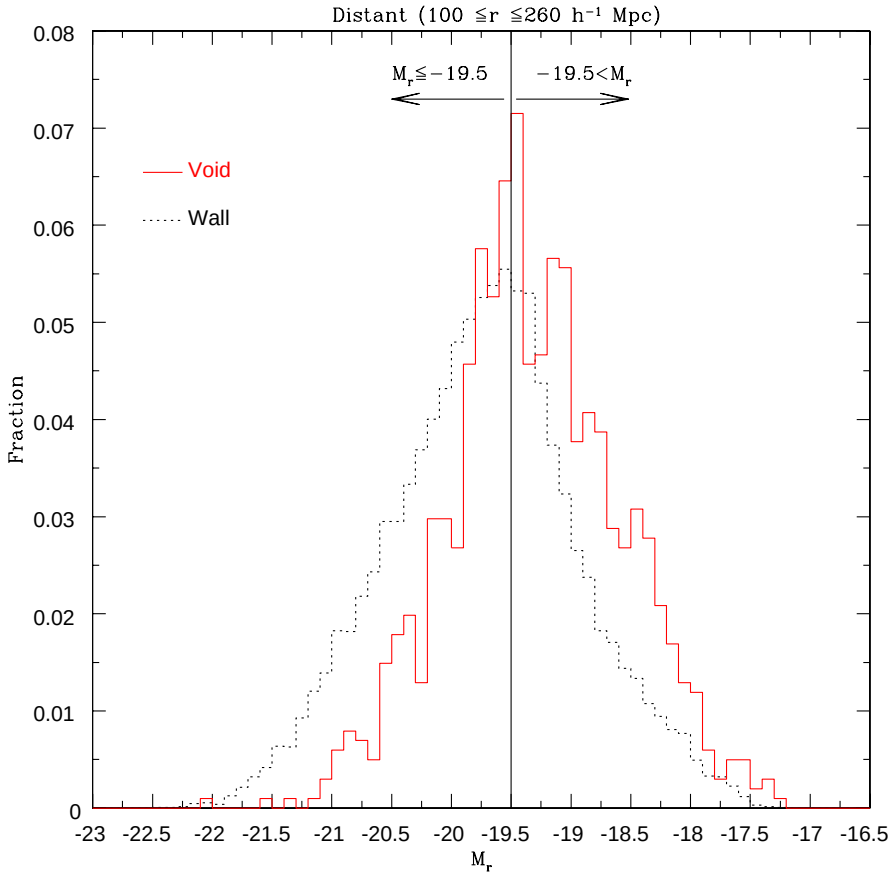

Figure 3.4: Distribution of the absolute magnitudes in the distant wall (WGD, dotted line) and void (VGD, solid line) galaxy samples. The parent sample is apparent magnitude-limited at $r \leq 17.5$ and redshift limited at $z \leq 0.089$. We split both data sets at $M_r = -19.5$ to obtain the void galaxy sub-samples [VGD_b (b=bright), VGD_f (f=faint)] and wall galaxy sub-samples [WGD_b, WGD_f]. The cut at $M_r = -19.5$ divides both the void and wall galaxy samples into approximately equal halves. This histogram bins galaxies by $\Delta M = 0.1$. The range of absolute magnitudes probed by the void galaxies that lie within this volume is $-22.0 \lesssim M_r \lesssim -17.2$.

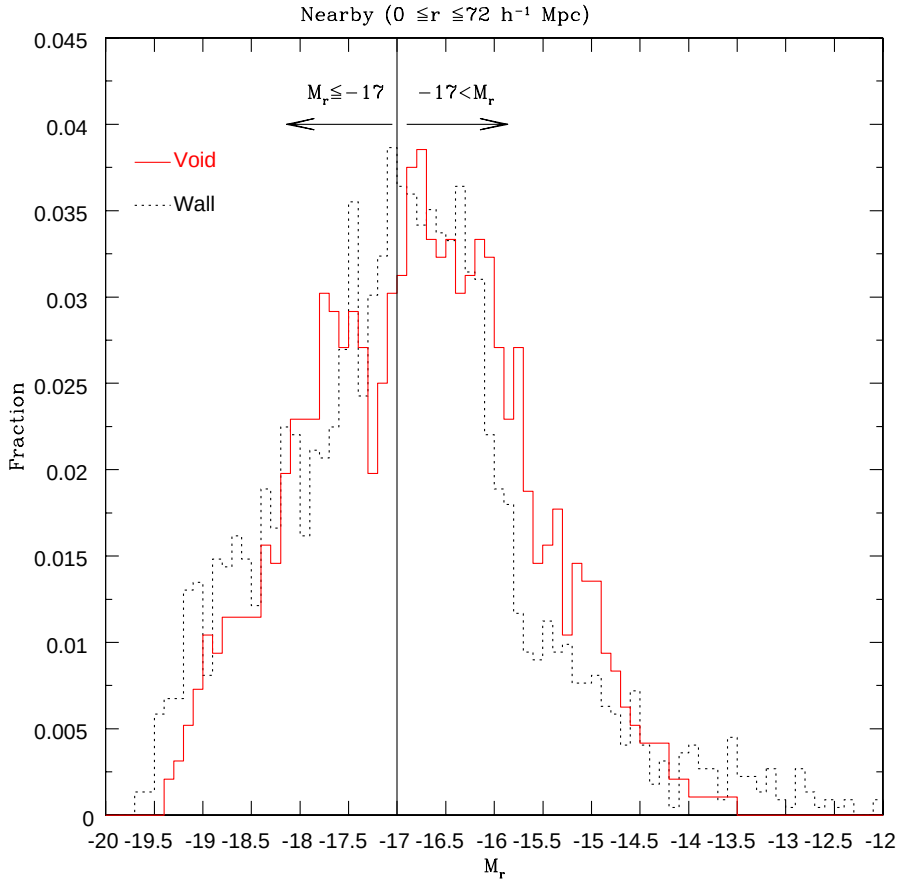

Figure 3.5: Distributions of absolute magnitudes in the nearby wall (WGN, dotted line) and void (VGN, solid line) galaxy samples. The parent sample is apparent magnitude-limited at $r \leq 17.5$ and redshift limited at $z \leq 0.025$. Both data sets are split at $M_r = -17$ to obtain the void galaxy sub-samples [VGN_b (b=bright), VGN_f (f=faint)] and wall galaxy sub-samples [WGN_b, WGN_f]. The cut at $M_r = -17$ divides both the void and wall samples into approximately equal halves. This histogram bins galaxies by $\Delta M = 0.1$. The range of absolute magnitudes probed by the void galaxies that lie within this volume is $-19.7 \lesssim M_r \lesssim -13.0$.

Chapter 4: Catalog of Void Galaxies

We present a catalog of more than 10^3 void galaxies from the Sloan Digital Sky Survey. We use a nearest neighbor analysis to construct the sample of void galaxies. The density field of galaxies is traced using a volume-limited sample with $z_{max} = 0.089$. Galaxies from the flux-limited SDSS with $z \leq z_{max}$ and fewer than three volume-limited neighbors within $7h^{-1}$Mpc are classified as void galaxies. Details of how the sample of void galaxies is obtained are discussed in Chapter 3. These galaxies have density contrast $\delta\rho/\rho < -0.6$ and span a range of absolute magnitude from $M_r = -13.5$ to $M_r = -22.5$ with redshift $z < 0.089$. Measured photometric parameters from the SDSS photometric pipeline include the absolute magnitude in u, g, r, i, z, concentration index, and Sersic index. In addition, spectroscopic parameters from the SDSS `spectro1d` pipeline such as the equivalent width, sigma, and height of the fitted Gaussian to the respective line are also included for 5 emission lines. Derived star formation and specific star formation rates from Hα are also included. We provide the 4000 Å Balmer strength and stellar masses from Kauffmann et al. (2003; K03a). For other galaxies in our sample not included in K03a we estimate the stellar masses from a least squares fit using the z-band flux. Color composite images and calibrated spectra of all objects are also available. Rojas et al. (2003, 2004) studied

the photometric and spectroscopic properties of these galaxies and discovered that they are bluer, more late-type, have larger emission line equivalent widths, larger specific star formation rates, smaller stellar masses and smaller 4000 Å Balmer break than non-void galaxies of similar luminosities and surface brightness profiles. Hoyle et al. (2003) computed the corresponding luminosity function and found that voids are not filled with a large population of dwarf galaxies. The metallicities of these void galaxies were studied by Hao et al. (2004) and it was found that they have comparable metallicities to galaxies in more typical environments.

4.1 The Void Galaxy Catalog

Here we provide the list of parameters that are included in the two (nearby and distant) catalogs of void galaxies. A brief description of each parameter is included next to each entry in Table 1. and a more detailed discussion is given in the following sections. Both catalogs (nearby and distant) have the same number of columns and parameters as those listed in Table 1. There are 1010 void galaxies in the distant sample and 194 and the nearby sample.

4.1.1 The SDSS Coordinate System

RA and DEC

Details of the SDSS coordinate system are given in Stoughton et al. (2002), however, we provide a brief review below. The SDSS coordinate system (λ, η) consists of a spherical coordinate system with poles at $\alpha = 95°$, $\delta = 0°$ and $\alpha = 275°$, $\delta = 0°$

(J2000). Where α and δ are the RA and DEC in J2000 Equatorial coordinates respectively.

The survey equator is a great circle perpendicular to the J2000 celestial equator, intersecting it at $\alpha = 185^\circ$ and $\alpha = 5^\circ$. Lines of constant η are great circles perpendicular to the survey equator, and lines of constant λ are small circles parallel to the survey equator; $\lambda = 0^\circ$, $\eta = 0^\circ$ is located at $\alpha = 185^\circ$, $\delta = 32.5^\circ$, with η increasing northward.

The survey area is divided into stripes, where each stripe is centered along a line of constant η, separated from the adjoining stripe or stripes by 2.5°. Each drift scan tracks a survey stripe, offset by $\pm 386''$ perpendicular to the stripe. Two scans (or "strips"), one offset to the north and one to the south, are required to fill a stripe. The survey latitude tracked by stripe n is given by

$$\eta = (\eta - 10) \times 2.5^\circ - 32^\circ.5 \tag{4.1}$$

in the northern Galactic hemisphere, and by

$$\eta = (\eta - 82) \times 2.5^\circ - 32.5^\circ \tag{4.2}$$

for the three stripes in the southern Galactic hemisphere. These stripes are superposed on a Galactic extinction map in Figure 2 of York et al. (2000).

The natural coordinate system to use for processing a given drift scan is the *great-circle coordinate system* for that stripe, (μ, ν), in which the equator of the coordinate

system is the great circle tracked by the scan. This great circle is inclined by $i = \eta + 32.5^\circ$ to the J2000 celestial equator, with an ascending node of 95°; $\mu = \alpha$ at the ascending node, and μ increases in the scan direction (east) and ν increases to the north. Each stripe has its own great-circle coordinate system.

The transformation equations between the different coordinate systems are

$$\cos(\alpha - 95^\circ)\cos\delta = -\sin\lambda \tag{4.3}$$

$$= \cos(\mu - 95^\circ)\cos\nu, \tag{4.4}$$

$$\sin(\alpha - 95^\circ)\cos\delta = \cos\lambda\cos(\eta + 32^\circ.5) \tag{4.5}$$

$$= \sin(\mu - 95^\circ)\cos\nu\cos i - \sin\nu\sin i, \tag{4.6}$$

$$\sin\delta = \cos\lambda\sin(\eta + +32^\circ.5) \tag{4.7}$$

$$= \sin\nu\cos i + \sin(\mu - 95^\circ)\cos\nu\sin i \tag{4.8}$$

Positions of the galaxies are given in right ascension (RA) and declination (DEC) and distances (in comoving coordinates) to the third nearest neighbor are computed using an $(\Omega_m, \Omega_\Lambda) = (0.3, 0.7)$ cosmology with $H_o \equiv 100h\,\mathrm{km\ s^{-1}\,Mpc^{-1}}$.

4.1.2 SDSS Identification Parameters

Photometric ID Parameters

The run number is a term used to describe one continuous scan of the SDSS imaging camera on the sky, and a stripe is the great circle covered by two runs, 2.5°

wide. Each stripe is covered in two strips, separated in the north-south direction so that the interleaved scans of the six columns of the imaging camera completely cover the stripe. Runs are combined into chunks, contiguous areas of the sky in which spectroscopic targets will be selected and spectroscopic tiling (the process by which targets are assigned to spectroscopic plates) will be done. A segment is a single piece of a run for a single camera column. The frames pipeline (`frames`) detects, deblends, and measures objects, carrying out this processing on a field-by-field basis. Each object detected during the frames analysis of a particular set of data is given a unique identifier, which consists of five integers:

- `run`: A run number refers to a given uninterrupted drift scan.
- `rerun`: Each time we analyze a run with a different set of pipeline versions or calibrations, we assign it a new rerun number. The same rerun number in different runs does not necessarily refer to the same version of the pipelines.
- `camcol`: This number, from 1 to 6, refers to the dewar, or column of photometric CCDs in the imaging camera, with which this object was imaged.
- `fieldID`: This refers to which field the object is in.
- `objID`: This is an identification number for the object that is unique within each field.

Spectroscopic ID Parameters

Plate is the plate number (four digits, zero-padded), MJD is the Modified Julian Day on which observations were completed, and fiber is the fiber of plug plate fiber

number (three digits, zero-padded).

4.1.3 Photometric Parameters

Magnitudes

The five SDSS color bands have been chosen to cover from the UV atmospheric cutoff near 3000 Å up to the sensitivity limit for silicon CCDs near 11000 Å. The 5 photometric bands are: u, g, r, i, and z, have design effective wavelengths of 3550, 4770, 6230, 7620, and 9130 Å, respectively (Fukugita et al. 1996; Gunn et al. 1998).

The SDSS has adopted a modified form of the Petrosian (1976) system, measuring galaxy fluxes within a circular aperture whose radius is defined by the shape of the azimuthally averaged light profile.

The "Petrosian ratio" R_P at a radius r from the center of an object is defined as the ratio of the local surface brightness in an annulus at r to the mean surface brightness within r, as described by Blanton et al. 2001a, Yasuda et al. 2001, Strauss et al. 2001:

$$R_P \equiv \frac{\int_{0.8r}^{1.25r} dr' 2\pi r' I(r') / [\pi(1.25^2 - 0.8^2) r^2]}{\int_0^r dr' 2\pi r' I(r') / (\pi r^2)} \tag{4.9}$$

where $I(r)$ is the azimuthally averaged surface brightness profile.

The Petrosian radius r_P is defined as the radius at which $R_P(r_P)$ equals some specified value $R_{P,lim}$ set to 0.2 in this case. The Petrosian flux in any band is then defined as the flux within a certain number N_P (equal to 2.0 in this case) of r Petrosian radii:

$$F_P = \int_0^{N_P r_P} 2\pi r' I(r') dr' \tag{4.10}$$

In the SDSS five-band photometry, the aperture in all bands is set by the profile of the galaxy in the r band alone. This procedure ensures that the color measured by comparing the Petrosian flux F_P in different bands is measured through a consistent aperture.

Concentration Index

Morphological properties of void and wall galaxies can be inferred from concentration indices measured by the SDSS photometric pipeline (Lupton et al. 2001; Stoughton et al. 2002; Pier et al. 2002; Lupton et al. 2002). The concentration index (CI) is defined by the ratio CI $\equiv$ r90/r50, where $r90$ and $r50$ correspond to the radii at which the integrated fluxes are equal to 90% and 50% of the Petrosian flux, respectively. A large value of CI corresponds to a relatively diffuse galaxy and a small value of CI to a highly concentrated galaxy. The concentration index has been shown to correlate well with galaxy type (Strateva et al. 2001; Shimasaku et al. 2001). Spiral galaxies are usually found to have small concentration indices ($\lesssim 2.5$) whereas ellipticals have larger concentration indices ($\gtrsim 2.5$).

Sersic Index

Another measure of galaxy morphology is the Sersic index (Sersic 1968), found by fitting the functional form

$$I(r) = A \exp[-(r/r_o)^{1/n}], \tag{4.11}$$

where n is the Sersic index itself, to each galaxy surface brightness profile (SBP). With this form, $n = 1$ corresponds to a purely exponential profile, while $n = 4$ is a de Vaucouleurs profile. We use the Sersic indices as measured by Blanton et al. (2002) for the SDSS galaxies.

In brief, Blanton et al. (2002) find the parameters A, r_o, and n in Eq. [13] that minimize χ^2 with respect to the observed i-band radial profile and errors (as expressed by the `profMean` and `profErr` parameters in the SDSS catalog). Sersic profiles have been fitted to the profiles of the other bands as well; the results of the g, r, i, and z profiles are all fairly consistent with one another, while the u-band profile fits tend to be much less concentrated than the others.

4.1.4 Spectroscopic Parameters

Details of the spectroscopic system are discussed in York et al. (2000). Below we describe the overall features of the spectroscopic system and include a brief discussion on the spectroscopic parameters measured. The SDSS spectroscopic pipeline uses two spectrographs, each producing 320 spectra. There are thus four CCD detectors, each of the same kind as are present in the g, r, and i bands in the camera, 2048 pixels square with 24 μm pixels. 640 individual spectra observed over a 3°-diameter field at a resolution $R \equiv \lambda/\delta\lambda$ of about 1800 in the wavelength range of 3800-9200 Å. This wavelength range is divided between two cameras by a dichroic at $\sim$ 6150 Å.

For each plate the exposure time is 45 minutes, split into at least three parts for cosmic-ray rejection. 15 minute exposures are repeated until the cumulative median

$(S/N)^2 > 15$ at $g = 20.2$ and $i = 19.9$ in all four cameras. The set of science exposures is preceded and followed by a series of shorter exposures for calibration: arcs, flat fields, and a 4 minute *smear* exposure on the sky for spectrophotometric calibration, in which the telescope is moved so that the $3''$; fiber on each object effectively covers a $5'' \times 8''$ aperture, aligned with the parallactic angle. The smear exposures allows recovery of object light excluded from the $3''$ fibers because of seeing and atmospheric refraction; they provide an accurate (albeit low signal-to-noise ratio) measure of the true spectral shape of the objects and are used for spectrophotometric calibration. The calibration and science exposures are immediately processed through a streamlined version of the second spectroscopic pipeline to inform the observers whether the calibrations were successful and to provide signal-to-noise ratio (S/N) diagnostics on the science exposures.

Emission Line Parameters

The `spectro1d`pipeline analyzes the combined, merged spectra output by spectro2d and determines object classifications (galaxy, quasar, star, or unknown) and redshifts; it also provides various line measurements and warning flags. The code attempts to measure an emission and absorption redshift independently for every targeted (nonsky) object. That is, to avoid biases, the absorption and emission codes operate independently, and they both operate independently of any target selection information.

Emission lines (peaks in the one-dimensional spectrum) are found by carrying out a wavelet transform of the continuum-subtracted spectrum $f_c(\lambda)$:

$$w(a,b) = \frac{1}{\sqrt{b}} \int_{-\infty}^{+\infty} f_c(\lambda) \bar{g} \left(\frac{\lambda - a}{b} \right) d\lambda, \tag{4.12}$$

where $g(x; a, b)$ is the wavelet (with complex conjugate $\bar{g}$) with translation and scale parameters a and b. The à trous wavelet (Starck, Siebenmorgen, & Gredel 1997) is applied. For fixed wavelet scale b, the wavelet transform is computed at each pixel center a; the scale b is then increased in geometric steps and the process repeated. Once the full wavelet transform is computed, the code finds peaks above a threshold and eliminates multiple detections (at different b) of a given line by searching nearby pixels. The output of this routine is a set of positions of candidate emission lines.

Each significant peak found by the wavelet routine is assigned a trial line identification from the common list (e.g., MgII) and an associated trial redshift. The peak is fitted with a Gaussian, and the line center, width, and height above the continuum are stored in the SpecLine class as parameters wave, sigma, and height, respectively. If the code detects close neighboring lines, it fits them with multiple Gaussians. Depending on the trial line identification, the line width it tries to fit is physically constrained. The code then searches for the other expected common emission lines at the appropriate wavelengths for that trial redshift and computes a confidence level (CL) by summing over the weights of the found lines and dividing by the summed weights of the expected lines. The CL is penalized if the different line centers do not quite match. Once all of the trial line identifications and redshifts have been explored, an emission-line redshift is chosen as the one with the highest CL and stored as z in the EmissionRedshift class. The exact expression for the emission-

line CL has been tweaked to match our empirical success rate in assigning correct emission-line redshifts, based on manual inspection of a large number of spectra from the EDR.

In the catalog we include the amplitude and width of the Gaussian fit and equivalent width for Hα, [OII] λ3727, Hβ, [NII] λ6583, and [OIII] λ5007 emission lines. We provide only these 5 emission lines because they are the strongest and also the ones used in our analysis.

Star Formation Rates

Star formation rates are estimated using Kennicutt's (1998b) prescription for the Hα flux valid in the Case B recombination (Osterbrock 1986) with a Salpeter (1955) initial mass function from

$$\mathrm{SFR} = 7.9 \times 10^{-42} L\,[M_{\odot}\ yr^{-1}], \tag{4.13}$$

where L is the derived Hα luminosity in units of [erg s^{-1}].

Detailed discussions of the Hα derived SFRs and systematics can be found in Chapter 6 Sections 5 & 6.

Stellar Masses

The integrated stellar masses for our samples are obtained from two sources: the primary source is from K03a's library of stellar masses and the secondary source uses a least squares fit to the stellar mass vs. z-band absolute magnitude relation. The z-band absolute magnitude is our preferred galaxy luminosity measure because it is less affected by extinction and less dependent on stellar age than the other four SDSS

bands (u, g, r, i; Fukugita et al. 1996). The reason for obtaining the masses from two different sources is because K03a's library of stellar masses only includes a subset of DR1 (Abazajian 2003) and our samples are from a larger database (Blanton et al. 2002; `sample10`). Therefore, for galaxies in our samples that are missing in K03a's list we need an alternate method to estimate the masses. Given that there is a nearly linear relationship between the z-band absolute magnitude and the logarithm of the estimated stellar mass, a least squares fit ($\mathrm{Log}_{10}(\mathrm{mass}/\mathrm{M}_{\odot}) = -0.5134\mathrm{M}_{\mathrm{z}} - 0.01581$) is a reasonable approach. Using this fit we can measure typical stellar masses to within a factor of 10.

Specific Star Formation Rates

We estimate the star formation rates per unit stellar mass using the stellar masses from K03a and the absorption, aperture, and dust corrected SFRs as discussed in Chapter 6.

Dn4000

We obtain the strength of the 4000Å Balmer break for the void galaxies from K03a. K03a's measurements of this index include about 70% of our galaxies. The $\mathrm{D}_n(4000)$ is an excellent spectral indicator of past star formation on timescales of $t \sim 1$Gyr and is also highly insensitive to dust attenuation effects. For hot stars where elements are multiply ionized the opacity decreases, therefore, hot, young stars (e.g., O and B) have lower amplitudes of $\mathrm{D}_n(4000)$ than cooler, older stars (e.g., K and M; see Figure 3, Bruzual 1983). Since late-type galaxies are mainly composed of young stars, their 4000 Å break is smaller than for early-type galaxies which are primarily composed of older stellar populations.

4.2 Images and Spectra

In Figure 4.1 we show a small sample of void galaxy images and spectra to show the quality of the observations and a few prominent spectral features. The images are color composites of void galaxies of different morphologies and colors. The top panel shows a typical void galaxy, the middle panel a void galaxy with an AGN, and the bottom panel a spiral void galaxy all taken from the distant sample. The complete set of images and spectra is available at

http://www.physics.drexel.edu/SDSS/void_galaxies.

4.3 Unusual Void Galaxies

In our sample of void galaxies we find that several of them have unusually high [OIII]/Hβ and [NII]/Hα flux ratios and hence high nuclear activity. This prompts the question of whether these galaxies have an Active Galactic Nucleus (AGN)? In our distant sample of void galaxies we find that about $9-30\%$ (depending on the classification method) possess an AGN. To identify AGNs in our samples of void galaxies we use the standard flux ratios log([OIII]/Hβ) and log([NII]/Hα) as suggested by Baldwin, Philips, & Terlevich (1981, BPT) and Villieux & Osterbrock (1987). The galaxy's position on this plot of log([OIII]/Hβ) versus log([NII]/Hα) indicates whether it is an AGN or star-forming galaxy.

From our sample of void galaxies we select only those galaxies for which all four lines have been measured in order to compute the respective ratios. Following the approach of K03a we then plot our void galaxies on the BPT diagram and look for

galaxies that have $\log([\mathrm{NII}]/\mathrm{H}\alpha) > -0.2$ and $\log([\mathrm{OIII}]/\mathrm{H}\beta) > 0.5$ simultaneously. This yields 20 void galaxies (out of 760) that have AGNs with high confidence (i.e. Seyferts). As suggested by Miller et al. (2003) an AGN can also be detected by only looking for a high $\log([\mathrm{OIII}]/\mathrm{H}\beta)$ or $\log([\mathrm{NII}]/\mathrm{H}\alpha)$ ratio. Therefore, if we simply look for a high $\log([\mathrm{NII}]/\mathrm{H}\alpha)$ (> -0.2) ratio, our sample of AGNs increases from 20 to 65 i.e., about 9% of our void galaxies have an AGN compared to 15% in the wall galaxies (1055/7151). In Figure 3 we plot the BPT diagram for the distant sample of void galaxies. Filled circles in the top right corner are the 'high confidence' AGNs (Seyferts) ($\log([\mathrm{NII}]/\mathrm{H}\alpha) > -0.2$ and $\log([\mathrm{OIII}]/\mathrm{H}\beta) > 0.5$) and galaxies that have $\log([\mathrm{NII}]/\mathrm{H}\alpha) > -0.2$ (top right and bottom right corners) are the additional AGNs (these include the Seyferts and Liners). The solid curve is the modified Kewley et al. (2001) demarcation curve from K03a:

$$\log([\mathrm{OIII}]/\mathrm{H}\beta) > \frac{0.61}{\log([\mathrm{NII}]/\mathrm{H}\alpha) - 0.05} + 1.3 \tag{4.14}$$

Any galaxy that lies above this curve is classified as an AGN and any galaxy that lies below it is a star-forming galaxy. With this criterion, we find that 234 void galaxies are classified as having an AGN (i.e. 31%) in contrast to 35% in the wall galaxy sample (2494/7151). In the nearby samples we find a lower fraction of AGNs, at most 10% from the nearby void galaxies and 17% from the nearby wall galaxies. Further examination of their equivalent widths confirms that we have identified AGNs based on their broad emission lines as can be seen in Figure 5. In this paper we do not discuss the individual properties of AGNs in voids and leave this as a topic for

future research.

4.4 Conclusions

Thanks to the superb quality and unprecedented quantity of data from the SDSS, we are able to compile a catalog of void galaxies that is large enough for robust statistical analysis. The catalog of nearby and distant void galaxies can be retrieved electronically from http://www.physics.drexel.edu/SDSS/void_galaxies. In addition, the spectra and images of our samples are available. Additional parameters (e.g., equivalent widths for emission lines not included in the catalog) can be obtained from the SDSS DR2 (Abazajian et al. 2004) database using the SDSS ID parameters provided in this catalog such as the `PLATE`, `FIBER`, and `MJD` for spectroscopic data and `RUN`, `RERUN`, `CAMCOL`, `FIELD`, and, `OBJID` for photometric data.

SDSS VOID GALAXY CATALOG

Table 4.1: Void Galaxy Catalog Format

Column	Parameter	Format	Description
1.	RA	F10.5	J2000 Right Ascension [degrees]
2.	DEC	F10.5	2000 Declination [degrees]
3.	z	F10.5	Redshift
4.	RUN	I3	Run number of this object
5.	RERUN	I2	Rerun number of this object
6.	CAMCOL	I3	Camera column number of this object
7.	FIELD	I3	Field number of this object
8.	OBJID	I3	Object number of this object
9.	PLATE	I3	Plate for this object
10.	FIBERID	I3	Fiber ID
11.	MJD	I5	Last 5 digits of the modified Julian date
12.	M_u	F12.5	SDSS u-band absolute magnitude
13.	M_g	F12.5	SDSS g-band absolute magnitude
14.	M_r	F12.5	SDSS r-band absolute magnitude
15.	M_i	F12.5	SDSS i-band absolute magnitude
16.	M_z	F12.5	SDSS z-band absolute magnitude
17.	CI	F7.5	Concentration index
18.	n	F7.5	Sersic Index
19.	Ha_SIGMA	F11.5	Sigma of the fitted Gaussian [Å]
20.	Ha_SIGMA_ERR	F11.5	Error in the width of the fitted Gaussian [Å]
21.	Ha_HEIGHT	F11.5	Height of the fitted Gaussian [10^{-17}ergs s^{-1} cm^{-2} Å^{-1}]
22.	Ha_HEIGHT_ERR	F11.5	Error on the height of the fitted Gaussian [10^{-17}ergs s^{-1} cm^{-2} Å^{-1}]
23.	Ha_EW	F11.5	Equivalent width [Å]
24.	Ha_EW_ERR	F11.5	Error on the equivalent width [Å]
25.	Ha_CONT	F11.5	Continuum value at this pixel [10^{-17}ergs s^{-1} cm^{-2} Å^{-1}]
26.	Hb_SIGMA	F11.5	Sigma of the fitted Gaussian [Å]
27.	Hb_SIGMA_ERR	F11.5	Error in the width of the fitted Gaussian [Å]
28.	Hb_HEIGHT	F11.5	Height of the fitted Gaussian [10^{-17}ergs s^{-1} cm^{-2} Å^{-1}]
29.	Hb_HEIGHT_ERR	F11.5	Error on the height of the fitted Gaussian [10^{-17}ergs s^{-1} cm^{-2} Å^{-1}]
30.	Hb_EW	F11.5	Equivalent width [Å]
31.	Hb_EW_ERR	F11.5	Error on the equivalent width [Å]
32.	Hb_CONT	F11.5	Continuum value at this pixel [10^{-17}ergs s^{-1} cm^{-2} Å^{-1}]
33.	OII_SIGMA	F11.5	Sigma of the fitted Gaussian [Å]
34.	OII_SIGMA_ERR	F11.5	Error in the width of the fitted Gaussian [Å]
35.	OII_HEIGHT	F11.5	Height of the fitted Gaussian [10^{-17}ergs s^{-1} cm^{-2} Å^{-1}]
36.	OII_HEIGHT_ERR	F11.5	Error on the height of the fitted Gaussian [10^{-17}ergs s^{-1} cm^{-2} Å^{-1}]
37.	OII_EW	F11.5	Equivalent width [Å]
38.	OII_EW_ERR	F11.5	Error on the equivalent width [Å]
39.	OII_CONT	F11.5	Continuum value at this pixel [10^{-17}ergs s^{-1} cm^{-2} Å^{-1}]
40.	NII_SIGMA	F11.5	Sigma of the fitted Gaussian [Å]
41.	NII_SIGMA_ERR	F11.5	Error in the width of the fitted Gaussian [Å]
42.	NII_HEIGHT	F11.5	Height of the fitted Gaussian [10^{-17}ergs s^{-1} cm^{-2} Å^{-1}]
43.	NII_HEIGHT_ERR	F11.5	Error on the height of the fitted Gaussian [10^{-17}ergs s^{-1} cm^{-2} Å^{-1}]
44.	NII_EW	F11.5	Equivalent width [Å]
45.	NII_EW_ERR	F11.5	Error on the equivalent width [Å]
46.	NII_CONT	F11.5	Continuum value at this pixel [10^{-17}ergs s^{-1} cm^{-2} Å^{-1}]
47.	OIII_SIGMA	F11.5	Sigma of the fitted Gaussian [Å]
48.	OIII_SIGMA_ERR	F11.5	Error in the width of the fitted Gaussian [Å]
49.	OIII_HEIGHT	F11.5	Height of the fitted Gaussian [10^{-17}ergs s^{-1} cm^{-2} Å^{-1}]
50.	OIII_HEIGHT_ERR	F11.5	Error on the height of the fitted Gaussian [10^{-17}ergs s^{-1} cm^{-2} Å^{-1}]
51.	OIII_EW	F11.5	Equivalent width [Å]
52.	OIII_EW_ERR	F11.5	Error on the equivalent width [Å]
53.	G_SYNTH	F12.5	Synthetic magnitude in G
54.	R_SYNTH	F12.5	Synthetic magnitude in R
55.	MASS	F10.5	Stellar mass [$\log_{10} M/M_\odot$] from K03a and and a least square fit
56.	SFR(Ha)	F10.5	Hα derived star formation rate [$M_\odot$ yr^{-1}]
57.	S-SFR(Ha)	E11.5	Hα derived star formation rate per unit stellar mass [yr^{-1}]
58.	D4000	F8.4	Strength of the 4000 Å Balmer break from K03a
59. - 63.	Di_nn	F8.5	Distance to the i^{th} nearest neighbor [h^{-1}Mpc] for $i = 1 - 5$ using an $(\Omega_m, \Omega_\Lambda) = (0.3, 0.7)$ cosmology

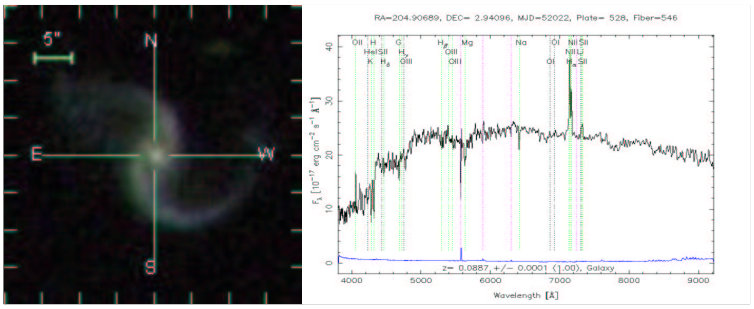

SDSS J133937.6+025627.4

Mr = −21.02, z = 0.089

Typical Void Galaxy

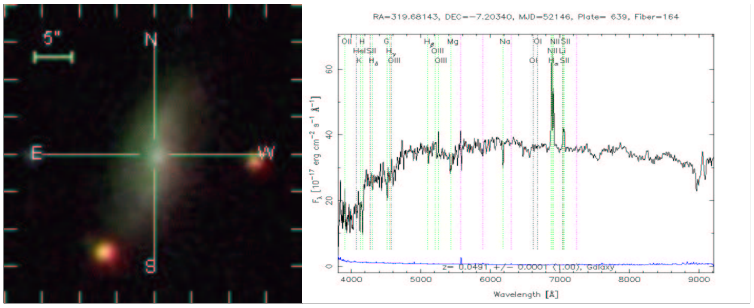

SDSS J211843.5−071212.2

Mr = −20.20, z = 0.049

Void Galaxy with an AGN

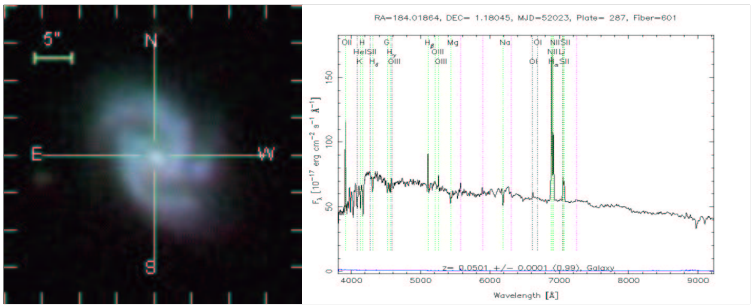

SDSS J121604.4+011049.5

Mr = −20.88, z = 0.05

Spiral Void Galaxy

Figure 4.1: In this figure we show the color image and respective spectra of 3 void galaxies. The top panel corresponds to a typical void galaxy, the middle panel shows a void galaxy with an AGN, and the bottom panel a spiral void galaxy. The respective SDSS ID, $r-$band absolute magnitude, and redshift are listed next to each spectra.

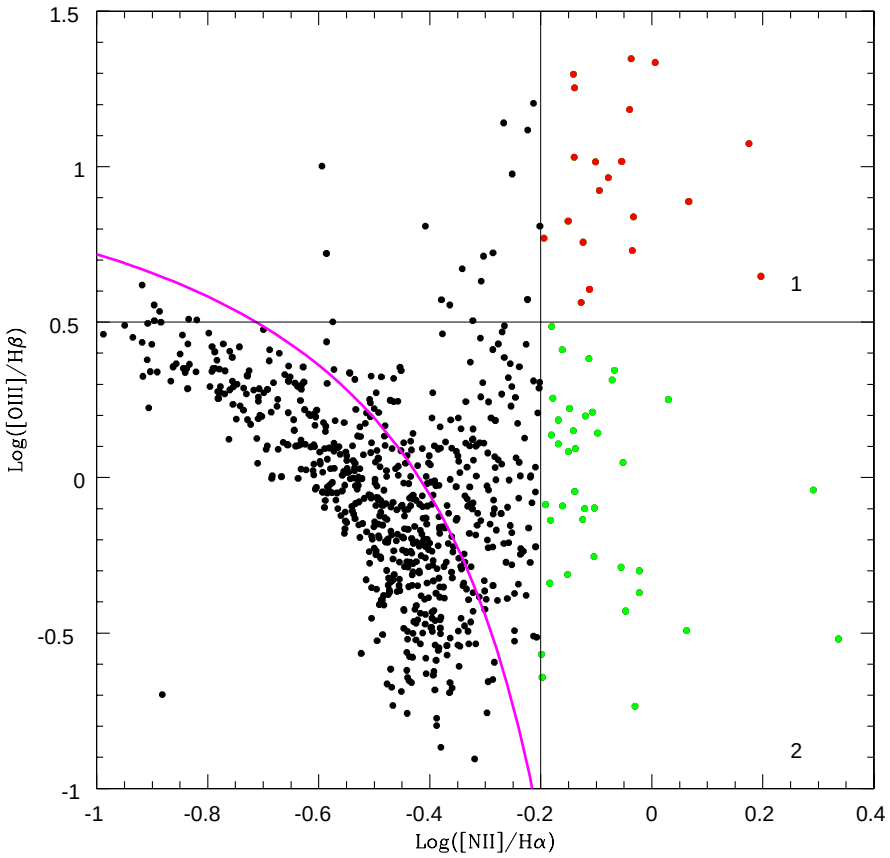

Figure 4.2: BPT diagram of distant void galaxies. Filled red circles in the top right corner (labeled 1) are the 'high confidence' AGNs ($\log([\mathrm{NII}]/\mathrm{H}\alpha) > -0.2$ and $\log([\mathrm{OIII}]/\mathrm{H}\beta) > 0.5$). Filled green circles in the bottom right (labeled 2) are the additional 45 AGNs ($\log([\mathrm{NII}]/\mathrm{H}\alpha) > -0.2$).

Chapter 5: Photometric Properties of Void Galaxies in the SDSS

To examine whether void and wall galaxies have different photometric properties, we compare their colors ($u-r$, $u-g$, and $g-r$), concentration indices, and Sersic indices. We compare the properties of wall and void galaxies in both the distant and nearby samples. We also subdivide each sample by absolute magnitude and compare their properties further. The samples compared are therefore, (1) Distant; bright ($M_r \leq -19.5$) [WGD_b, VGD_b], faint ($M_r > -19.5$) [WGD_f, VGD_f], and full (undivided) void vs. wall samples in each case respectively and (2) Nearby; bright ($M_r \leq -17.0$) [WGN_b, VGN_b], faint ($M_r > -17.0$) [WGD_f, VGD_f], and full (undivided) void vs. wall samples in each case respectively.

We compute the means of the distributions and also the error on the mean to see if on average void and wall galaxies have the same colors, concentration indices and Sersic indices. We also use the *Kolmogorov-Smirnov* (KS) test to see if the void and wall galaxies could be drawn from the same parent population.

Tables 1 and 2, summarize the results of these tests for the nearby and distant samples respectively. We present the results for the whole sample, as well as the samples split by absolute magnitude. The results are considered in detail below.

5.1 Color

The existence of strong correlations of galaxy type with density (Postman & Geller 1984; Dressler 1980), galaxy type with color (Strateva et al. 2001; Baldry et al. 2003), and density with luminosity and color (Hogg et al. 2002; Blanton et al. 2002) are well known; bright red galaxies tend to populate galaxy clusters and tend to be elliptical, while dim blue galaxies are less clustered and tend to be more disk like. This behavior is shown in an analysis of SDSS galaxy photometry by Blanton et al. (2002; see their Figures 7 and 8), in which they find that the distribution of $(g-r)$ colors at redshift 0.1 is bimodal.

Of particular interest to us is the location of the void galaxies in color space. Because these galaxies evolve more slowly and interact less with neighboring galaxies than their wall galaxy counterparts, we might expect void galaxies to be dim, blue, of low-mass and have high star formation rates (Benson et al. 2003). We consider three color indices: $u-r$, $u-g$ and $g-r$. The reason for these three colors is that $g-r$ measures the slope of the spectrum, $u-r$ is sensitive to the UV flux and the 4000Å break, and $u-g$ provides a consistency check for the other two colors. Since the u band magnitudes can be noisy, by looking at $g-r$, $u-g$ and $u-r$ we are able to verify that the results are consistent and not affected by low signal-to-noise ratio.

In Tables 1 and 2, we compare the photometric properties of the void galaxy samples to their respective wall galaxy samples. In Figures 5.1 and 5.2 we present normalized histograms of the color distributions. Solid lines correspond to the void galaxy samples and the dotted lines represent the wall galaxies. In all cases (nearby,

distant and the bright and faint sub-samples) we find that the void galaxy samples are on average bluer than the corresponding wall galaxy samples in both colors. If we look at the full samples, we find that the mean values of the two samples are significantly different. The nearby void galaxies have mean $u-r$, $u-g$ and $g-r$ colors that are at least $3\sigma_\mu$ bluer than the wall galaxy samples. For the distant void galaxies, the differences in the means are about four times greater than for the nearby case.

When we split the nearby sample into the bright and faint samples, we see that it is at the faint end where there is the greatest difference between void and wall galaxies. The significance of the KS test is reduced because of the smaller number of galaxies in each sample. The nearby bright and faint void galaxies are at least $2\sigma_\mu$ bluer than the wall galaxies. The differences between the nearby void and wall galaxies are not as pronounced as in the distant samples because we are shot noise limited by how many clusters there are in the small nearby volume. In the distant sample it is very unlikely that the wall and void galaxies in both the bright and faint sub-samples are drawn from the same parent population ($P < 10^{-4}$).

We assess the statistical significance of differences in the color distributions using a KS test (the values of P, the probability that the two samples are drawn from the same parent population, are given in the last column of Tables 1 and 2). The probability that the void and wall galaxies are drawn from the same parent population is low: $P < 0.002$ in the nearby case and $P < 10^{-4}$ in the distant case. In the distant sample it is very unlikely that the wall and void galaxies in both the bright and faint sub-samples are drawn from the same parent population ($P < 10^{-4}$).

5.2 Concentration Index

To compare morphological properties of void and wall galaxies, we examine the distribution of concentration indices measured by the SDSS photometric pipeline (Lupton et al. 2001; Stoughton et al. 2002; Pier et al. 2002; Lupton et al. 2002). The concentration index (CI) is defined by the ratio CI $\equiv$ r90/r50, where $r90$ and $r50$ correspond to the radii at which the integrated fluxes are equal to 90% and 50% of the Petrosian flux, respectively. A large value of CI corresponds to a relatively diffuse galaxy and a small value of CI to a highly concentrated galaxy. The concentration index has been shown to correlate well with galaxy type (Strateva et al. 2001; Shimasaku et al. 2001). Spiral galaxies are usually found to have small concentration indices ($\lesssim 2.5$) whereas ellipticals have larger concentration indices ($\gtrsim 2.5$). This bimodal behavior of the concentration index can be clearly seen in Strateva et al. (2001; see Figure 8).

Figure 5.3 shows histograms of CI for void and wall galaxies for both the nearby and distant samples along with the respective bright and faint sub-samples. Tables 1 and 2 show the mean, error on the mean, and the KS statistic found when comparing the wall and void galaxies.

In the nearby samples, the void and wall galaxies are not distinguished by this morphological parameter. In Table 1, we find that the mean values of CI are very similar. The probability that the distributions of concentration indices of void and wall sub-samples are drawn from the same parent population approaches unity and 0.5 for the faint and bright sub-samples respectively. The top row of plots in Figure 5.3, shows there is indeed little difference between the distributions of CI for the void

and wall galaxies in these samples.

We find that void galaxies have on average significantly smaller concentration indices in the bright half of the distant samples. There are more wall than void galaxies at large values of CI (CI $\gtrsim$ 2.5). The means differ by more than $7\sigma_\mu$. In Figure 5.3, in the bottom row, all three dotted curves show this behavior. In Table 2, it is clear that in the full sample and in the bright sample, the wall and void galaxies have significantly different CI distributions. A KS analysis of the bright sub-sample reveals that there is a probability of less than 10^{-4} that the void and wall galaxies are drawn from the same parent population. In the case of the distant faint void and wall galaxy samples the results are consistent.

5.3 Sersic Index

As another measure of morphology of void and wall galaxies we examine the Sersic index (Sersic 1968), found by fitting the functional form $I(r) = I_o exp(-r^{1/n})$, where n is the Sersic index itself, to each galaxy surface brightness profile (SBP). With this form, $n = 1$ corresponds to a purely exponential profile, while $n = 4$ is a de Vaucouleurs profile. We use the Sersic indices as measured by Blanton et al. (2002) for the SDSS galaxies.

In Figure 5.4, we plot histograms of Sersic indices measured for all the samples. Statistics of these distributions and the results of comparison of void and wall sub-samples are listed in Tables 1 and 2. In the nearby survey volume, we find $\bar{n} \lesssim 1.5$ for all void and wall galaxy sub-samples and there are no statistically significant

differences between the distributions. The top panels of Figure 5.4, show histograms of the Sersic index; the distributions of the void (solid lines) and wall (dotted line) galaxies appear very similar.

We find significant differences between void and wall galaxies in the distant samples. The lower panels in Figure 5.4, show the distribution of Sersic indices for the void and wall galaxies. For the more distant void galaxies, we find in Table 2, that $\bar{n}_{\rm Distant} = 1.7$, which is higher than what was found for the nearby void galaxies ($\bar{n}_{\rm Nearby} = 1.4$). A KS test reveals that the void galaxies are distinct from the wall galaxies with a probability of $P < 10^{-4}$ in the fainter ($M_r > -19.5$), brighter ($M_r < -20.3$) and full samples that the void and wall galaxies are drawn from the same parent population. The means of the Sersic indices of the void and wall galaxies differ by at least $3\sigma_\mu$. We show the number of wall galaxies as a function of Sersic index versus $g - r$ color in Figure 5.5. The y-axis is the Sersic index and the x-axis the $g - r$ color. The color intensities represent the number of galaxies in the two-dimensional bin. We can see that there are two prominent loci which correspond to blue-spirals (bottom left) and red-ellipticals (top right). For the nearby case, the bottom left region in Figure 5.5 would also include dE's since their colors, surface brightness profiles and, Sersic indices resemble those of blue spiral galaxies.

5.4 Discussion

The above analysis clearly shows that there is a difference in the photometric properties of void and wall galaxies. Void galaxies are fainter and bluer than wall galaxies

in all cases. Previous observational studies (e.g., Vennik et al. 1996; Pustilnik et al. 2002; Popescu et al. 1997) suggested that isolated galaxies in voids can be distinguished from non-void galaxies based on their color with a large enough sample. Here we provide such a sample and even extend the analysis to compare sub-samples of void and non-void galaxies of similar luminosity and SBP.

Nearby, the question might be raised as to whether it is the faintest void galaxies that are particularly blue and that these galaxies dominate the statistics. To test for this, the nearby sample is cut at -17.0, reducing the range of absolute magnitude in each bin and again the void galaxies are bluer than the wall galaxies. A further test was made where the galaxies were divided into bins of $\delta M = 1$ mag and still the void galaxies are bluer in every bin, thus the differences in color are not dominated by the tail of the distribution. Void galaxies are genuinely bluer than wall galaxies of the same luminosity.

In the distant sample the differences in color are only partly explained by the paucity of luminous red galaxies in voids. The average galaxy in the distant sample has an absolute magnitude of around -19.5 which is more than a magnitude fainter than an M^* galaxy in the r-band ($M^* = -20.80$ Blanton et al. 2001). Galaxies that are thought of as bright red cluster ellipticals are typically brighter than M^*. In the full sample, the faint sample and the bright sample (and in the $\delta M = 1$ mag test) void galaxies are still bluer than wall galaxies.

It may then be asked whether we are really finding a color difference between void and wall galaxies or whether we are just rediscovering the well known morphology-density relation, extrapolated down to lower densities: blue spiral galaxies are found

in low density environments, red ellipticals are found in clusters. However, nearby, the void and wall galaxies have very similar morphological mixes, at least as measured by the concentration and Sersic indices. There does not appear to be a significant difference in the morphological mix of galaxies between the void and wall samples. Yet still there is a difference in their colors.

In the distant sample the case is initially less clear. There is a morphological difference between the void and wall sample; there are more elliptical type galaxies in the wall sample. To test if the difference in color is just due to the paucity of ellipticals in voids, we divide the distant sample by Sersic index. Blanton et al. (2002) use $n < 1.5$ to represent exponential disks and $n > 3$ for the de Vaucouleurs profiles whereas Vennik et al. (1996) use $n \leq 1.5$ for exponential law fits and $n \geq 1.6$ for early type galaxy profile fitting. We look at the color distributions of void and wall galaxies with Sersic index less than 1.8 and greater than 1.8 to approximately split the sample into spirals and ellipticals. We find that the void galaxies with both $n < 1.8$ and $n > 1.8$ are bluer than the wall galaxies. In $u - r$ and $g - r$ and for both $n < 1.8$ and $n > 1.8$ the void galaxies are at least $3\sigma_\mu$ bluer than the wall galaxies, and for the $n < 1.8$, $g - r$ case the difference rises to $7\sigma_\mu$ (see Appendix for results). Again, the samples are divided into bright and faint sub-samples as well as by Sersic index. The void galaxies are always bluer than the wall galaxies, although the significance of the KS test is reduced because of the smaller number of galaxies.

Thus, void galaxies are bluer than wall galaxies even when compared at similar SBP and luminosities. They are also fainter and have surface brightness profiles that more closely resemble spirals than ellipticals. These findings are consistent with

predictions of void galaxy properties from a combination of Semi-Analytic Modeling and N-body simulations of structure formation in Cold Dark Matter models (Benson et al. 2003). One of the reasons why void galaxies are bluer than galaxies in richer environments may be that star formation is an ongoing process in void galaxies. Galaxies in clusters and groups have their supply of fresh gas cut off. Therefore, star formation is suppressed in the wall galaxies.

One question that should be addressed is what type of galaxies comprise our void galaxy samples. We are confident that the range of absolute magnitudes and Sersic indices spanned by the distant and nearby samples is large enough that a representative mix of different galaxy types e.g., the brightest members of the Local Group (LG), have been included in our samples. Local Group members like M31 and M33 can be detected in the distant sample, and fainter ($M_r \gtrsim -16.5$) members of the LG, like the LMC and SMC, would be included in the nearby sample.

In the nearby sample we can detect faint dwarf ellipticals (dE's), which is to be expected given that about 80% of the known galaxies in the LG are dwarfs (Sung et al. 1998; Staveley-Smith, Davies & Kinman al. 1992). It is well known that while dE's have exponential SBP's (Sandage & Binggeli 1984; Binggeli, Tammann & Sandage 1987; Caldwell & Bothun 1987) they exhibit color gradients that redden outward (Jerjen et al. 2000; Vader et al. 1988; Bremnes et al. 1998) and have a uniform color distribution (James 1994; Sung et al. 1998). Based on their color and other properties, a fraction of the void galaxies resemble a population of dwarf ellipticals (dE's), which have a mean $g - r = 0.51$ (Kniazev et al. 2003). Typical dE's have Sersic indices $n \sim 1.0$ and $M_B \gtrsim -17$, consistent with our sample of nearby void

galaxies (see Table 1).

5.5 Conclusions

Using a nearest neighbor analysis, we identify void galaxies in the SDSS. For the first time we have a sample of $\sim 10^3$ void galaxies. These void galaxies span a wide range of absolute magnitudes, $-13.5 > M_r > -22.5$, are found out to distances of $260h^{-1}$Mpc, and are found in regions of the universe that have density contrast $\delta\rho/\rho < -0.6$.

In previous studies of properties void galaxies it was suggested (Vennik et al. 1996; Pustilnik et al. 2002; Popescu et al. 1997) that void galaxies could be distinguished from non-void galaxies based on their color, and a hint of them being bluer was observed (Grogin & Geller (1999, 2000) from a small sample of void galaxies. In this paper we present a definitive result with a sample of 1204 void galaxies for which the colors, concentration and Sersic indices are compared against wall galaxies.

Void galaxies are bluer than wall galaxies of the same intrinsic brightness and redshift distribution down to $M_r = -13.5$. We demonstrate that the difference in colors is not explained by the morphology-density relation. Nearby, void and wall galaxies have very similar surface brightness profiles and still the void and wall galaxies have different colors. In the distant sample the voids and wall galaxies have different surface brightness profiles. However, when we divide the populations further by Sersic index, the void galaxies are still bluer. To test that the differences in color are not due to the choice of absolute magnitude range, we compare the colors within narrow bins of absolute magnitude. This reveals that void galaxies are genuinely blue and

that the differences between the colors are not dominated by extreme objects in the tails of the void and wall galaxy distributions.

Analysis of surface brightness profiles indicates that void galaxies are of later type than wall galaxies. Comparison of the Sersic indices between the distant void and wall galaxy samples including sub-samples within a narrow range of luminosities shows that it is very unlikely ($P < 10^{-4}$) that the two samples are drawn from the same parent population. However, based on the concentration index, it is only the bright distant void and wall galaxy samples that differ significantly.

Our results are in agreement with predictions from semi-analytic models of structure formation that predict void galaxies should be bluer, fainter, and have larger specific star formation rates (Benson et al. 2003). The differences in color are probably best explained in terms of star formation. Void galaxies are probably still undergoing star formation whereas wall galaxies have their supply of gas strangled as they fall into clusters and groups.

In a separate paper (Paper II; Rojas et al. 2004) we will discuss analysis of the spectroscopic properties (H_α, [OII] equivalent widths, and specific star formation rates) of our void galaxies. Work in progress reveals that the specific star formation rate of our void galaxies is considerably higher, consistent with our current findings and predictions.

Photometric Properties of Nearby Samples

Table 5.1: Means, errors on the means and KS test probabilities that the void and wall galaxies are drawn from the same parent population for the photometric properties of void and wall galaxies in the nearby sample ($r < 72h^{-1}$Mpc). The number of galaxies (void and wall) in each sample and sub-sample are listed next to the magnitude range heading as [N_V (void), N_W (wall)]. Small values of P correspond to a low probability that the two samples are drawn from the same parent population. The KS test shows that void galaxies appear to have different colors to wall galaxies. The void galaxies appear bluer than the respective wall galaxies in all cases, where the average difference between the means of the colors is about $2\sigma_\mu$. However, the concentration and Sersic indices are not significantly different.

Full ($-19.9 \leq M_r \leq -14.5$) [$N_V = 194$, $N_W = 2256$]

Property	Void (VGN) $\mu \pm \sigma_\mu$	Wall (WGN) $\mu \pm \sigma_\mu$	KS (P) Probability
$g-r$	0.433 ± 0.014	0.490 ± 0.004	0.002
$u-g$	1.193 ± 0.035	1.289 ± 0.011	0.007
$u-r$	1.598 ± 0.040	1.764 ± 0.013	0.001
$r90/r50$	2.390 ± 0.024	2.390 ± 0.007	0.802
n	1.388 ± 0.034	1.456 ± 0.004	0.506

Bright ($M_r \leq -17.0$) [$N_V = 76$, $N_W = 1071$]

Property	Void (VGN_b) $\mu \pm \sigma_\mu$	Wall (WGN_b) $\mu \pm \sigma_\mu$	KS (P) Probability
$g-r$	0.510 ± 0.019	0.549 ± 0.006	0.207
$u-g$	1.303 ± 0.050	1.395 ± 0.016	0.392
$u-r$	1.810 ± 0.063	1.930 ± 0.019	0.104
$r50/r90$	2.429 ± 0.044	2.421 ± 0.011	0.424
n	1.518 ± 0.060	1.626 ± 0.004	0.605

Faint ($M_r > -17.0$) [$N_V = 118$, $N_W = 1185$]

Property	Void (VGN_f) $\mu \pm \sigma_\mu$	Wall (WGN_f) $\mu \pm \sigma_\mu$	KS (P) Probability
$g-r$	0.383 ± 0.018	0.436 ± 0.006	0.003
$u-g$	1.121 ± 0.046	1.193 ± 0.015	0.074
$u-r$	1.459 ± 0.047	1.611 ± 0.016	0.018
$r50/r90$	2.366 ± 0.027	2.361 ± 0.008	0.918
n	1.305 ± 0.039	1.304 ± 0.006	0.509

Photometric Properties of Distant Samples

Table 5.2: Means, errors on the means and KS test probabilities that the void and wall galaxies are drawn from the same parent population for the photometric properties of void and wall galaxies in the distant sample ($100 \leq r \leq 260h^{-1}$Mpc). The number of galaxies (void and wall) in each sample and sub-sample are listed next to the magnitude range heading as [N_V (void), N_W (wall)]. Small values of P correspond to a low probability that the two samples are drawn from the same parent population. In this case, the KS test shows that the void and wall galaxies are drawn from different populations based on both color and morphology (concentration index and surface brightness profile). The differences between the means of the different parameters measured are on average $> 5\sigma_\mu$, except for the concentration index in the faint sub-sample, where the difference is $\sim 2\sigma_\mu$. Void galaxies are on average bluer and more disklike than wall galaxies.

Full ($-22.5 \leq M_r \leq -17.77$) [$N_V = 1010$, $N_W = 12732$]

Property	Void (VGD) $\mu \pm \sigma_\mu$	Wall (WGD) $\mu \pm \sigma_\mu$	KS (P) Probability
$g-r$	0.615 ± 0.007	0.719 ± 0.002	$< 10^{-4}$
$u-g$	1.359 ± 0.014	1.509 ± 0.004	$< 10^{-4}$
$u-r$	1.958 ± 0.018	2.219 ± 0.005	$< 10^{-4}$
$r90/r50$	2.449 ± 0.011	2.571 ± 0.004	$< 10^{-4}$
n	1.718 ± 0.024	2.051 ± 0.002	$< 10^{-4}$

Bright ($M_r \leq -19.5$) [$N_V = 409$, $N_W = 7831$]

Property	Void (VGD_b) $\mu \pm \sigma_\mu$	Wall (WGD_b) $\mu \pm \sigma_\mu$	KS (P) Probability
$g-r$	0.686 ± 0.009	0.765 ± 0.002	$< 10^{-4}$
$u-g$	1.457 ± 0.021	1.589 ± 0.005	$< 10^{-4}$
$u-r$	2.126 ± 0.026	2.343 ± 0.006	$< 10^{-4}$
$r90/r50$	2.505 ± 0.019	2.656 ± 0.004	$< 10^{-4}$
n	1.908 ± 0.042	2.285 ± 0.003	$< 10^{-4}$

Faint ($M_r > -19.5$) [$N_V = 601$, $N_W = 4901$]

Property	Void (VGD_f) $\mu \pm \sigma_\mu$	Wall (WGD_f) $\mu \pm \sigma_\mu$	KS (P) Probability
$g-r$	0.567 ± 0.009	0.645 ± 0.003	$< 10^{-4}$
$u-g$	1.292 ± 0.019	1.381 ± 0.007	$< 10^{-4}$
$u-r$	1.844 ± 0.024	2.020 ± 0.009	$< 10^{-4}$
$r90/r50$	2.411 ± 0.013	2.435 ± 0.005	0.211
n	1.589 ± 0.028	1.677 ± 0.003	$< 10^{-4}$

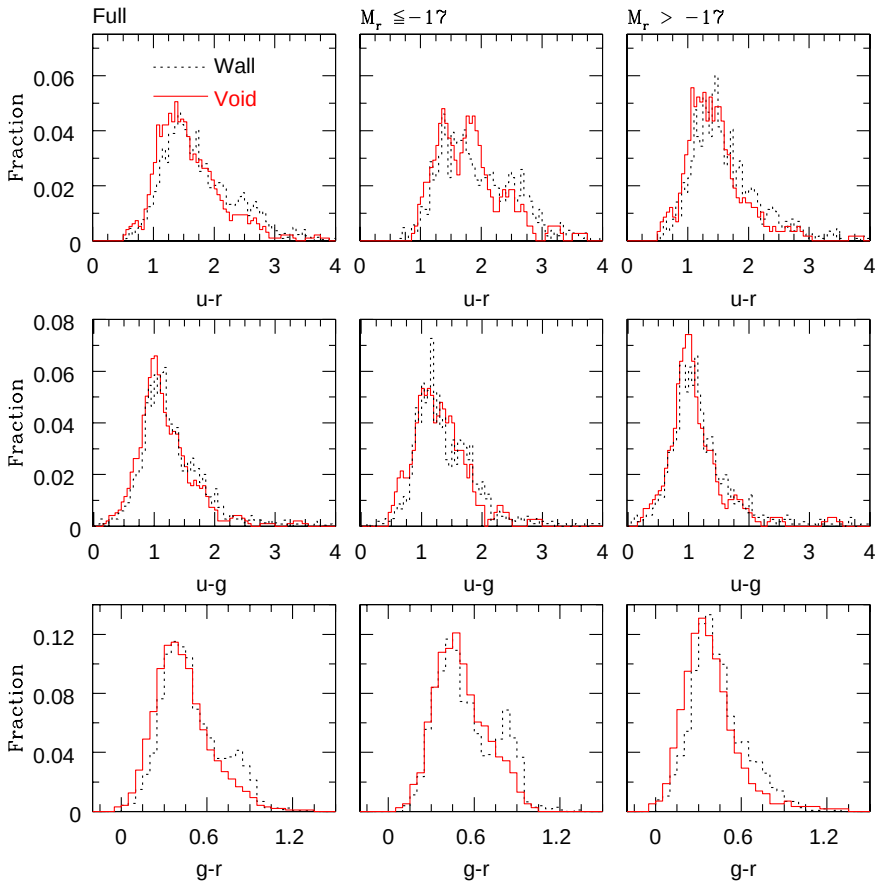

Figure 5.1: Color distributions of nearby void galaxies (solid lines) compared to the nearby wall galaxies (dotted lines) in three optical colors, $u-r$ (top row), $u-g$ (middle row) and $g-r$ (bottom row). The first, second and third columns are the undivided (full), bright ($M_r \leq -17$) and faint ($-17 < M_r$) samples respectively. The fraction of galaxies per 0.05 bin of color is shown on the Y-axis. In all cases, the solid curves are shifted to the left i.e., on average, the void galaxies are bluer than wall galaxies (see Table 1). A KS test reveals that in the case of the faint sub-sample and full sample it is very unlikely ($\bar{P} \lesssim 0.007$) that the full void and wall galaxy samples are drawn from the same respective parent populations. In the bright sub-sample, we see an excess of luminous red galaxies at $g-r \sim 0.9$ that is not present in the void galaxy histogram.

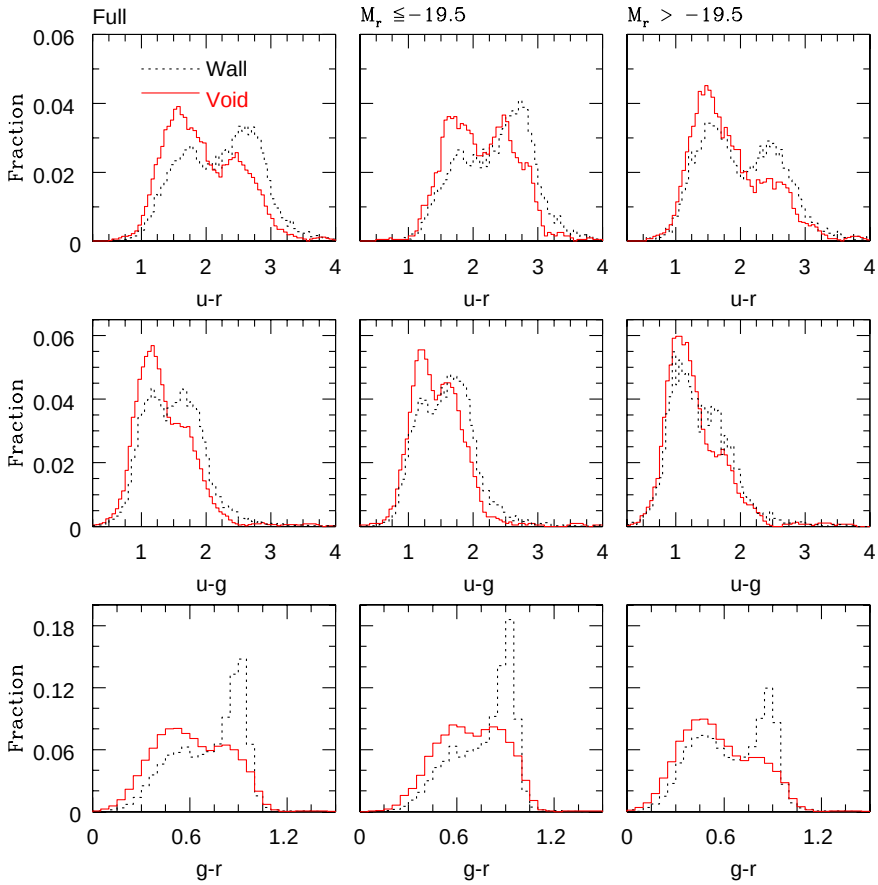

Figure 5.2: Color distributions of distant void galaxies (solid lines) compared to the distant wall galaxies (dotted lines) in three optical colors, $u-r$ (top row), $u-g$ (middle row) and $g-r$ (bottom row). The first, second and third columns are the undivided (full), bright ($M_r \leq -19.5$) and faint ($-19.5 < M_r$) samples respectively. The fraction of galaxies per 0.05 bin of color is shown on the Y-axis. In all cases, the solid curves are shifted to the left i.e., on average, the void galaxies are bluer than wall galaxies (see Table 2.). A KS test reveals that it is very unlikely ($P < 10^{-4}$) that the void galaxy and wall galaxy samples are drawn from the same parent populations. We clearly see an excess of luminous, red galaxies in the wall galaxy histograms as a peak at $g-r \sim 1.0$.

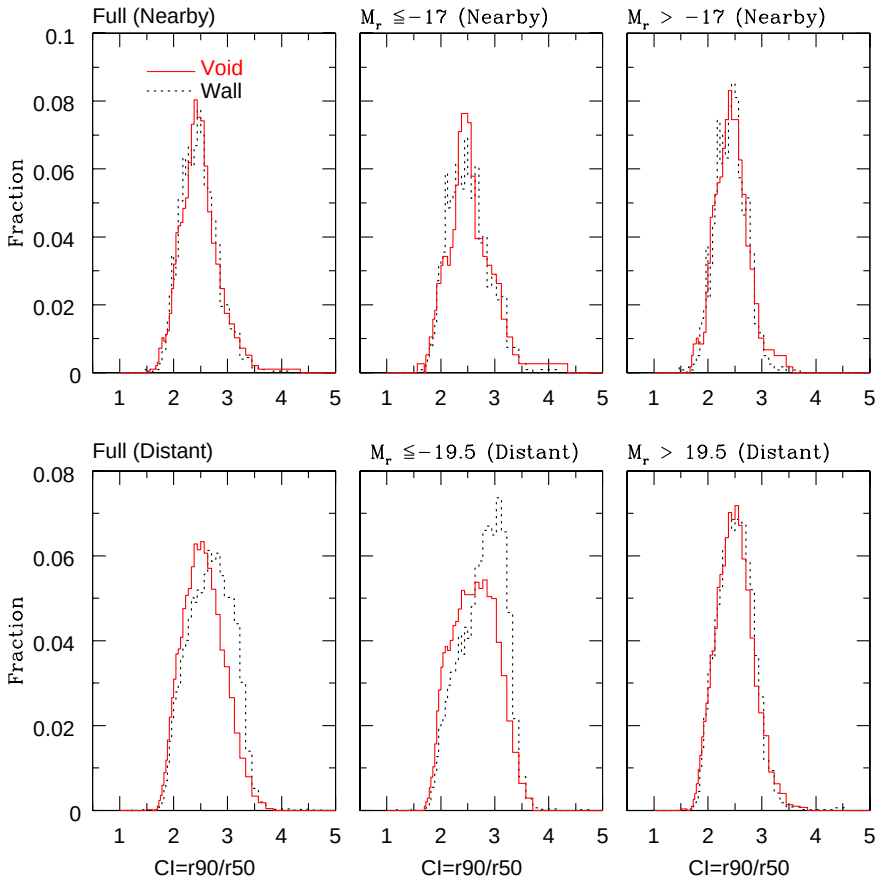

Figure 5.3: Concentration Index Distribution. We show the normalized fraction of void (solid lines) and wall galaxies (dotted lines) as a function of $r90/r50$. The top row shows the results for the nearby galaxies, the bottom row shows the results for the distant galaxies. The first, second and third columns are again the full, bright and faint samples. The fraction of galaxies per 0.1 bin of concentration index is shown on the Y-axis. The shift in the distribution for the distant, bright ($M_r \leq -19.5$) wall galaxies around $CI \sim 2.5$ corresponds to the excess of bright red galaxies in the wall samples. The KS statistic reveals that the distant void galaxy (bright and full) and respective wall galaxy samples are very different from one another, with a probability of $< 0.01\%$ that they are drawn from the same parent population. In the case of the nearby galaxies, the two distributions are indistinguishable.

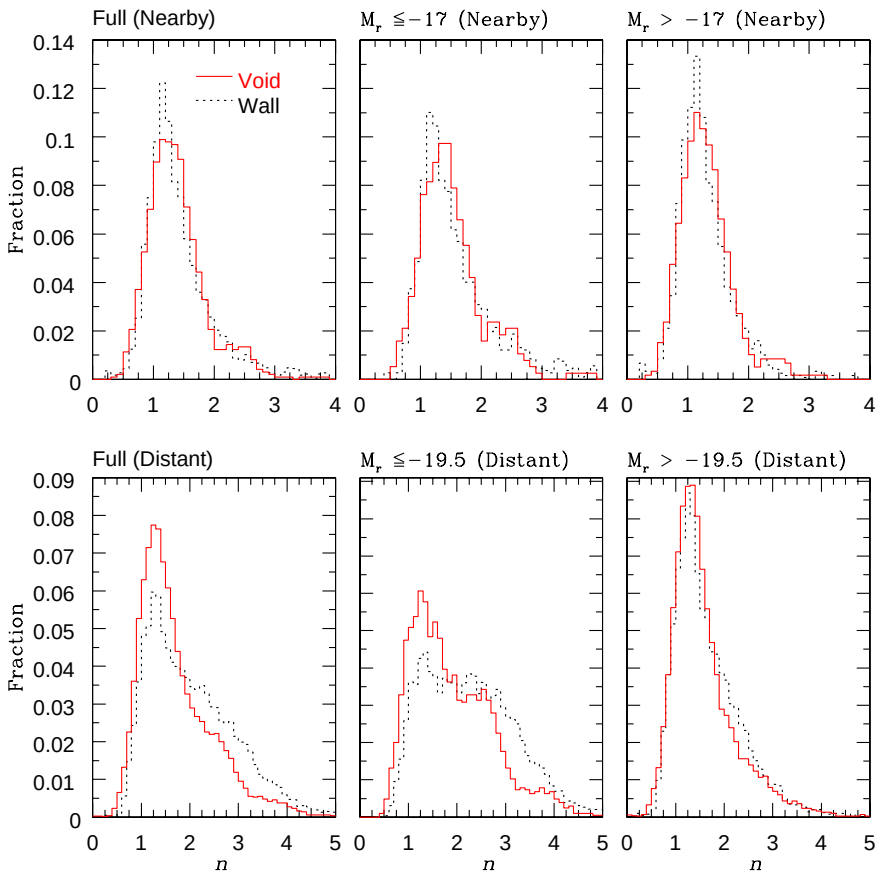

Figure 5.4: Sersic Index Distribution. We plot the normalized fraction of void (solid lines) and wall galaxies (dotted lines) as a function of Sersic index. The top row shows the results for the nearby galaxies, the bottom row shows the results for the distant galaxies. The first, second and third columns are again the full, bright and faint samples. The fraction of galaxies per 0.1 bin of Sersic index is shown on the Y-axis. We cannot distinguish the nearby void galaxies from the respective nearby wall galaxy sample based on the Sersic index. However, for the distant samples, the KS test assigns a probability of $P < 10^{-4}$ that the void galaxies are drawn from the same parent population as the respective wall galaxies.

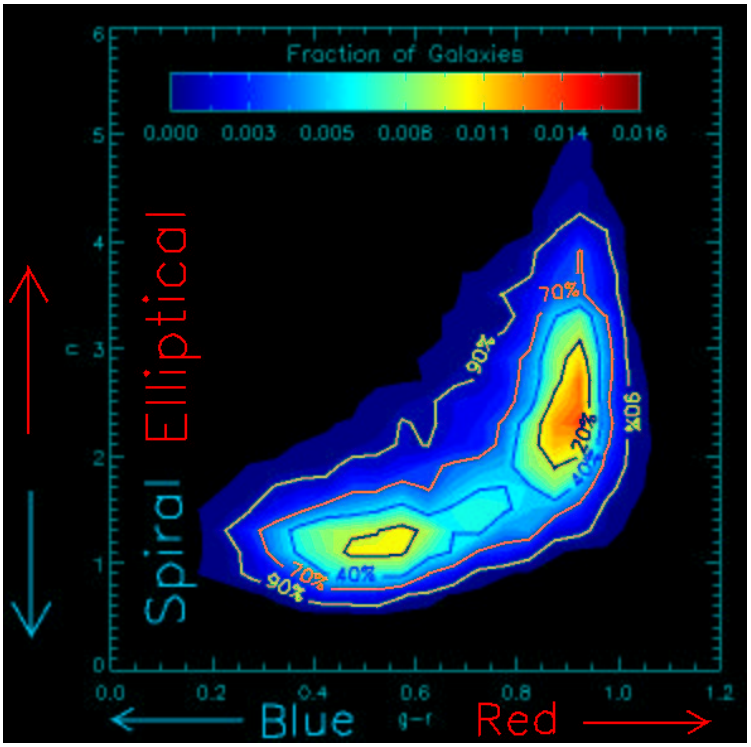

Figure 5.5: Number of distant wall galaxies as a function of Sersic index n and $g-r$ color. The color intensities correspond to the normalized number of galaxies in the two-dimensional bin. Red colors correspond to large numbers of galaxies and blue colors to smaller numbers in the respective bin. The two maxima that are observed; bottom left and top right contain predominantly late-type and early-type galaxies respectively.

Chapter 6: Spectroscopic Properties of Void Galaxies in the SDSS

To gain further clues about the differences between the properties of void and wall galaxies discussed in Rojas et al. (2003), we compare their Hα, [OII] λ3727, Hβ, [NII] λ6583, [OIII] λ5007 equivalent widths (EWs), stellar masses, 4000 Å Balmer break (ratio of the average flux density in the bands 4050-4250 and 3750-3950 Å, D(4000); Bruzual 1983) , and Hα and [OII] derived star formation (SFR) and specific star formation (S-SFR; SFR per unit stellar mass) rates. We choose these emission lines to examine a broad range of features in the spectra of our galaxies and star formation on different time scales. The EW([OII]) and 4000 Å Balmer break probe the blue end (3900-4800 Å) of the spectra, EW(Hβ) and EW([OIII]) probe the middle region (5000-6200 Å) and Hα and EW([NII]) probe the red end (6400-7500 Å) of the spectra. The Hα line probes star formation on timescales of $\sim 10^7$ years (e.g., lifetime of an HII region) and the strength of the 4000 Å break reflects on aging of the stellar population over timescales of $t \sim 1$ Gyr.

We use the emission line equivalent widths and the height and sigma of the Gaussian fit to the respective lines as measured by the SDSS spectral pipeline (`spectro1d`; SubbaRao et al, 2004). For the 4000 Å break strength we use Kauffmann et al's.

(2003a; K03a) estimates of of this index (D_n4000) which uses the ratio of average flux densities in narrower continuum bands (3850-3950 and 4000-4100 Å) as suggested by Balogh et al. (1999). About 70% of the stellar masses are obtained from K03a. They estimate the stellar masses by taking the product of the model predicted z-band stellar-mass-to-light ratio $(M/L)_z$ and the respective dust-corrected luminosity of the galaxy. The model used by K03a to predict the $(M/L)_z$ and stellar masses is based on median likelihood estimates from their library of Monte Carlo realizations of different star formation histories. We derive stellar masses for the remaining $\sim 30\%$ of galaxies as discussed below in Section 3.4. SFRs and S-SFRs are derived from the Hα and [OII] fluxes as discussed in detail in Sections 3.5 and 3.6 respectively.

We compute the means of the distributions and the error on the mean to compare the EWs, masses, SFRs, S-SFRs, and Dn4000s of void and wall galaxies. We also use the *Kolmogorov-Smirnov* (KS) test to test if the void and wall galaxies could be drawn from the same parent population based on the spectroscopic properties under consideration.

Tables 1 and 2 summarize the results of these tests for the nearby and distant samples respectively. We present results for the whole sample, as well as the samples split by absolute magnitude. The results are considered in detail below.

6.1 Hα Equivalent Width

Since the pioneering work of Kennicutt (1983) it has been demonstrated that large Hα equivalent widths are directly related to high star formation rates, bluer colors

and fainter absolute magnitudes (Kennicutt & Kent 1983). Recently Grogin & Geller (2000) showed that the EW(Hα)-density relation is most noticeable in either the lowest or highest density environments but that based on galaxy type and EW(Hα) one can not distinguish between the 'modest underdensities' ($0.5 < n/\bar{n} \leq 1$) and their control sample in 'modest overdensities' ($0.5 < \bar{n}/n \leq 1$)

EW(Hα) measures the ratio of flux from recent star formation (mainly flux from UV photons i.e, $\lambda < 912$ Å) to the integrated past star formation (predominantly flux from old stellar populations). Therefore, in the optical window the Hα emission line is an excellent diagnostic of star formation. When compared to other Balmer lines, the Hα emission line has several advantages that makes it an excellent choice for tracing the SFR of a galaxy at different redshifts. As pointed out by Tresse et al. (1999) the Hα line has a smaller dependence on chemical evolution because there is very little dependence on metallicity and is not affected by dust as much as the rest of the Balmer lines.

In Figure 6.1 we present normalized histograms of EW(Hα) for the nearby and distant samples. The solid lines correspond to the void galaxies and the dotted lines to the wall galaxies. In Tables 1 and 2, we compare the EW(Hα) of the various samples. In all cases[1] (bright, faint, late-type and early type) we find that void galaxies have on average larger EW(Hα) than wall galaxies of similar luminosity and type. If we compare the means of EWs of the distant sample (and sub-samples) we find that void galaxies have mean EW(Hα)s that are at least $5\sigma_{\mu}$ larger than wall galaxies.

[1]We divide our samples into late- and early-type using their Sersic index n as an indicator of morphology. Galaxies with $n \leq 1.8$ are considered late-type and galaxies with $n > 1.8$ early-type.

The statistical significance of the EW(Hα) differences between void and wall galaxies is quantified through a KS test. For the distant samples it is very unlikely that the void and wall galaxies are drawn from the same parent population ($P < 10^{-4}$). In the case of the nearby samples only the faint sub-sample shows a larger probability ($P = 0.37$) of being drawn from the same parent population. We attribute this in part to the the decrease in number of galaxies in this sample.

6.2 [OII] Equivalent Width

At higher redshifts the [OII] forbidden line is the most useful star formation tracer after Hα. This emission line is due to UV radiation ($\lambda < 730$ Å) produced by massive stars that ionizes heavier elements and therefore can be observed in the optical window for redshifts up to ~ 0.8 (Koo & Kron 1992). [OII] has the advantage that it is the most sensitive to blue luminosities and, hence is the most prominent emission line in the blue, especially for faint galaxies.

The [OII] emission line provides an independent diagnostic of the star formation history of galaxies since it is less affected by dust than Hα and is far enough from the Hα line ($\lesssim$ 3000Å apart). However, as pointed out by Koo and Kron (1992) the [OII] line's dependence on excitation and oxygen abundance makes it a less reliable measure of current star formation. Strong correlations between EW([OII])s and galaxy colors have been shown to exist for various galaxy types and redshifts. (Huchra 1977; Peterson et al. 1986; Broadhurst, Ellis, & Shanks 1988; Colless et al. 1990; Broadhurst, Ellis, & Glazerbrook 1992; Koo & Kron 1992). Therefore, even though the EW([OII])

has about half the flux as Hα it can still provide a complementary measure of the star formation history of our galaxy samples.

We find that for all the void galaxy samples and sub-samples under consideration the average value of EW([OII]) is significantly higher than for the respective wall galaxy samples. Figure 6.2 shows the normalized histograms of the EW([OII])s for void and wall galaxies for the distant sample along with the respective bright and faint sub-samples. It is important to note that in the nearby sample we do not have many measurements of EW([OII])s because only galaxies with redshifts $\gtrsim 0.02$ allow [OII] to be observed in the SDSS spectral wavelength coverage range. Tables 1 and 2 show the mean, error on the mean, and the KS statistic found when comparing the wall and void galaxies. We can see that the difference between EW([OII]) of void and wall galaxies is on average at least $5\sigma_\mu$ for the distant sample. In the nearby case, due to the small number of galaxies available it is difficult to statistically quantify the differences with high confidence. However, we can see that even with the reduced samples, void galaxies still have on average larger EW([OII]) than wall galaxies.

6.3 Hβ, [NII] and [OIII] Equivalent Widths

The Hβ and [OIII] emission lines not only provide a consistency check for the results discussed in the previous sections, but also allows us to gauge the spectroscopic properties of the void and wall galaxies at intermediate wavelengths between the blue and red. The [NII] line, although less intense than the Hα line, also probes the red end of the spectra and therefore serves as a complementary indicator of recent star

formation.

Once again we find that void galaxies have on average larger EWs than wall galaxies. Figures 6.3, 6.4 and 6.5 show the histograms of the EW(Hβ), EW([NII]), and EW([OIII]) distributions respectively. From Tables 1 and 2 it can be seen that on average the difference between void and wall galaxy EWs for Hβ, [NII] and [OIII] is about $5\sigma_{\mu}$. The fact that these three additional emission lines are consistent with Hα and [OII] results is an indication that void galaxies have higher specific star formation rates than wall galaxies of similar luminosities and type.

6.4 Stellar Masses

The integrated stellar masses for our samples are obtained from two sources: the primary source is from K03a's library of stellar masses and the secondary source uses a least squares fit to the stellar mass vs. z-band absolute magnitude relation. The z-band absolute magnitude is our preferred galaxy luminosity measure because it is less affected by extinction and less dependent on stellar age than the other four SDSS bands (u, g, r, i; Fukugita et al. 1996). The reason for obtaining the masses from two different sources is because K03a's library of stellar masses only includes a subset of DR1 (Abazajian 2003) and our samples are from a larger data base (Blanton et al. 2002; `sample10`). Therefore, for galaxies in our samples that are missing in K03a's list we need an alternate method to estimate the masses. Given that there is a nearly linear relationship between the z-band absolute magnitude and the logarithm of the estimated stellar mass, a least squares fit is a reasonable approach. Using this fit we

can measure typical stellar masses to within a factor of 10.

We find that our fit is in excellent agreement with K03a's estimate of the masses and proceed to complete the list of masses for our samples by applying this fit. In Figure 6.6 we plot K03a's masses vs. the z-band absolute magnitude. We can see that the scatter is well restricted to a narrow range about the line of best fit ($\mathrm{Log_{10}(mass/M_{\odot}) = -0.5134 M_z - 0.01581}$). To test how robust our mass estimates are, we compare the mean and error on the mean of the masses of the void and wall galaxies using a) only K03a's stellar masses, b) using K03a's masses with our estimates for the missing ones, and c) only using our linear fit applied to all the masses in the samples. In all three cases not only the relative values, but also the means and errors on the means are consistent. We therefore, use K03a's stellar masses for those galaxies in our sample that are included in their sample and apply the linear fit for those galaxies that are missing.

In Figure 6.7 we show the normalized histograms of the masses for all the samples. The differences between these distributions are listed in Tables 1 and 2. It can be readily seen in the distant sample that on average void galaxies have significantly smaller stellar masses than wall galaxies. From the KS test we conclude that it is very unlikely that void galaxies are drawn from the same parent population ($P < 10^{-4}$). However, in the nearby samples the mean values of the void and wall galaxy masses are very similar.

6.5 Star Formation Rates

In this section we discuss how star formation rates are derived and the relevant corrections applied. We employ the SDSS SFR prescription of Hopkins et al. (2003) with minor variations as discussed below.

Before estimating a SFR we need an estimate of the luminosity which in turn depends on the flux. Therefore, the first quantity that must be derived is the flux (F) associated with the height (κ) and width (σ) of the Gaussian fit to the respective line as measured by the SDSS spectroscopic data analysis pipeline:

$$F = \sqrt{2\pi}\sigma\kappa \times 10^{-17}\,[\mathrm{erg\ cm^{-2}\ s^{-1}}] \tag{6.1}$$

where κ is in units of [erg cm^{-2} s^{-1} Å] and σ in units of [Å]. The next step is to to compute the respective luminosity (L) using:

$$L = 4\pi D_L^2 F\,[\mathrm{erg\ s^{-1}}] \tag{6.2}$$

where D_L is the luminosity distance in units of [cm]. Finally, using Kennicutt's (1998b) formula for the Hα flux valid in the Case B recombination (Osterbrock 1986) with a Salpeter (1955) initial mass function, we compute the SFR from

$$\mathrm{SFR} = 7.9 \times 10^{-42} L\,[M_\odot\ yr^{-1}]. \tag{6.3}$$

Unfortunately, there exists at least four major systematics that must be accounted

for prior to computing the luminosities and corresponding SFRs. Excellent discussions of these systematics can be found in Gomez et al. (2002) and Hopkins et al. (2003). Below we provide a brief description of these biases and the steps taken to account for them in our estimates of the SFRs.

Following Hopkins' et al. (2003) methodology we begin by applying the stellar absorption correction. This consists of correcting the observed Balmer line equivalent width (EW) by a factor (EW_c) appropriate for the type of galaxy being studied. Hopkins et al. (2003) adopt a value of $\mathrm{EW}_c = 1.3$ Å for their analysis of the SDSS DR1(Abazajian et al. 2002) sample. Miller & Owen (2002) found that this correction varies from 0.9Å (E type) to 4.1Å (extreme spirals). In our case a correction of $\mathrm{EW}_c = 1.4$ Å is more appropriate for the morphological mix of our galaxies (C. Tremonti private communication). This correction is then converted to a flux correction via $F_c = \frac{\mathrm{EW}+\mathrm{EW}_c}{\mathrm{EW}}F$, where F is the observed line flux (Equation 1) and F_c the corrected line flux.

The next step is to correct the stellar absorption corrected flux F_c for aperture effects. Because emission detected through the 3″ fiber from a galaxy depends greatly on the redshift of the galaxy (nearby a smaller area of the galaxy is detected and at greater distances a larger area can be detected) we need to estimate the flux that would be measured within the Petrosian radius. This is accomplished by scaling F_c by the ratio of the continuum $r-$band flux in the fiber aperture and in the Petrosian aperture $10^{0.4(\mathrm{M}_{\mathrm{r(spec)}}-\mathrm{M}_{\mathrm{r(petro)}})}$ where $\mathrm{M}_{\mathrm{r(spec)}}$ and $\mathrm{M}_{\mathrm{r(petro)}}$ are the synthetic and Pet-

rosian[2] k-corrected SDSS r-band absolute magnitudes respectively. Therefore, the stellar absorption and aperture corrected flux (F_c') is

$$F_c' = F_c \times 10^{0.4(\mathrm{M_{r(spec)} - M_{r(petro)}})} [\mathrm{erg\ s^{-1}}]. \tag{6.4}$$

The final and largest correction (about a factor of 10) consists of accounting for obscuration by dust. Here we apply the Fitzpatrick (1998) parameterization and compute the color excess E(B-V) from the Balmer decrement given by $\tau_{\mathrm{Balmer}} = \ln[\frac{F_c'(\mathrm{H}\alpha)}{F_c'(\mathrm{H}\beta)}/2.87]$ where $F_c'(H\alpha)$ and $F_c'(H\beta)$ are the stellar absorption and aperture corrected Hα and Hβ fluxes respectively and:

$$\mathrm{E(B-V)} = 1.086\,\tau_{\mathrm{Balmer}}/1.17. \tag{6.5}$$

Note that for $F_c'(\mathrm{H}\beta)$ we use the g-band absolute magnitude when estimating the aperture corrections. For all other fluxes the r-band is used. With an estimate of the color excess for each galaxy we can now derreden the Hα, Hβ and [OII] fluxes using the R-dependent Galactic extinction curve of Fitzpatrick & Massa (1999). The dust corrected F_c' is now substituted into Equation 2. to compute the respective absorption, aperture, and dust corrected luminosity from which the SFR is derived using Equation 3.

---

[2]The magnitudes that are measured from the SDSS are Petrosian magnitudes (Petrosian 1976). The Petrosian magnitude is the total amount of flux within a circular aperture whose radius depends on the shape of the galaxy light profile, i.e., the size of the aperture is not fixed so galaxies of the same type are observed out to the same physical distance at all redshifts. More details are given in Stoughton et al. (2002). Synthetic magnitudes are magnitudes that are synthesized from the spectrum.

There still remains however, one more effect that has not been discussed, namely the effect of 'smearing' in the SDSS spectroscopic observing procedure (Stoughton et al. 2002). It consists of four minute spectroscopic observations performed while the telescope dithers for the purpose of correcting for light losses from the 3″ fiber aperture. For galaxies typically about 1/3 of their light is contained within the 3″ fiber aperture. Although the systematic differences between smear corrected and original spectra are only about 10% (Hopkins et al. 2003) the increase in the reported flux is generally about a factor of 2. Fortunately this was accounted for by using the r-band Petrosian magnitude in the aperture correction factor (this essentially scales the spectrum to match the photometry which is more reliable). An inherent assumption is that the EW(Hα) and reddening are constant across the whole galaxy.

Star Formation Rates from Hα and [OII]

Before estimating the SFRs we need to bear in mind that absorption and scattering of light by interstellar dust grains is the largest source of uncertainty. Significant underestimates of the derived SFRs would be expected if this effect were unaccounted for. In the case of SFRs derived from the [OII] line, the situation is even more severe because of the larger variation of $\tau_{\rm Balmer}$ (Gallagher et al. 1989; Kennicutt 1992a). This implies that SFRs of 'dustier' galaxies will have considerably larger corrections (increase in flux) than dust poor galaxies. We find that void galaxies are relatively dust poor and therefore, wall galaxies have the largest increase in flux due to reddening corrections. These corrections are quite significant: wall galaxies have an average factor of 13 increase in flux vs. void galaxies which have a factor

of 9 increase after all the relevant corrections are applied. Star formation rates are derived from Hα luminosities as discussed above using Equation 3. For the [OII] line we use Kennicutt's (1998) calibration:

$$\mathrm{SFR} = 1.4 \times 10^{-41} L\,[M_{\odot}\ yr^{-1}]. \tag{6.6}$$

We find that void and wall galaxies have similar Hα and [OII] derived SFRs both in the absence of dust corrections and with the applied reddening corrections. Because the stellar masses of void galaxies are smaller than wall galaxies, we expect that void galaxies are on average also smaller in size. This would explain the slightly lower SFRs observed in void galaxies. Figures 6.8 and 6.9 show the SFR(Hα) and SFR([OII]) normalized distributions for the void and wall galaxies. In the case of the Nearby samples, given the reasons discussed in Section 3.2 we are only able to estimate SFR([OII]) for a small number of galaxies. In Tables 1 and 2 we summarize the results from the SFR estimates. We can see that in the distant sample, the bright void galaxies have on average larger SFR(Hα) and SFR([OII]) than wall galaxies at the $3.5\sigma_{\mu}$ level, yet in the faint samples we find the opposite trend at the $1\sigma_{\mu}$ level (i.e., the SFR(Hα) of faint void and wall galaxies are roughly the same). When we split the samples by Sersic index we find that the early-type void galaxies have average larger SFR(Hα) and SFR([OII]) than wall galaxies, but that in the late-type sub-samples it is the wall galaxies that have larger SFRs.

When computing the means, errors on the means, and the KS statistic we include the negative SFRs in all the calculations. Negative SFRs are obtained when either

emission lines are seen as absorption lines or when the strength of the line is too weak and therefore, dominated by noise. The only SFRs that are not included are those for which an estimate of the color excess was not possible because $F'_c(\mathrm{H}\alpha)/\mathrm{F}'_c(\mathrm{H}\beta) < 0$. Our samples of void and wall galaxies are reduced in number by about 12% due to this restriction. However, these samples are large enough that even with this reduction we still have a statistically significant sample to perform our analysis.

6.6 Specific Star Formation Rates

The SFR per unit stellar mass (S-SFR) is perhaps a more informative spectral indicator for our purposes because void galaxies are on average less luminous and have smaller masses. By dividing the SFRs by the respective stellar masses we can discriminate better between the underlying physical processes that are taking place. We estimate the S-SFRs using the stellar masses and the absorption, aperture, and dust corrected SFRs as discussed in Sections 3.4 and 3.5 respectively. Consistent with our analysis of the SFRs, we include negative S-SFRs in the statistical calculations. Neither the negative SFRs or negative S-SFR have a physical meaning, yet the few 11% (void galaxies) and 22% (wall galaxies) that have S-SFRs< 0, if removed do bias our results (causes an artificial shift in the S-SFR distributions).

Specific Star Formation Rates from Hα and [OII]

In Figures 6.10 and 6.11 we show the S-SFR distributions for the Hα and [OII] lines respectively. In the case of the distant samples (bright and faint), including

sub-samples split by Sersic index, void galaxies have larger average S-SFR(Hα)s and S-SFR([OII])s than wall galaxies. The KS test shows that the probability of void and wall galaxies being derived from the same parent population is $< 10^{-4}$. The only case where this probability is higher is in the faint sub-sample where P(Hα)=0.054 and P([OII])=0.298 as shown in Table 1. For the nearby samples, since we do not have a complete list of SFR([OII])s we only discuss the S-SFR(Hα)s. In this case the wall galaxies have higher S-SFR(Hα)s than the void galaxies as can be seen in Table 2.

6.7 $\mathbf{D}_n(4000)$

As a final consistency check, we compare the strength of the 4000Å Balmer break of void and wall galaxies using K03a's measurements of this index (about 70% of our galaxies are included in K03a's list). The $D_n(4000)$ is an excellent spectral indicator of past star formation on timescales of $t \sim 1$Gyr and is also highly insensitive to dust attenuation effects. For hot stars where elements are multiply ionized the opacity decreases, therefore, hot, young stars (e.g., O and B) have lower amplitudes of $D_n(4000)$ than cooler, older stars (e.g., K and M; see Figure 3, Bruzual 1983). Since late-type galaxies are mainly composed of young stars, their 4000 Å break is smaller than for early-type galaxies which are primarily composed of older stellar populations.

In Figure 6.12 we show the distributions of $D_n(4000)$ for the void and wall galaxy samples. We can observe two noticeable features: (1) all samples of void galaxies have on average smaller $D_n(4000)$ than wall galaxies, as expected from the other properties measured, and (2) there is an obvious deficit of early-type galaxies in the nearby

samples which is observed in the amplitude of the distributions for $D_n(4000) \gtrsim 1.5$. From Tables 1 and 2 we can see that there is a very low probability ($P < 10^{-4}$) that the distributions of $D_n(4000)$ of void and wall galaxies (Distant and Nearby) are drawn from the same parent population.

6.8 Additional Tests

So far we have shown that on average void galaxies are bluer, more late-type, have higher specific star formation rates, and smaller masses than wall galaxies of similar luminosities and surface brightness profiles[3]. These results were obtained from comparing void and wall galaxies over broad bins in absolute magnitude and density. To verify that the differences between void and wall galaxies are genuine and not a consequence of comparing galaxies over broad bins in absolute magnitude and density space, we perform three additional tests. By comparing void and wall galaxies over narrow bins in absolute magnitude we can test whether the observed differences are due to the paucity of bright red galaxies in the void galaxy samples. In addition, the reduced statistical significance of the differences found in the nearby samples was attributed to the smaller number of galaxies available, by sparse sampling the distant samples to the same number of galaxies as in the nearby samples we can test whether this is the case. A final test is to compare void galaxies to low density wall galaxies using the third nearest neighbor as a measure of local density to examine the differences over a continuous range in density. Below we provide a brief outline of the tests

[3]We shall refer to these properties collectively as indicative of galaxies being 'voidier'.

followed by a detailed discussion of the results from each one.

1. Wall and void galaxies with absolute magnitudes in the range $-21.5 \leq M_r \leq -17.77$ are divided into 4 bins of 1 magnitude each. We then compare their properties within each bin of absolute magnitude.

2. We extract a sub-sample of wall galaxies from the distant wall sample based on their distance to the third nearest neighbor. We take the 25% of wall galaxies with the largest distance to the third nearest neighbor and compare their properties to void galaxies.

3. Both wall and void galaxy samples are sparse sampled to approximately the same number of galaxies as in the nearby wall and void samples respectively. We then compare properties between the two samples.

For the tests discussed above we choose the 3 most significant photometric ($g-r$, $u-r$, and Sersic index) and spectroscopic (EW(Hα), stellar mass, and specific star formation rate) parameters. We find that the same trend discussed above is observed in each test; void galaxies are voidier than wall galaxies regardless of the parameter space explored. Below we expand on the details of the results for each test.

6.8.1 Comparisons in Narrow Bins of Absolute Magnitude

A complementary test of the reliability of the differences between void and wall galaxies is to compare their properties over a narrow range of absolute magnitude. We therefore, compare several photometric and spectroscopic properties of void and wall

galaxies in bins of 1 magnitude from $M_r = -17.5$ to $M_r = -21.5$ for the distant samples. For the nearby samples the small number of void galaxies does not lend itself to this analysis. However, as shown in Table 6.3, we can see that void galaxies are considerably different from wall galaxies of similar luminosities even when compared within narrow bins of absolute magnitude. In the brightest and faintest bins the statistical significance is reduced because of the smaller number of void galaxies. This test shows that void galaxies are voidier than wall galaxies of similar luminosities at the $\sim 5\sigma_\mu$ level.

6.8.2 Low Density Wall Galaxies vs. Void Galaxies

To compare the properties of wall galaxies in low density environments to void galaxies, we extract a sub-sample from the wall galaxy sample based on a galaxy's distance to the third nearest neighbor (nn). All the wall galaxies are ranked according to their distance to their third nn. We then select the 25% whose third nn distances are the largest. Hereafter, we refer to this sample as the 'low density' wall sample. The next step is to compare the photometric and spectroscopic properties of void and low density wall galaxies using the same criteria discussed in Chapter 4. Therefore, we compare full samples and sub-samples split by absolute magnitude.

The distant low density wall sample has 3184 galaxies which divides into 1603 (faint) and 1581 (bright) when split by absolute magnitude at $M_r = -19.5$. In Table 6.4 we compare the results for a few photometric and spectroscopic properties. We can see that for all three cases (full, bright, and faint), void galaxies are still different when

compared to wall galaxies in low density environments (as defined by their distance to the third nn) and luminosities. Once again the significance of the differences is reduced because of the smaller size of the low density wall sample. However, it is clear that void galaxies are considerably voidier than low density wall galaxies at the $> 3\sigma_{\mu}$ level.

6.8.3 Sparse Sampling

For the nearby case in Chapters 5 and 6 we observe the same differences (i.e., void galaxies are voidier than wall galaxies), but at a lower statistical significance. We attribute this to the smaller number of galaxies in the samples. Therefore, to test this hypothesis, we sparse sample the distant void and wall galaxy samples to the same number of void and wall galaxies as in the nearby samples respectively. We then compare their properties and find that the differences still prevail but at a lower significance as expected. In Table 6.5 we show results of this test. We again see that void galaxies are voidier than wall galaxies but that the significance is reduced and comparable to that found when comparing the nearby samples.

6.9 Conclusions

Following our analysis in Rojas et al. (2003) we compare the spectroscopic properties of void and wall galaxies of similar luminosities and surface brightness profiles. We find that on average void galaxies have larger Hα, [OII], [NII], Hβ, and [OIII] equivalent widths, smaller masses, weaker 4000Å Balmer break and higher Hα specific star

formation rates than wall galaxies. Our analysis shows that our sample of void galaxies is less dusty and has slightly smaller average star formation rates than galaxies in more typical environments. This consistent with void galaxies being smaller and therefore, having less gas available for forming stars. The additional tests performed provide complementary evidence that the differences found between void and wall galaxies are genuine.

Our work is in agreement with other studies of smaller samples of void galaxies (Grogin & Geller 1999, 2000; Popescu et al. 1997, 1999; Pustilnik et al. 2002; Hopp et al. 1995) which have suggested that void galaxies are on average bluer and fainter than galaxies in more typical environments. However, there is disagreement with other studies that look at low and high density environments and do not find significant differences between galaxies in these environments (Hogg et al. 2004; Kauffmann et al. 2004; Balogh et al. 2003). This discrepancy is due to the fact that their analysis does not extend to such low density regions as ours.

The observed properties of void galaxies can be explained by two possible scenarios. On one hand, as suggested by Grogin & Geller (2002) the bluer colors of void galaxies are actually indicative of them being younger. On the other hand, the dark matter halos inside the voids could have formed at early times in order to form at all in such a low density environment. This is because as the voids expand and matter flows out towards the higher density regions, galaxies would never form inside the voids. As matter collapses in denser regions to form galaxies, the smaller gravitational potential of void galaxies (because of their smaller masses) allows them to evolve (consume their gas) at a slower pace as observed in their mean higher specific

star formation rates. Void galaxies can continue to form stars over longer periods of time due to the lack of tidal interactions that can suppress the flow of gas to the center of the galaxy. We could in principle test both possibilities by searching for void galaxies at larger redshifts (e.g., $z = 1$). If we fail to find void galaxies at large redshifts, then this would imply that void galaxies are younger and that predictions from hierarchical models of galaxy formation need to be revised.

NEARBY SAMPLE

Table 6.1: Means, errors on the means and KS test probabilities that the void and wall galaxies are drawn from the same parent population for the spectroscopic properties of void and wall galaxies in the nearby sample ($r < 72h^{-1}$Mpc). The number of galaxies (void and wall) in each sample and sub-sample are listed next to the magnitude range heading as [N_V (void), N_W (wall)]. Small values of P correspond to a low probability that the two samples are drawn from the same parent population. The KS test shows that void galaxies appear to have stronger emission line EWs than wall galaxies in all cases. The average difference between the means of the EWs and D_n4000s is about $2\sigma_\mu$. However, the SFRs and stellar masses are not significantly different. Only the bright void galaxy sub-sample shows a larger S-SFR(Hα) than wall galaxies.

Full ($-19.9 \leq M_r \leq -14.5$) [$N_V = 194$, $N_W = 2256$]

Property	Void (VGD) $\mu \pm \sigma_\mu$	Wall (WGD) $\mu \pm \sigma_\mu$	KS (P) Probability	[N_V, N_W]
EW(Hα) [Å]	35.31 ± 0.262	26.18 ± 0.645	0.0021	(187, 2202)
EW(Hβ) [Å]	7.317 ± 0.738	5.702 ± 0.242	0.0007	(192, 2226)
EW([NII]) [Å]	5.175 ± 0.338	4.298 ± 0.097	0.0611	(191, 2232)
EW([OIII]) [Å]	18.50 ± 2.111	14.17 ± 0.548	$< 10^{-4}$	(188, 2211)
$\mathrm{Log}_{10}(\mathrm{Mass}/M_\odot)$	8.692 ± 0.060	8.803 ± 0.018	0.0592	(194, 2256)
SFR(Hα) [$M_\odot/yr$]	0.162 ± 0.012	0.146 ± 0.006	0.3410	(183, 2020)
S-SFR(Hα) [yr^{-1}]	$(25.55 \pm 0.353) \times 10^{-11}$	$(31.70 \pm 0.169) \times 10^{-11}$	0.0001	(182, 2005)
D_n4000	1.261 ± 0.019	1.314 ± 0.005	$< 10^{-4}$	(119, 1545)

Bright ($M_r \leq -17.0$) [$N_V = 76$, $N_W = 1071$]

Property	Void (VGD_b) $\mu \pm \sigma_\mu$	Wall (WGD_b) $\mu \pm \sigma_\mu$	KS (P) Probability	[N_V, N_W]
EW(Hα) [Å]	33.316 ± 3.74	21.91 ± 0.809	0.0005	(76, 1060)
EW(Hβ) [Å]	5.939 ± 0.769	3.770 ± 0.210	0.0006	(76, 1055)
EW([NII]) [Å]	7.223 ± 0.733	5.203 ± 0.157	0.0034	(76, 1062)
EW([OIII]) [Å]	11.615 ± 2.41	8.276 ± 0.525	0.0133	(76, 1056)
$\mathrm{Log}_{10}(\mathrm{Mass}/M_\odot)$	9.333 ± 0.066	9.390 ± 0.018	0.4123	(76, 1071)
SFR(Hα) [$M_\odot/yr$]	0.323 ± 0.048	0.194 ± 0.011	0.0009	(73, 933)
S-SFR(Hα) [yr^{-1}]	$(17.57 \pm 3.222) \times 10^{-11}$	$(12.57 \pm 0.958) \times 10^{-11}$	$< 10^{-4}$	(73, 933)
D_n4000	1.287 ± 0.032	1.371 ± 0.008	$< 10^{-4}$	(50, 792)

Faint ($M_r > -17.0$) [$N_V = 118$, $N_W = 1185$]

Property	Void (VGD_f) $\mu \pm \sigma_\mu$	Wall (WGD_f) $\mu \pm \sigma_\mu$	KS (P) Probability	[N_V, N_W]
EW(Hα) [Å]	36.68 ± 3.60	30.14 ± 0.977	0.3740	(111, 1142)
EW(Hβ) [Å]	8.220 ± 1.111	7.443 ± 0.412	0.2920	(116, 1171)
EW([NII]) [Å]	3.821 ± 0.378	3.477 ± 0.121	0.4446	(115, 1170)
EW([OIII]) [Å]	23.17 ± 3.073	19.55 ± 0.905	0.0481	(112, 1155)
$\mathrm{Log}_{10}(\mathrm{Mass}/M_\odot)$	8.279 ± 0.060	8.273 ± 0.019	0.3589	(118, 1185)
SFR(Hα) [$M_\odot/yr$]	0.054 ± 0.006	0.098 ± 0.005	0.1725	(109, 1066)
S-SFR(Hα) [yr^{-1}]	$(29.19 \pm 4.527) \times 10^{-11}$	$(46.37 \pm 2.713) \times 10^{-11}$	0.0269	(109, 1066)
D_n4000	1.243 ± 0.022	1.253 ± 0.007	$< 10^{-4}$	(69, 753)

DISTANT SAMPLE

Table 6.2: Means, errors on the means and KS test probabilities that the void and wall galaxies are drawn from the same parent population for the spectroscopic properties of void and wall galaxies in the distant sample ($100 \leq r \leq 260h^{-1}$Mpc). The number of galaxies (void and wall) in each sample and sub-sample are listed next to the magnitude range heading as [N_V (void), N_W (wall)]. Small values of P correspond to a low probability that the two samples are drawn from the same parent population. In this case, the KS test shows that the void and wall galaxies are drawn from different populations based on emission line EWs, stellar masses, Hα and [OII] derived SFRs and S-SFRs, and D$_n$4000. The differences between the means of the different parameters measured are on average $> 5\sigma_\mu$, except for the SFR(Hα) and SFR([OII]) in the faint sub-sample, where the difference is $\sim 2\sigma_\mu$. Void galaxies on average have higher S-SFRs, larger EWs, smaller stellar masses and smaller D_n4000.

Full ($-22.5 \leq M_r \leq -17.77$) [$N_V = 1010$, $N_W = 12732$]

Property	Void (VGD) $\mu \pm \sigma_\mu$	Wall (WGD) $\mu \pm \sigma_\mu$	KS (P) Probability	[N_V, N_W]
EW(Hα) [Å]	19.14 ± 0.680	11.77 ± 0.158	$< 10^{-4}$	(1005, 12636)
EW([OII]) [Å]	14.26 ± 0.395	9.441 ± 0.093	$< 10^{-4}$	(1006, 12301)
EW(Hβ) [Å]	2.571 ± 0.146	0.828 ± 0.035	$< 10^{-4}$	(997, 12544)
EW([NII]) [Å]	6.553 ± 0.181	5.065 ± 0.049	$< 10^{-4}$	(1006, 12586)
EW([OIII]) [Å]	4.694 ± 0.335	2.197 ± 0.061	$< 10^{-4}$	(994, 12373)
$\mathrm{Log}_{10}(\mathrm{Mass}/M_\odot)$	10.13 ± 0.015	10.43 ± 0.004	$< 10^{-4}$	(1010, 12732)
SFR(Hα) $[M_\odot/yr]$	0.734 ± 0.025	0.747 ± 0.007	$< 10^{-4}$	(850, 8930)
SFR($[OII]$) $[M_\odot/yr]$	0.448 ± 0.015	0.488 ± 0.006	$< 10^{-4}$	(841, 8764)
S-SFR(Hα) $[yr^{-1}]$	$(3.744 \pm 0.108) \times 10^{-11}$	$(2.629 \pm 0.034) \times 10^{-11}$	$< 10^{-4}$	(850, 8930)
S-SFR([OII]) $[yr^{-1}]$	$(4.892 \pm 0.890) \times 10^{-11}$	$(3.020 \pm 0.251) \times 10^{-11}$	$< 10^{-4}$	(841, 8764)
D_n4000	1.515 ± 0.011	1.649 ± 0.003	$< 10^{-4}$	(714, 9862)

Bright ($M_r \leq -19.5$) [$N_V = 409$, $N_W = 7831$]

Property	Void (VGD_b) $\mu \pm \sigma_\mu$	Wall (WGD_b) $\mu \pm \sigma_\mu$	KS (P) Probability	[N_V, N_W]
EW(Hα) [Å]	14.47 ± 0.932	8.542 ± 0.175	$< 10^{-4}$	(406, 7774)
EW([OII]) [Å]	9.338 ± 0.429	6.884 ± 0.089	$< 10^{-4}$	(399, 7548)
EW(Hβ) [Å]	1.246 ± 0.201	0.018 ± 0.038	$< 10^{-4}$	(401, 7699)
EW([NII]) [Å]	6.606 ± 0.332	4.711 ± 0.066	$< 10^{-4}$	(407, 7743)
EW([OIII]) [Å]	2.706 ± 0.531	1.172 ± 0.055	$< 10^{-4}$	(401, 7574)
$\mathrm{Log}_{10}(\mathrm{Mass}/M_\odot)$	10.52 ± 0.016	10.70 ± 0.004	$< 10^{-4}$	(409, 7831)
SFR(Hα) $[M_\odot/yr]$	1.136 ± 0.063	0.920 ± 0.016	$< 10^{-4}$	(306, 4956)
SFR([OII]) $[M_\odot/yr]$	0.736 ± 0.051	0.626 ± 0.013	$< 10^{-4}$	(304, 4876)
S-SFR(Hα) $[yr^{-1}]$	$(3.133 \pm 0.169) \times 10^{-11}$	$(2.137 \pm 0.004) \times 10^{-11}$	$< 10^{-4}$	(306, 4956)
S-SFR([OII]) $[yr^{-1}]$	$(3.061 \pm 0.279) \times 10^{-11}$	$(2.192 \pm 0.053) \times 10^{-11}$	$< 10^{-4}$	(304, 4876)
D_n4000	1.602 ± 0.017	1.711 ± 0.004	$< 10^{-4}$	(287, 6069)

Faint ($M_r > -19.5$) [$N_V = 601$, $N_W = 4901$]

Property	Void (VGD_f) $\mu \pm \sigma_\mu$	Wall (WGD_f) $\mu \pm \sigma_\mu$	KS (P) Probability	[N_V, N_W]
EW(Hα) [Å]	22.31 ± 0.929	16.93 ± 0.287	$< 10^{-4}$	(599, 4862)
EW([OII]) [Å]	17.57 ± 0.554	13.50 ± 0.178	$< 10^{-4}$	(593, 4753)
EW($H\beta$) [Å]	3.452 ± 0.202	2.095 ± 0.067	$< 10^{-4}$	(531, 4334)
EW([NII]) [Å]	6.517 ± 0.204	5.630 ± 0.074	$< 10^{-4}$	(599, 4843)
EW([OIII]) [Å]	6.038 ± 0.423	3.817 ± 0.128	$< 10^{-4}$	(593, 4799)
$\mathrm{Log}_{10}(\mathrm{Mass}/M_\odot)$	9.873 ± 0.015	10.02 ± 0.005	$< 10^{-4}$	(601, 4901)
SFR(Hα) $[M_\odot/yr]$	0.508 ± 0.0237	0.530 ± 0.009	0.0254	(544, 3974)
SFR([OII]) $[M_\odot/yr]$	0.286 ± 0.017	0.316 ± 0.007	0.0298	(537, 3888)
S-SFR(Hα) $[yr^{-1}]$	$(4.146 \pm 0.137) \times 10^{-11}$	$(3.349 \pm 0.005) \times 10^{-11}$	$< 10^{-4}$	(544, 3974)
S-SFR([OII]) $[yr^{-1}]$	$(5.725 \pm 1.375) \times 10^{-11}$	$(4.058 \pm 0.147) \times 10^{-11}$	0.0034	(537, 3888)
D_n4000	1.456 ± 0.013	1.551 ± 0.004	$< 10^{-4}$	(427, 3793)

PHOTOMETRIC AND SPECTROSCOPIC PROPERTIES IN NARROW BINS OF M_r

Table 6.3: Means, errors on the means and KS test probabilities that the void and wall galaxies are drawn from the same parent population for selected photometric and spectroscopic properties of void and wall galaxies in the distant sample ($100 \leq r \leq 260h^{-1}$Mpc). Sub-samples of void and wall galaxies are compared in bins of 1 magnitude. The KS test shows that the void and wall galaxies are drawn from different populations based on color, morphology (surface brightness profile), Hα equivalent width, stellar mass, and, specific star formation rate. The differences between the means of the different parameters measured are on average $\sim 5\sigma_\mu$, except for the Sersic index in the faintest sub-sample.

	$(-21.5 \leq M_r < -20.5)$	$[N_V = 46,\ N_W = 2035]$	
Property	Void $\mu \pm \sigma_\mu$	Wall $\mu \pm \sigma_\mu$	KS (P) Probability
$g-r$	0.756 ± 0.023	0.822 ± 0.003	0.013
$u-r$	2.307 ± 0.068	2.524 ± 0.011	0.018
n	2.247 ± 0.115	2.733 ± 0.003	$< 10^{-4}$
EW(Hα) [Å]	7.777 ± 1.820	4.056 ± 0.252	0.0008
$\mathrm{Log}_{10}(\mathrm{Mass}/M_\odot)$	10.94 ± 0.029	11.03 ± 0.004	0.01752
S-SFR(Hα) $[yr^{-1}]$	$(1.329 \pm 0.324) \times 10^{-11}$	$(1.088 \pm 0.057) \times 10^{-11}$	0.54

	$(-20.5 \leq M_r < -19.5)$	$[N_V = 361,\ N_W = 5637]$	
Property	Void $\mu \pm \sigma_\mu$	Wall $\mu \pm \sigma_\mu$	KS (P) Probability
$g-r$	0.676 ± 0.011	0.741 ± 0.002	$< 10^{-4}$
$u-r$	2.099 ± 0.028	2.265 ± 0.007	$< 10^{-4}$
n	1.854 ± 0.042	2.096 ± 0.003	$< 10^{-4}$
EW(Hα) [Å]	15.397 ± 1.020	10.384 ± 0.220	$< 10^{-4}$
$\mathrm{Log}_{10}(\mathrm{Mass}/M_\odot)$	10.46 ± 0.013	10.55 ± 0.003	$< 10^{-4}$
S-SFR(Hα) $[yr^{-1}]$	$(3.353 \pm 0.178) \times 10^{-11}$	$(2.503 \pm 0.005) \times 10^{-11}$	0.0025

	$(-19.5 \leq M_r < -18.5)$	$[N_V = 453,\ N_W = 4073]$	
Property	Void $\mu \pm \sigma_\mu$	Wall $\mu \pm \sigma_\mu$	KS (P) Probability
$g-r$	0.583 ± 0.011	0.661 ± 0.003	$< 10^{-4}$
$u-r$	1.899 ± 0.027	2.056 ± 0.009	$< 10^{-4}$
n	1.618 ± 0.028	1.705 ± 0.003	0.0004
EW(Hα) [Å]	20.664 ± 0.972	16.200 ± 0.306	$< 10^{-4}$
$\mathrm{Log}_{10}(\mathrm{Mass}/M_\odot)$	9.995 ± 0.014	10.11 ± 0.005	$< 10^{-4}$
S-SFR(Hα) $[yr^{-1}]$	$(3.880 \pm 0.153) \times 10^{-11}$	$(3.235 \pm 0.066) \times 10^{-11}$	0.027

	$(-18.5 \leq M_r \leq -17.77)$	$[N_V = 142,\ N_W = 821]$	
Property	Void $\mu \pm \sigma_\mu$	Wall $\mu \pm \sigma_\mu$	KS (P) Probability
$g-r$	0.507 ± 0.018	0.564 ± 0.008	0.0013
$u-r$	1.647 ± 0.039	1.840 ± 0.021	0.0002
n	1.469 ± 0.040	1.540 ± 0.009	0.3323
EW(Hα) [Å]	27.583 ± 2.351	20.592 ± 0.778	0.004
$\mathrm{Log}_{10}(\mathrm{Mass}/M_\odot)$	9.516 ± 0.027	9.574 ± 0.011	0.0180
S-SFR(Hα) $[yr^{-1}]$	$(5.087 \pm 0.291) \times 10^{-11}$	$(3.933 \pm 0.134) \times 10^{-11}$	0.216

Table 6.4: Means, errors on the means and KS test probabilities that the void and low density wall galaxies (i.e., 25% of wall galaxies with the largest distance to their third nearest neighbor.) are drawn from the same parent population for the photometric properties of void and wall galaxies in the distant sample ($100 \leq r \leq 260h^{-1}$Mpc). The number of galaxies (void and wall) in each sample and sub-sample are listed next to the magnitude range heading as [N_V (void), N_W (wall)]. Small values of P correspond to a low probability that the two samples are drawn from the same parent population. In this case, the KS test shows that the void and low density wall galaxies are drawn from different populations based on color, Hα equivalent width, and specific star formation rate. The differences between the means of the different parameters measured are on average $> 3\sigma_\mu$, except for the Sersic index in the faint sub-sample, where the distributions are very similar. Overall the void galaxies are bluer, have higher EW(Hα), and higher specific star formation rates than low density wall galaxies in similar environments.

Full ($-22.5 \leq M_r \leq -17.77$) [$N_V = 1010$, $N_W = 3184$]

Property	Void (VGD) $\mu \pm \sigma_\mu$	Wall (WGD) $\mu \pm \sigma_\mu$	KS (P) Probability
$g-r$	0.615 ± 0.007	0.652 ± 0.004	$< 10^{-4}$
$u-r$	1.958 ± 0.018	2.039 ± 0.011	0.0004
n	1.718 ± 0.024	1.823 ± 0.008	0.0018
EW(Hα) [Å]	19.14 ± 0.680	16.16 ± 0.358	$< 10^{-4}$
$\mathrm{Log}_{10}(\mathrm{Mass}/M_\odot)$	10.13 ± 0.015	10.25 ± 0.013	$< 10^{-4}$
S-SFR(Hα) $[yr^{-1}]$	$(3.744 \pm 0.108) \times 10^{-11}$	$(3.231 \pm 0.063) \times 10^{-11}$	0.0003

Bright ($M_r \leq -19.5$) [$N_V = 409$, $N_W = 1581$]

Property	Void (VGD_b) $\mu \pm \sigma_\mu$	Wall (WGD_b) $\mu \pm \sigma_\mu$	KS (P) Probability
$g-r$	0.686 ± 0.009	0.715 ± 0.005	0.0012
$u-r$	2.126 ± 0.026	2.197 ± 0.014	0.0119
n	1.908 ± 0.042	2.068 ± 0.011	0.0088
EW(Hα) [Å]	14.47 ± 0.932	11.66 ± 0.441	0.0053
$\mathrm{Log}_{10}(\mathrm{Mass}/M_\odot)$	10.52 ± 0.016	10.59 ± 0.008	0.0017
S-SFR(Hα) $[yr^{-1}]$	$(3.133 \pm 0.169) \times 10^{-11}$	$(2.645 \pm 0.009) \times 10^{-11}$	0.0072

Faint ($M_r > -19.5$) [$N_V = 601$, $N_W = 1603$]

Property	Void (VGD_f) $\mu \pm \sigma_\mu$	Wall (WGD_f) $\mu \pm \sigma_\mu$	KS (P) Probability
$g-r$	0.567 ± 0.009	0.589 ± 0.005	0.04042
$u-r$	1.844 ± 0.024	1.881 ± 0.015	0.1785
n	1.589 ± 0.028	1.583 ± 0.010	0.82946
EW(Hα) [Å]	22.31 ± 0.929	20.606 ± 0.541	0.2472
$\mathrm{Log}_{10}(\mathrm{Mass}/M_\odot)$	9.873 ± 0.015	9.941 ± 0.009	0.0006
S-SFR(Hα) $[yr^{-1}]$	$(4.146 \pm 0.137) \times 10^{-11}$	$(3.768 \pm 0.009) \times 10^{-11}$	0.1044

SPARSE SAMPLED DISTANT WALL VS. VOID GALAXIES

Table 6.5: Means, errors on the means and KS test probabilities that the sparse sampled distant void and wall galaxies are drawn from the same parent population for a few photometric and spectroscopic properties of void and wall galaxies in the distant sample ($100 \leq r \leq 260h^{-1}$Mpc). The number of galaxies (void and wall) in each sample and sub-sample are listed next to the magnitude range heading as [N_V (void), N_W (wall)]. Small values of P correspond to a low probability that the two samples are drawn from the same parent population. In this case, the KS test shows that the distant void and wall samples when sparse sampled to match the number of nearby galaxies are drawn from different populations based on color, morphology (surface brightness profile), EW(Hα), stellar mass, and specific star formation rate. The differences between the means of the different parameters measured are on average $> 3\sigma_\mu$, void galaxies being voidier than wall galaxies.

Full ($-22.5 \leq M_r \leq -17.77$) [$N_V = 182$, $N_W = 2447$]

Property	Void (VGD) $\mu \pm \sigma_\mu$	Wall (WGD) $\mu \pm \sigma_\mu$	KS (P) Probability
$g-r$	0.627 ± 0.016	0.719 ± 0.004	$< 10^{-4}$
$u-r$	2.015 ± 0.041	2.216 ± 0.012	0.0005
n	1.725 ± 0.0529	2.049 ± 0.005	$< 10^{-4}$
EW(Hα) [Å]	19.14 ± 0.680	16.16 ± 0.358	$< 10^{-4}$
$\mathrm{Log}_{10}(\mathrm{Mass}/M_\odot)$	10.18 ± 0.035	10.43 ± 0.009	$< 10^{-4}$
S-SFR(Hα) [yr^{-1}]	$(3.508 \pm 0.249) \times 10^{-11}$	$(2.616 \pm 0.074) \times 10^{-11}$	0.0260

Bright ($M_r \leq -19.5$) [$N_V = 78$, $N_W = 1485$]

Property	Void (VGD_b) $\mu \pm \sigma_\mu$	Wall (WGD_b) $\mu \pm \sigma_\mu$	KS (P) Probability
$g-r$	0.706 ± 0.021	0.764 ± 0.004	0.0278
$u-r$	2.178 ± 0.056	2.336 ± 0.014	0.0557
n	1.941 ± 0.089	2.287 ± 0.005	0.0014
EW(Hα) [Å]	14.25 ± 2.121	8.301 ± 0.396	0.0007
$\mathrm{Log}_{10}(\mathrm{Mass}/M_\odot)$	10.52 ± 0.038	10.69 ± 0.009	0.0002
S-SFR(Hα) [yr^{-1}]	$(2.542 \pm 0.339) \times 10^{-11}$	$(2.029 \pm 0.009) \times 10^{-11}$	0.0983

Faint ($M_r > -19.5$) [$N_V = 601$, $N_W = 1603$]

Property	Void (VGD_f) $\mu \pm \sigma_\mu$	Wall (WGD_f) $\mu \pm \sigma_\mu$	KS (P) Probability
$g-r$	0.567 ± 0.021	0.652 ± 0.007	0.0404
$u-r$	1.893 ± 0.056	2.029 ± 0.015	0.0197
n	1.563 ± 0.059	1.683 ± 0.007	0.0395
EW(Hα) [Å]	22.52 ± 2.242	16.09 ± 0.595	0.1175
$\mathrm{Log}_{10}(\mathrm{Mass}/M_\odot)$	9.919 ± 0.034	10.019 ± 0.111	0.0623
S-SFR(Hα) [yr^{-1}]	$(4.200 \pm 0.329) \times 10^{-11}$	$(3.434 \pm 0.119) \times 10^{-11}$	0.0428

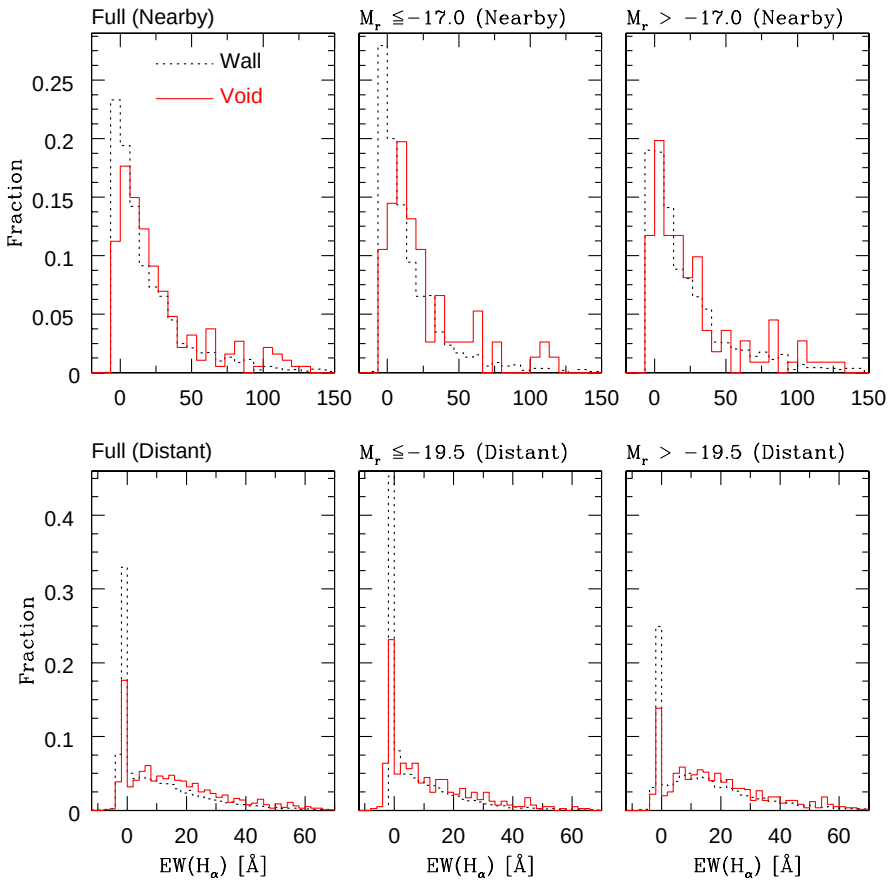

Figure 6.1: Distribution of Hα equivalent widths. We show the normalized fraction of void (solid lines) and wall galaxies (dotted lines) as a function of EW(Hα). The top row shows the results for the nearby ($r < 72h^{-1}$Mpc) galaxies, the bottom row shows the results for the distant ($100 \leq r \leq 260h^{-1}$Mpc) galaxies. The first, second and third columns are the full, bright and faint samples. The fraction of galaxies per 6.5Å (nearby) and 2Å (distant) bin of EW(Hα) is shown on the Y-axis. The KS statistic reveals that the distant void galaxy (bright, faint, and full) and respective wall galaxy samples are very different from one another, with a probability of $< 0.01\%$ that they are drawn from the same parent population. In the case of the nearby galaxies, only the faint galaxy distributions (top right panel) have a higher probability ($P \lesssim 0.37$) of being similar.

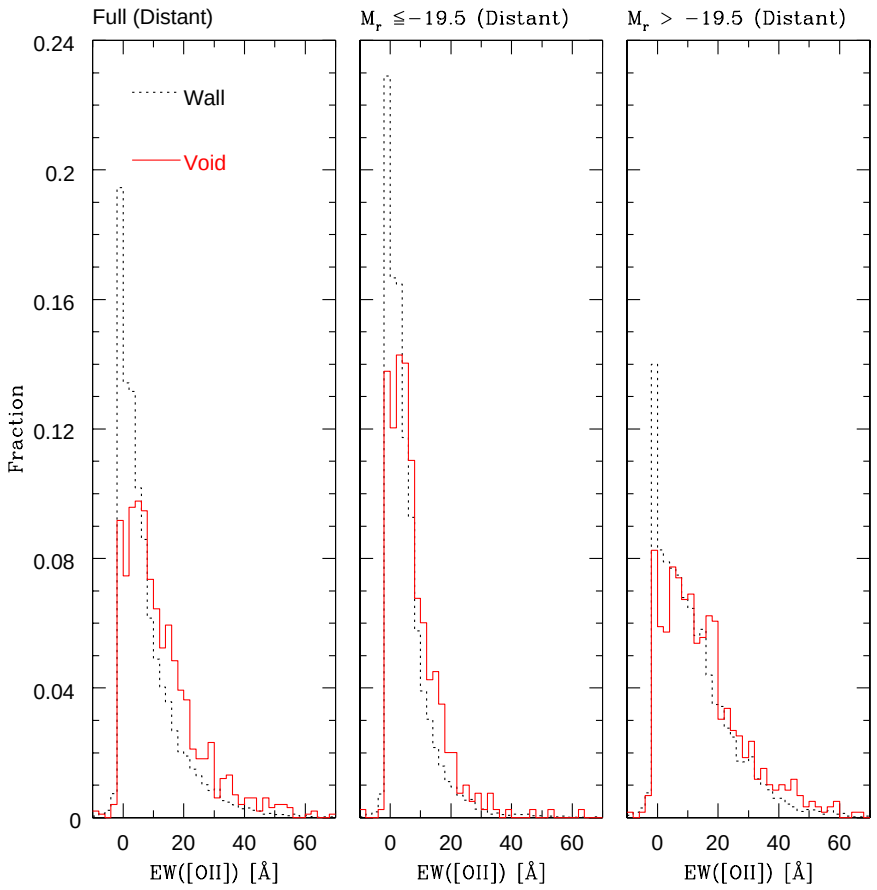

Figure 6.2: Distribution of [OII] equivalent widths. We show the normalized fraction of void (solid lines) and wall galaxies (dotted lines) as a function of EW([OII]). The first, second and third columns are the full, bright and faint distant samples. The fraction of galaxies per 2Å bin of EW([OII]) is shown on the Y-axis. The KS statistic reveals that the distant void galaxy (bright, faint, and full) and respective wall galaxy samples are very different from one another, with a probability of $< 0.01\%$ that they are drawn from the same parent population.

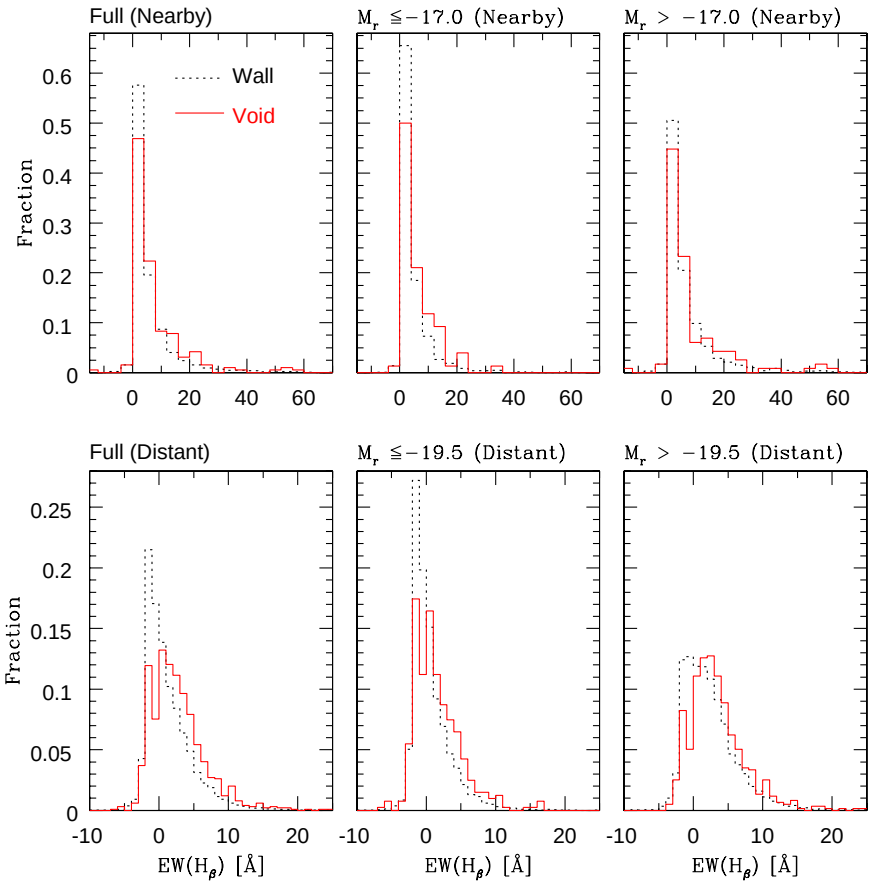

Figure 6.3: Distribution of Hβ equivalent widths. We show the normalized fraction of void (solid lines) and wall galaxies (dotted lines) as a function of EW(Hβ). The top row shows the results for the nearby ($r < 72h^{-1}$Mpc) galaxies, the bottom row shows the results for the distant ($100 \leq r \leq 260h^{-1}$Mpc) galaxies. The first, second and third columns are the full, bright and faint samples. The fraction of galaxies per 4Å (nearby) and 1Å (distant) bin of EW(Hβ) is shown on the Y-axis. The KS statistic reveals that the distant void galaxy (bright, faint, and full) and respective wall galaxy samples are very different from one another, with a probability of $< 0.01\%$ that they are drawn from the same parent population. In the case of the nearby galaxies, only the faint galaxy distributions (top right panel) have a higher probability ($P \lesssim 0.29$) of being similar.

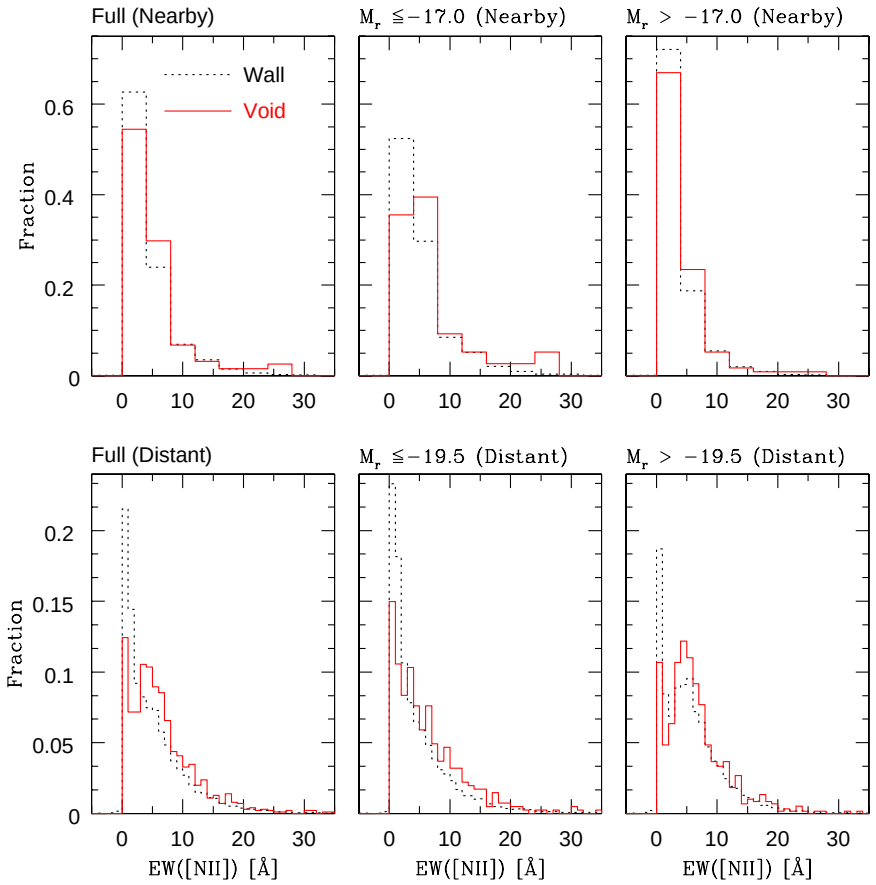

Figure 6.4: Distribution of [NII] equivalent widths. We show the normalized fraction of void (solid lines) and wall galaxies (dotted lines) as a function of EW([NII]). The top row shows the results for the nearby ($r < 72h^{-1}$Mpc) galaxies, the bottom row shows the results for the distant ($100 \leq r \leq 260h^{-1}$Mpc) galaxies. The first, second and third columns are the full, bright and faint samples. The fraction of galaxies per 2.8Å (nearby) and 1Å (distant) bin of EW([NII]) is shown on the Y-axis. The KS statistic reveals that the distant void galaxy (bright, faint, and full) and respective wall galaxy samples are very different from one another, with a probability of $< 0.01\%$ that they are drawn from the same parent population. In the case of the nearby galaxies, only the faint galaxy distributions (top right panel) have a higher probability ($P \lesssim 0.44$) of being similar.

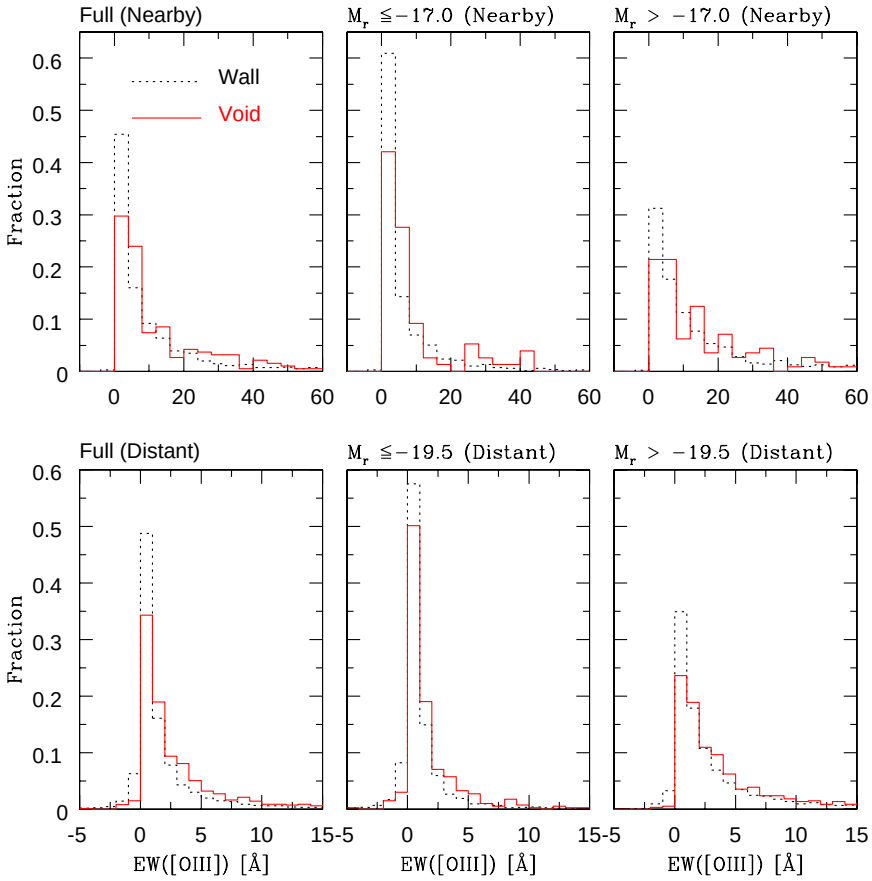

Figure 6.5: Distribution of [OIII] equivalent widths. We show the normalized fraction of void (solid lines) and wall galaxies (dotted lines) as a function of EW([OIII]). The top row shows the results for the nearby ($r < 72h^{-1}$Mpc) galaxies, the bottom row shows the results for the distant ($100 \leq r \leq 260h^{-1}$Mpc) galaxies. The first, second and third columns are the full, bright and faint samples. The fraction of galaxies per 4Å (nearby) and 1Å (distant) bin of EW([OIII]) is shown on the Y-axis. The KS statistic reveals that the distant void galaxy (bright, faint, and full) and respective wall galaxy samples are very different from one another, with a probability of $< 0.01\%$ that they are drawn from the same parent population. In the case of the nearby galaxies, only the faint galaxy distributions (top right panel) have a higher probability ($P \lesssim 0.05$) of being similar.

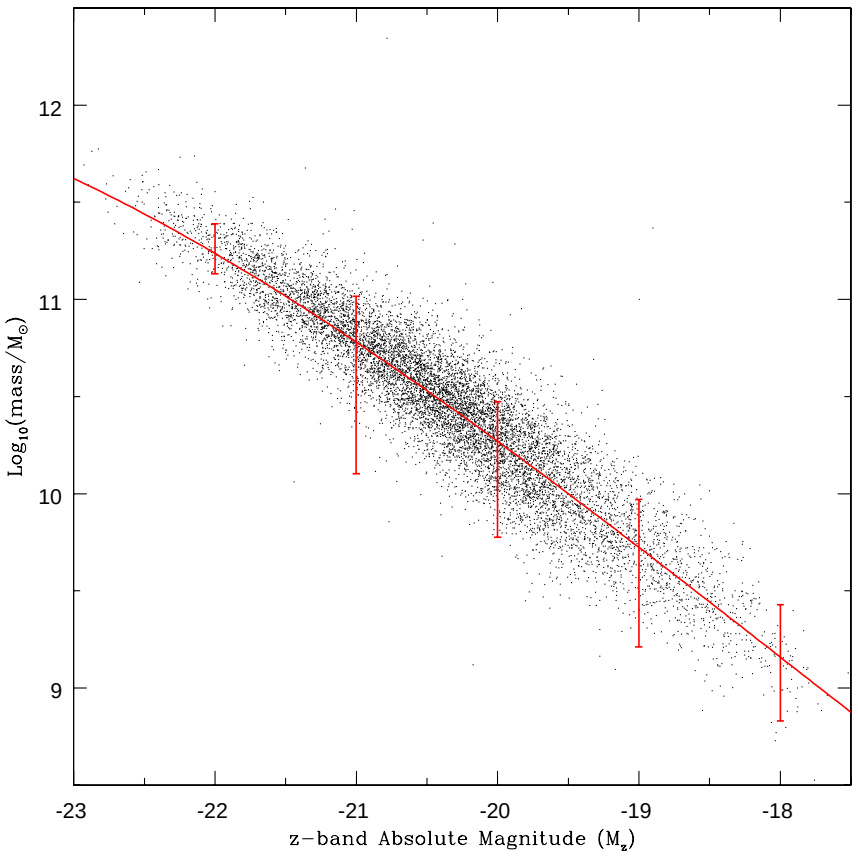

Figure 6.6: Plot of $\mathrm{Log}_{10}(\mathrm{Mass}/\mathrm{M}_{\odot})$ vs. z-band absolute magnitude using Kauffmanns et al's (2003) stellar masses (points). Error bars are the 1σ errors of stellar masses in bins $\Delta M_z = 1$ wide. The solid line is a least squares fit. We use this linear fit to estimate the stellar masses of other galaxies in our sample using their z-band flux.

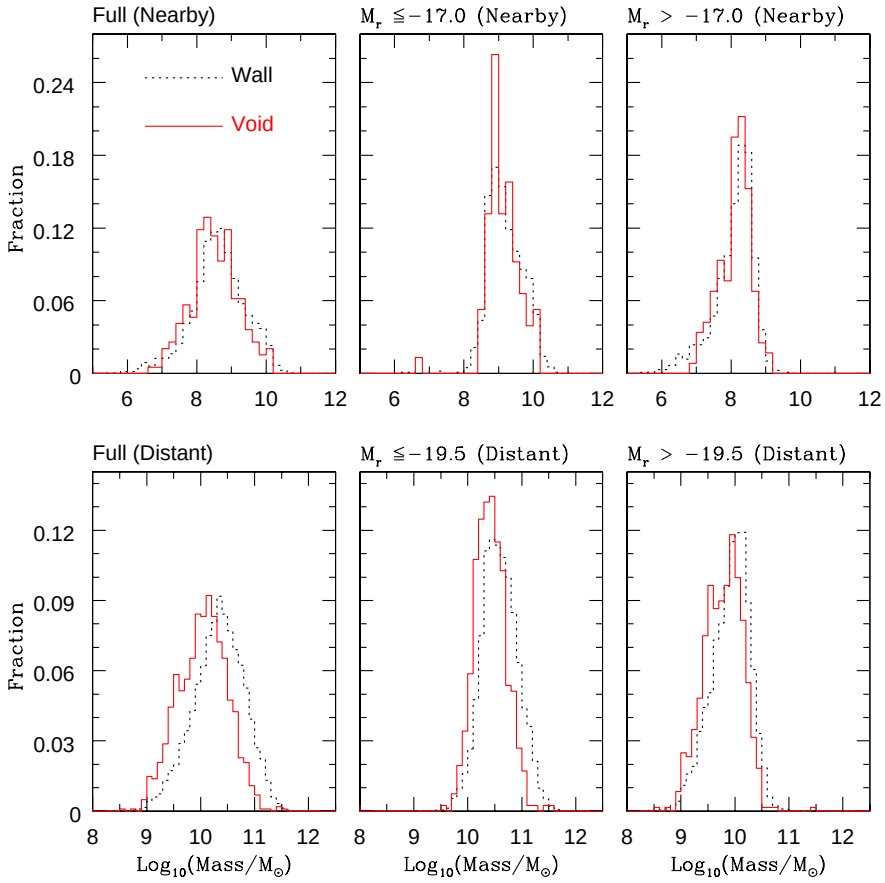

Figure 6.7: Stellar Mass Distribution. We show the normalized fraction of void (solid lines) and wall galaxies (dotted lines) as a function of $\mathrm{Log}_{10}(\mathrm{Mass/M}_{\odot})$. The top row shows the results for the nearby ($r < 72h^{-1}$Mpc) galaxies, the bottom row shows the results for the distant ($100 \leq r \leq 260h^{-1}$Mpc) galaxies. The first, second and third columns are the full, bright and faint samples. The fraction of galaxies per $5M_{\odot}$ (nearby) and $10M_{\odot}$ (distant) bin of $\mathrm{Log}_{10}(\mathrm{Mass/M}_{\odot})$ is shown on the Y-axis. The KS statistic reveals that the distant void galaxy (bright, faint, and full) and respective wall galaxy samples are very different from one another, with a probability of $< 0.01\%$ that they are drawn from the same parent population. In the case of the nearby galaxies, only the bright galaxy distributions have a higher probability ($P \lesssim 0.36$) of being similar.

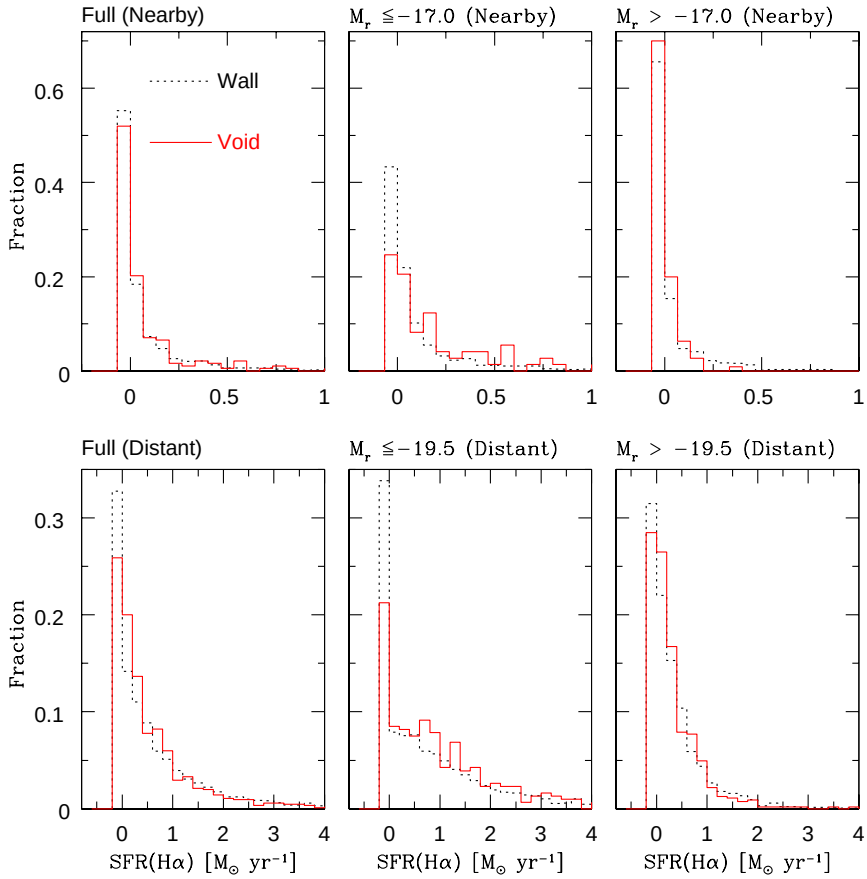

Figure 6.8: Distribution of Hα star formation rates. We show the normalized fraction of void (solid lines) and wall galaxies (dotted lines) as a function of SFR(Hα). The top row shows the results for the nearby ($r < 72h^{-1}$Mpc) galaxies, the bottom row shows the results for the distant ($100 \leq r \leq 260h^{-1}$Mpc) galaxies. The first, second and third columns are the full, bright and faint samples. The fraction of galaxies per $0.067 M_{\odot}\,\mathrm{yr}^{-1}$ bin of SFR(Hα) is shown on the Y-axis. The KS statistic reveals that the distant void galaxy (bright and full) and respective wall galaxy samples are very different from one another, with a probability of $< 0.01\%$ that they are drawn from the same parent population.

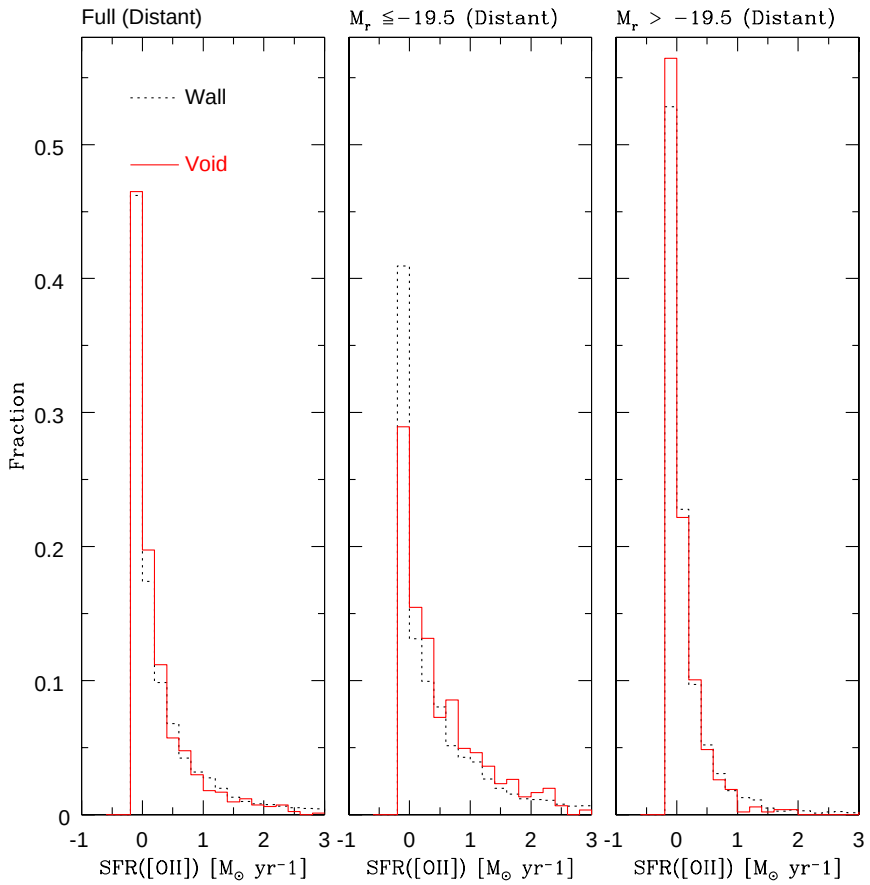

Figure 6.9: Distribution of [OII] star formation rates. We show the normalized fraction of void (solid lines) and wall galaxies (dotted lines) as a function of SFR([OII]). The first, second and third columns are the full, bright and faint distant samples. The fraction of galaxies per $0.067 M_{\odot}\,\mathrm{yr}^{-1}$ bin of SFR([OII]) is shown on the Y-axis. The KS statistic reveals that the distant void galaxy (bright and full) and respective wall galaxy samples are very different from one another, with a probability of $< 0.01\%$ that they are drawn from the same parent population.

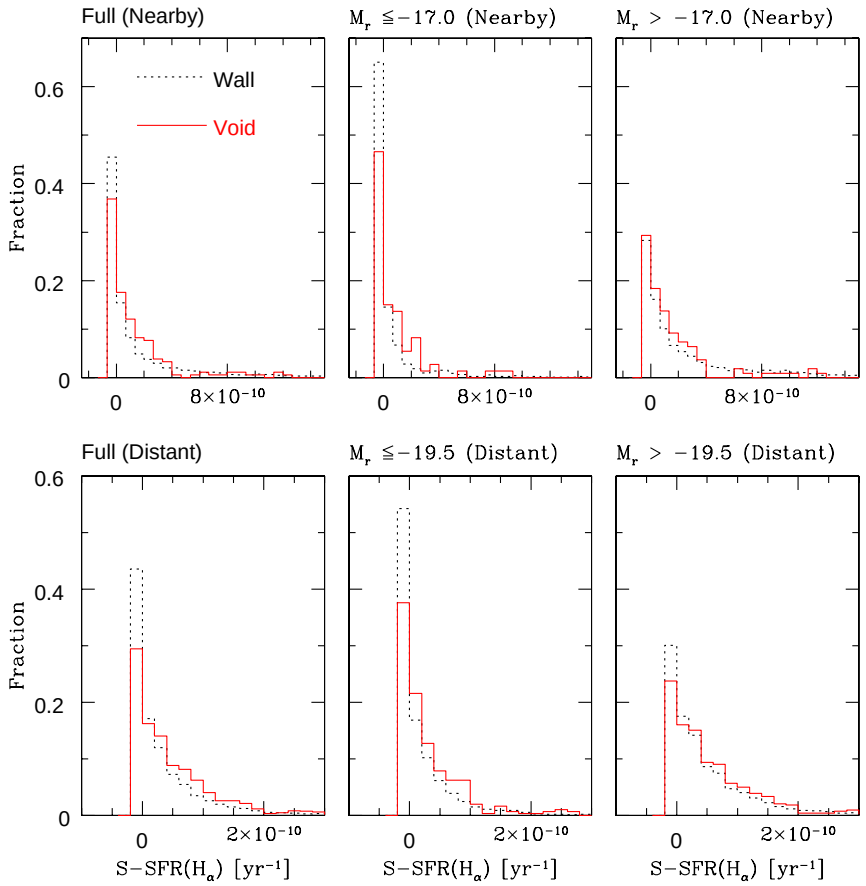

Figure 6.10: Distribution Hα specific star formation rates. We show the normalized fraction of void (solid lines) and wall galaxies (dotted lines) as a function of S-SFR(Hα). The top row shows the results for the nearby ($r < 72h^{-1}$Mpc) galaxies, the bottom row shows the results for the distant ($100 \leq r \leq 260h^{-1}$Mpc) galaxies. The first, second and third columns are the full, bright and faint samples. The fraction of galaxies per 10^{-10}yr^{-1} bin of S-SFR(Hα) is shown on the Y-axis. The KS statistic reveals that the distant void galaxy (bright, faint, and full) and respective wall galaxy samples are very different from one another, with a probability of $< 0.01\%$ that they are drawn from the same parent population. In the case of the nearby galaxies, only the bright galaxy distributions have a higher probability ($P \lesssim 0.027$) of being similar.

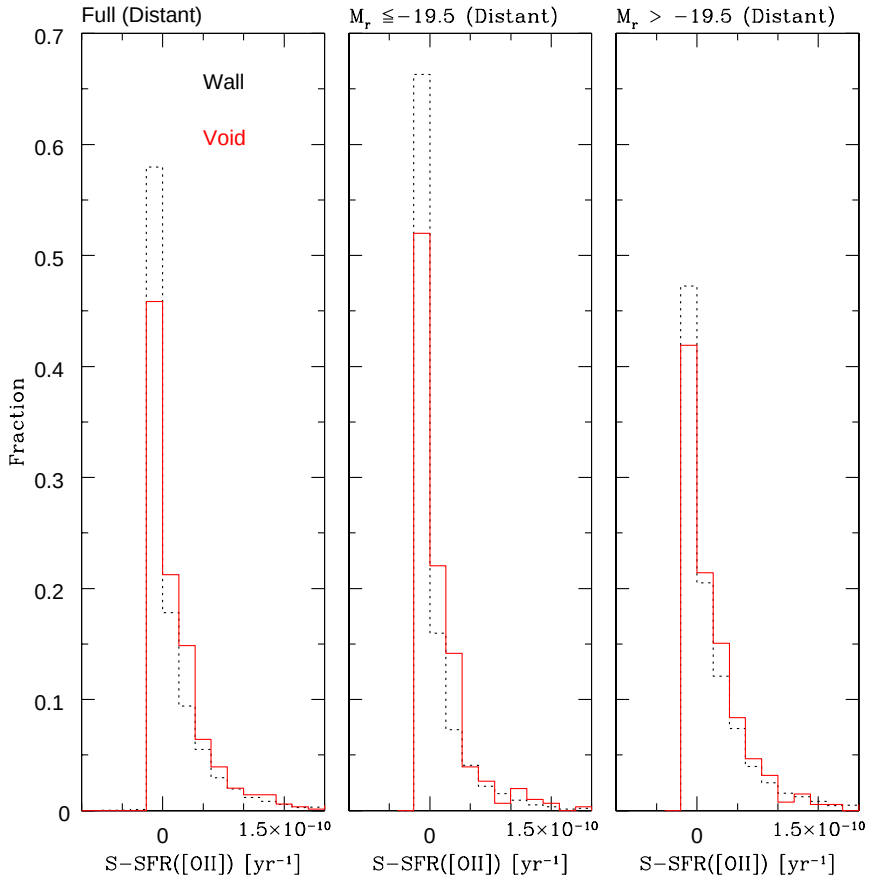

Figure 6.11: Distribution of [OII] specific star formation rates. We show the normalized fraction of void (solid lines) and wall galaxies (dotted lines) as a function of S-SFR([OII]). The first, second and third columns are the full, bright and faint distant samples. The fraction of galaxies per 10^{-10}yr^{-1}bin of SFR([OII]) is shown on the Y-axis. The KS statistic reveals that the distant void galaxy (bright, faint, and full) and respective wall galaxy samples are very different from one another, with a probability of $< 0.034\%$ that they are drawn from the same parent population.

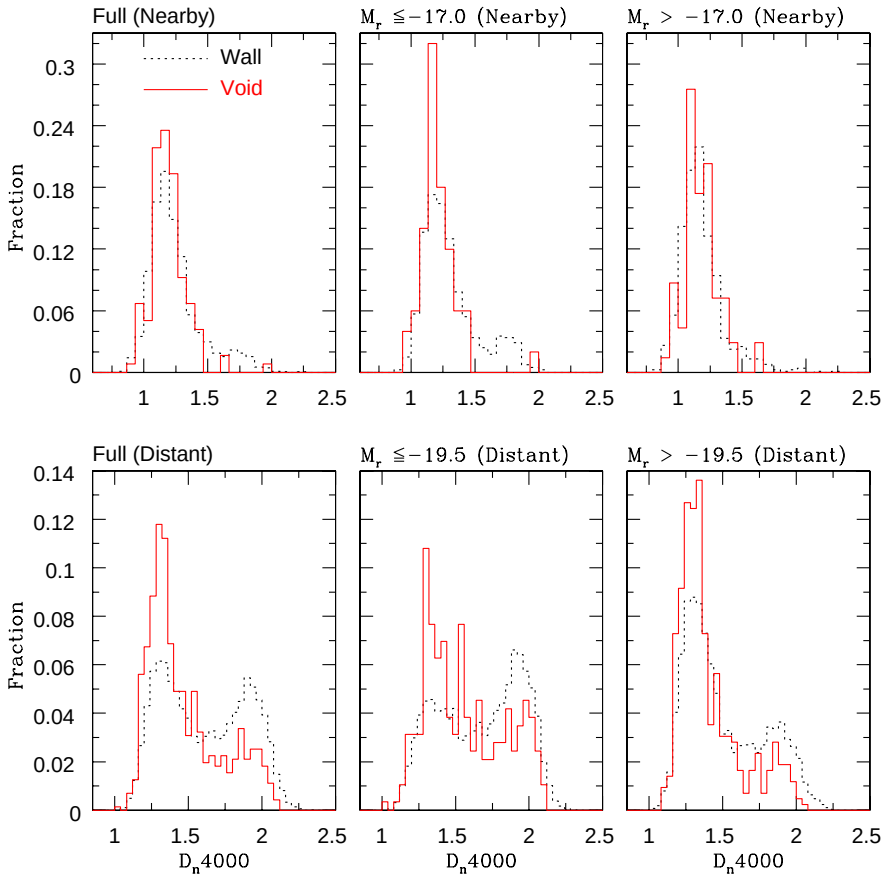

Figure 6.12: Distribution of the 4000 Å Balmer break. We show the normalized fraction of void (solid lines) and wall galaxies (dotted lines) as a function of D_n4000. The top row shows the results for the nearby ($r < 72h^{-1}$Mpc) galaxies, the bottom row shows the results for the distant ($100 \leq r \leq 260h^{-1}$Mpc) galaxies. The first, second and third columns are the full, bright and faint samples. The fraction of galaxies per 0.067 (nearby) and 0.04 (distant) bin of D_n4000 is shown on the Y-axis. The KS statistic reveals that the distant and nearby void galaxy (bright, faint, and full) and respective wall galaxy samples are very different from one another, with a probability of $< 0.01\%$ that they are drawn from the same parent population.

Chapter 7: Conclusions and Directions for Future Work

The large statistical significance of all the spectral diagnostics being considered and our results from the photometric properties (Rojas et al. 2003) reveal a genuine underlying difference between void and wall galaxies. Below we summarize our results from the photometric and spectroscopic analysis of void galaxies compared to wall galaxies as follows[1]

- Void galaxies are bluer and fainter than wall galaxies.
- Based on their Sersic and concentration indices as proxies for morphology, void galaxies are more late-type than wall galaxies.
- On average void galaxies have larger Hα, [OII], Hβ, [OIII], and [NII] equivalent widths than wall galaxies.
- The stellar masses and 4000 Å Balmer break of void galaxies are on average smaller than for wall galaxies.
- Void galaxies are less dusty than wall galaxies.

[1]Unless otherwise stated the results discussed also apply to the nearby samples and to comparisons between void and wall galaxies of similar luminosities and surface brightness profiles.

- The Hα and [OII] derived star formation rates of faint void galaxies are on average smaller than for wall galaxies. However, bright void galaxies have larger average SFRs than wall galaxies.

- Void galaxies have larger mean Hα *specific* star formation rates than wall galaxies. However, in the nearby sample only the bright void galaxies have larger S-SFR(Hα). The faint nearby (faintest of all galaxies examined) void galaxies do not have higher S-SFR(Hα).

- Analysis of the luminosity function of our void galaxies (Hoyle et al. 2003) shows that voids are not filled with a large population of dwarf galaxies.

- In Hao et al. (2004) we find that our void galaxies have on average similar metallicities to wall galaxies, that voids are dominated by emission-line galaxies, and that there is a deficiency of metal-poor galaxies in dense environments.

These observed properties of void galaxies can be explained in two possible scenarios. In the first case, hierarchical galaxy formation would suggest that void galaxies are old galaxies, formed when the voids were small and the matter in them more concentrated. Otherwise, as the voids expand and matter flows out towards the higher density regions, galaxies would never form inside the voids. Due to the lack of tidal interactions which can suppress the flow of gas to the center of the galaxy, void galaxies can continue to form stars over longer periods of time. This would explain the higher mean specific star formation rates observed in void galaxies. On the other hand, since low mass galaxies usually have young stellar ages and are more actively forming stars at the present than more massive galaxies, this would indicate that void

galaxies are actually younger systems as suggested by Grogin & Geller (1999, 2000) based on their bluer colors. We could test which scenario is correct by searching for void galaxies at larger redshifts (e.g., $z = 1$). If we fail to find void galaxies at large redshifts, then this would indicate that void galaxies are younger. If void galaxies are found at larger redshifts it will be interesting to see how their properties depend on redshift. Are the observed properties of void galaxies in the local universe comparable to those of void galaxies at an earlier epoch? How do observations at different redshifts compare to those across different wavebands? Answering these questions is critical to understanding galaxy formation.

The Great Observatories (Hubble Space Telescope, Chandra X-ray Observatory, Compton Gamma Ray Observatory, and Spitzer Space Telescope), GALEX ($z \sim 0 - 2$), DEEP2 ($z \sim 0.7 - 1.55$), the Magellan Project and VIRMOS-VLT Deep Survey ($z \sim 0 - 5$) will provide complementary observations that will help answer the questions posed above because they have the ability to probe galaxies at large redshifts with great sensitivity and unprecedented quality. For example, overlap between two of the DEEP2 Survey fields and the SDSS equatorial strip can allow one to piece together observations from the two surveys to construct a uniform snapshot of the universe down to a redshift of $z \sim 1.55$ and $I_{AB} = 23.5 - 24.5\,\mathrm{mag}$. In addition, DEEP2 has the advantage that the geometry of the survey and number of anticipated redshifts ($> 50,000$) lends itself to a nearest neighbor analysis for finding additional void galaxies. Likewise GALEX's Deep (DIS) and All-sky (AIS) Imaging Surveys along with the Medium (MSS) and Deep (DSS) Spectroscopic Surveys will allow the search for new void galaxies.

Equivalent width measurements are less affected by the large uncertainties that affect SFR calculations. Therefore, they are a more reliable spectral indicator of the underlying properties of the galaxies being compared. The fact that on average all five emission line EWs are larger for void than for wall galaxies is consistent with our results from the photometric properties. In the nearby samples the overall differences are not as significant, however, this can be partly explained by the smaller number of galaxies available in the samples.

To further understand the physical mechanisms that could explain the observed properties we will need to study void galaxies at multi-wavelengths. This can be done by cross-correlating the coordinates of our void galaxies with objects from deeper surveys such as SIRTF (3 to 180 microns in the near- and mid-infrared) and GALEX far UV (1350-1800 Å) and near UV (1800-3000 Å) that have common sky coverage with the SDSS footprint.

Observations from SIRTF (3 to 180 microns) in the near- and mid-infrared with IRAC and the far-infrared range with MIPS will contribute significantly to our understanding of galaxy and star formation. With these observation we will be able to test whether a substantial amount of mass is shrouded by dust and, therefore, evades detection in voids. With the detailed observations from SIRTF piercing through clouds and disks of dust, we can indirectly look for the signatures of hidden objects inside voids. Equally important will be observations from GALEX in the far UV (1350-1800 Å) and near UV (1800-3000 Å) bands. Recall that the SDSS covers the wavelength range from 3000-9000 Å, therefore, GALEX is an excellent complement to the SDSS. With more than 10^5 galaxies spanning a large redshift range from $z \sim 0 - 1$ in the

spectroscopic survey, we can address the question of what is the star formation and metal production history of galaxies out to redshift $z \sim 1$? Metal deficient stars are more common in underdense regions. However, if one compares metallicities of void galaxies against non-void galaxies, the differences are not that striking (Hao et al. 2003). A complement to this endeavor will be to look at low-metallicity galaxies in underdense environments to further understand the processes taking place inside these regions.

From our sample of void galaxies we found about 65 AGNs. Once the SDSS is completed, the sample of AGNs and possibly QSOs in voids will be large enough to study their properties in more detail. Their individual properties may be considerably different from AGNs and QSOs in less quiescent environments. The SWIRE Legacy program will image 100 deg^2 of the SDSS footprint with similar depth in the IR. The GALEX Deep Imaging Survey will provide comparable sensitivity ($m_{AB} \approx 26$) to that of the SDSS over a common sky coverage that will include $\sim 300,000$ QSOs. Complementary observations in the X-ray from the Chandra X-Ray Observatory will be extremely useful for looking at these AGN in more detail to help us understand the role environment plays on their formation and evolution.

The observed photometric and spectroscopic properties of void galaxies generally agree with predictions from semi-analytic models of structure formation (Benson et al. 2003) and scenarios where galaxy-galaxy interactions govern galaxy evolution. Benson et al. (2003) credit all the differences found between void and wall galaxies in their simulations to the differences in the smaller dark matter halos of the mass functions in voids.

Comparison of the properties of void galaxies to Bruzual & Charlot (1993, 2003) and similar stellar population evolution models can be used to study the history of star formation in void galaxies. As discussed in the beginning, hierarchical models of structure formation suggest that void galaxies have to be relatively old. However, the colors and surface brightness profiles of void galaxies are consistent with those of younger galaxies. Information regarding the star formation rates and histories is a key element in understanding the nature of mass build up in underdense environments.

At the present we can conclude that our findings show that void galaxies are different from galaxies elsewhere based on their photometric and spectroscopic properties. However, a physical mechanism that can explain their observed properties is still not well understood. With respect to other works, there is agreement in the sense that our void galaxies exhibit some properties suggested by studies of smaller samples of void galaxies like being blue and faint (Grogin & Geller 1999, 2000; Popescu et al. 1997, 1999; Pustilnik et al. 2002; Hopp et al. 1995). However, to some degree there is disagreement with other studies that fail to find noticeable differences between galaxies in low and high density environments (Hogg et al. 2004; Kauffmann et al. 2004; Balogh et al. 2003) because their analysis does not extend to such low density regions as ours. Overall however, we do have a consistent picture of how the properties of galaxies change with environment in agreement with previous studies (Kauffmann et al. 2004; Baldry et al. 2003; Brinchman et al. 2003; Balogh et al. 2003; Gomez et al. 2003; Lewis et al. 2002; Blanton et al. 2002; Hogg et al. 2002; Kodama et al. 2001; Strateva et al. 2001; Postman & Geller 1984; Dressler 1980). The observed trends are that in dense regions (like clusters of galaxies), galaxies typically have redder col-

ors, are brighter, their morphologies more closely resemble early-types, have reduced star formation rates, larger stellar masses, and, old stellar populations. In less dense environments galaxies are bluer, more late-type, have smaller stellar masses, higher ongoing star formation, are fainter, and, have young stellar populations. In this work we have extended the analysis of galaxy properties to extremely low density environments and demonstrated that void galaxies are different from other galaxies in more typical environments.

Funding for the creation and distribution of the SDSS Archive has been provided by the Alfred P. Sloan Foundation, the Participating Institutions, the National Aeronautics and Space Administration, the National Science Foundation, the U.S. Department of Energy, the Japanese Monbukagakusho, and the Max Planck Society. The SDSS Web site is http://www.sdss.org/.

The SDSS is managed by the Astrophysical Research Consortium (ARC) for the Participating Institutions. The Participating Institutions are The University of Chicago, Fermilab, the Institute for Advanced Study, the Japan Participation Group, The Johns Hopkins University, Los Alamos National Laboratory, the Max-Planck-Institute for Astronomy (MPIA), the Max-Planck-Institute for Astrophysics (MPA), New Mexico State University, University of Pittsburgh, Princeton University, the United States Naval Observatory, and the University of Washington. I acknowledge support from NSF grant AST-0071201 and a grant from the John Templeton Foundation.

Bibliography

[1] Abadi, M. G., Moore, B., & Bower, R. G. 1999, MNRAS, 308, 947

[2] Abazajian, K., et al. 2003, ApJ submitted, astro-ph/0305492

[3] Alonso, M. V., da Costa, L., Latham, D., Pellegrini, P. S., & Milone, A. E. 1994, AJ, 108, 1987

[4] Babul, A., & Postman, M. 1990, ApJ, 359, 280

[5] Baldry, I. K., et al. 2003, ApJ submitted, astro-ph/0309710

[6] Baldwin, J. A., Phillips, M. M., & Terlevich, R. 1981, PASP, 93, 5

[7] Balogh, M. L., Morris, S. L., Yee, H. K. C., Carlberg, R. G., & Ellingson, E. 1997, ApJL, 488, 75

[8] Balogh, M. L., Schade, D., Morris, S. L., Yee, H. K. C., Carlberg, R. G., & Ellingson, E. 1998, ApJL, 504, 75

[9] Balogh, M. L., Morris, S. L., Yee, H. K. C., Carlberg, R. G., & Ellingson, E. 1999, ApJ, 527, 54

[10] Balogh, M. L., Navarro, J. F., & Morris, S. L. 2000, ApJ, 540, 113

[11] Balogh, M. L., Couch, W. J., Smail, I., Bower, R. G., & Glazerbrook, K. 2002a, MNRAS submitted

[12] Balogh, M. L., et al. 2003, MNRAS submitted

[13] Baugh, C. M., Cole, S., & Frenk, C. S. 1996a, MNRAS, 283, 1361

[14] Baugh, C. M., Cole, S., & Frenk, C. S. 1996b, MNRAS, 282, L27

[15] Benson, A. J., Hoyle, F., Torres, F., & Vogeley, M. S. 2003, MNRAS, 340, 160

[16] Bennett, C. L., et al. 2003, ApJ submitted

[17] Bingelli, B., Tammann, G. A., & Sandage, A. 1987, AJ, 94, 251

[18] Bingelli, B. 1989, Large scale structure and motions in the universe; Proceedings of the International Meeting, Trieste, Italy, Apr. 6-9, 1988

[19] Blanton, M. R., Lin, H., Lupton, R. H., Maley, F. M., Young, N., Zehavi, I., & Loveday, J. 2003, AJ, 125, 2276

[20] Blanton, M. R., et al. 2001, ApJ, 121, 2358

[21] Blanton, M. R., et al. 2002, ApJ, 594, 186

[22] Blanton, M. R., et al. 2003, AJ, 125, 2348

[23] Bode, P., Ostriker J. P., Turok, N. 2000, ApJ, 556, 93

[24] Bremnes, T., Bingelli, B., & Prugniel, P. 1998, A&AS, 129, 313

[25] Broadhurst, T. J., Ellis, R. S.,& Glazerbrook, K. 1992 Nature, 355, 55

[26] Broadhurst, T. J., Ellis, R. S. & Shanks, T. 1988, MNRAS, 235, 827

[27] Bruzual, G. 1983, ApJ, 273, 105

[28] Byrd, G. & Valtonen, M. 1990, ApJ, 350, 89

[29] Caldwell, N., & Bothun, G. D. 1987, AJ, 94, 1126

[30] Cole, S., Lacey, C. G., Baugh, C. M., & Frenk, C. S. 2000, MNRAS, 319, 168

[31] Coles, P. & Lucchin, F. 2002 Cosmology, Second Edition (John Wiley & Sons)

[32] Colless, M., Ellis, R. S., Taylor, K.,& Hook, R. N. 1990, MNRAS, 244, 408

[33] Colless, M. et al. 2001, MNRAS, 328, 1039

[34] Couch, W. J. & Sharples, R. M. 1987, MNRAS, 229, 423

[35] Couch, W. J., Balogh, M. L., Bower, R. G., Smail, I., Glazerbrook, K., & Taylor, M. 2001, ApJ, 549, 820

[36] da Costa, L. N., et al. 1998, AJ, 116, 1

[37] da Costa, L. N., Vogeley, M .S., Geller, M. J., Huchra, J. P., & Changbom, P. 1994, ApJ, 437, 1

[38] Davis, M., Efstathiou, G., Frenk, C. S., & Wite, S. D. M. 1985, ApJ, 292, 371

[39] de Lapparent, V., Geller, M. J., & Huchra, J. P. 1991, ApJ, 369, 273

[40] Dekel, A., & Silk, J. 1986, ApJ, 303, 39

[41] Diaferio, A., Kauffmann, G., Balogh, M. L., White, S. D. M., Schade, D., & Ellingson, E. 2001, MNRAS, 323, 999

[42] Domínguez, M. J., Zandivarez, A. A., Martínez, H. J., Merchán, M. E., Muriel, H., & Lambas, D. G. 2002, MNRAS, 335, 825

[43] Dressler, A. 1980, ApJ, 236, 351

[44] Dressler, A., Thompson, I. B., & Shectman, S. 1985, ApJ, 288, 481

[45] Efstathiou, G., Ellis, R. S., & Peterson, B. S. 1988, MNRAS, 233, 431

[46] Eisenstein, D. J., et al. 2001, AJ, 122, 2267

[47] El-Ad, H., & Piran, T. 1997, ApJ, 491, 421

[48] El-Ad, H., Piran, T., & da Costa, L. N. 1996, ApJ, 462, 13

[49] El-Ad H., Piran, T., & da Costa, L. N. 1997, MNRAS, 287, 790

[50] Falco, E. E., et al. 1999, PASP, 111, 438

[51] Fitzpatrick, E. L 1998, ESA Conf. Ser. 413, 461, Ultraviolet Astrophysics Beyond the IUE Final Archive

[52] Fitzpatrick, E. L & Massa, D. 1999, ApJ, 525, 101

[53] Frenk, C. S., et al. 2000, astro-ph/0007362

[54] Fukugita, M., Shimasaku, K., Ichikawa, T. 1995, PASP, 107, 945

[55] Fukugita, M., Ichikawa, T., Gunn, J. E., Doi, M., Shimasaku, K., & Schneider, D. P. 1996, AJ, 111, 1748

[56] Gallagher, J. S., Hunter, D. A., Bushouse, H. 1989, AJ, 97, 700

[57] Goldberg, D. & Vogeley, M. S. 2003, ApJ accepted

[58] Gomez, P. L., et al. 2003, ApJ, 584, 210

[59] Gottlöber, S., Łokas, E. L., Klypin, A., & Hoffman, Y. 2003, MNRAS, 344, 715

[60] Grogin, N. A., & Geller, M. J. 1999, ApJ, 118, 2561

[61] Grogin, N. A., & Geller, M. J. 2000, ApJ, 119, 32

[62] Gunn, J. E., et al. 1998, ApJ, 116, 3040

[63] Gunn, J. E. & Gott, J. R. I. 1972, ApJ, 176, 1

[64] Geller, M. J., & Huchra, J. P. 1989, Science, 246, 857

[65] Hashimoto, Y., Oemler, A. J., Lin, H., & Tucker, D. L. 1998, ApJ, 499, 589

[66] Hao, L., Strauss, M. A., Rojas, R. R., & Vogeley, M. S. 2004 in preparation

[67] Heyl, J. S., Cole, S., Frenk, C. S., & Navarro, J. 1995, MNRAS, 274, 755

[68] Hoffman, Y., Silk, J., & Wyse, R. F. G. 1992, ApJ, 388, L13

[69] Hogg, D. W., Finkbeiner, D. P., Schlegel, D. J., & Gunn, J. E. 2001, AJ, 122, 2129

[70] Hogg, D. W., et al. 2002, ApJ, 124, 646

[71] Hogg, D. W., et al. 2003, ApJ, 202, 5103

[72] Hopkins, A. M., et al. 2003, ApJ, 599, 971

[73] Hoyle, F. & Vogeley, M. S. 2002, ApJ, 566, 641

[74] Hoyle, F., Rojas, R. R., Vogeley, M. S., & Brinkmann, J. 2003, ApJ submitted

[75] Hoyle, F. & Vogeley, M. S. 2003, ApJ submitted

[76] Hoyle, F. & Vogeley, M. S. 2004a, in preparation

[77] Hoyle, F. & Vogeley, M. S. 2004b, in preparation

[78] Hubble, E. 1929 Proc. Nat. Acc. Sci., 15, 168

[79] Huchra, J. P. 1977, ApJ, 217, 928

[80] Huchra, J. P., Geller, M. J., de Lapparent, V., & Corwin, H. 1990, ApJS, 72, 433

[81] Huchra, J. P., Geller, M. J., & Corwin, H. 1995, ApJS, 99, 391

[82] Huchra, J. P., Vogeley, M. S., & Geller, M. J. 1999, ApJS, 121, 287

[83] Icke, V. & van de Weygaert, R. 1987, AA, 184, 16

[84] James, P. A. 1994, MNRAS, 269, 176

[85] Jerjen, H., Binggeli, B., & Freeman, K. C. 2000, AJ, 119, 593

[86] Karachentsev, I. D., & Makarov, D. A. 1996, ApJ, 111, 794

[87] Kauffmann, G., White, S. D. M., & Guiderdoni, B. 1993, MNRAS, 264, 201

[88] Kauffmann, G. et al. 2003, MNRAS, 341, 33

[89] Kennicutt, R. C. 1983, ApJ, 272, 54

[90] Kennicutt, R. C. Jr. 1992, ApJ, 388, 310

[91] Kennicutt, R. C., Jr. 1998, ARA&A, 36, 189

[92] Kennicutt, R. C. & Kent, S. M., 1983, AJ, 88, 1094

[93] Kewley, L., Dopita, M., Sutherland, R., Heisler, C., Trevena, J. 2001, ApJ, 556, 121

[94] Kirshner, R. P., Oemler, A. Jr., Schechter, P. L., Shectman, S. A. 1981, ApJ, 248, 57

[95] Klypin, A., Kravtsov, A. V., Valenzuela, O., & Prada, F. 1999a, ApJ, 522, 82

[96] Kniazev, A. Y. et al. 2003, in preparation

[97] Koo, D. C. & Kron, R. G. 1992 ARA&A, 30, 613

[98] Kuhn, B., Hopp, U., & Elaässer, H. 1997, A&A, 318, 405

[99] Larson, R. B., Tinsley, B. M., & Caldwell, C. N. 1980, ApJ, 237, 692

[100] Lemaître, G. 1927, MNRAS, 91,483

[101] Lewis, I., et al. 2002, MNRAS, 334, 673

[102] Lanzetta, K. M., Bowen, D. V., Tytler, D., & Webb, J. K. 1995, ApJ, 442, 538

[103] Lupton, R. H., Gunn, J. E., Ivezić, Ž., Knapp, G. R., Kent, S., & Yasuda, N. 2001, in ASP Conf. Ser. 238, Astronomical Data Analysis Software and Systems X, ed. F. R. Harnden, Jr., F. A. Primini & H. E. Payne (San Francisco: ASP), 269

[104] Lupton, R. H., et al. 2002, SPIE, 4836, 350

[105] Mathis, H. & White S. D. M. 2002, MNRAS, 337, 1193

[106] Mihos, J. C., Hernquist, L. 1996, ApJ, 462, 576

[107] Miller, N. A. & Owen, F. N. 2002, AJ, 124, 2453

[108] McLin, K. M., Stocke, J. T., Weymann, R. J., Penton, S. V., Shull, J. M. 2002, ApJ, 574, 115

[109] Mo, H. J., McGaugh, S. S., & Bothun, G. D. 1994, MNRAS, 267, 129

[110] Moore, B., Ghinga, S., Governato, F., Lake, G., Quinn, T., Stadel, & J., Tozzi, P. 1999, ApJ, 524, L19

[111] Moore, B., Katz, N., Lake, G., Dressler, A., & Oemler, A. 1996, Nature, 379, 613

[112] Morris, A. L., Weymann, R. J., Dressler, A., McCarthy, P. J., Smith, B. A., Terrile, R. J., Giovanelli, R., & Irwin, M. 1993, ApJ, 419, 524

[113] Müller, V., Arbabi-Bidgoli, S., Einasto, J., Tucker, D. 2000, MNRAS, 318, 280

[114] Osterbrock, D. E. 1989, Astrophysics of Gaseous Nebulae and Active Galactic Nuclei (Mill Valley: University Science Books)

[115] Park, C., Vogeley, S. M., Geller, M. J., & Huchra, J. P. 1994, ApJ, 431, 569

[116] Peacock, J. 2000, Cosmological Physics (Cambridge University Press)

[117] Peebles, P. J. E. 2001, ApJ, 557, 495

[118] Peebles, P. J. E. 1993, Principles of Physical Cosmology (Princeton University Press)

[119] Pellegrini, P. S., da Costa, L. N., & de Carvalho, R. R. 1989, ApJ, 339, 595

[120] Pence, W. 1976, ApJ, 203, 39

[121] Peterson, B., Ellis, R. S., Efstathiou, G., Shanks, T., Bean, A. J., Fong, R., & Zen-Long, Z. 1986, MNRAS, 221, 233

[122] Petrosian, V. 1976, ApJ, 209, L1

[123] Pier, J. R., Munn, J. A., Hindsley, R. B., Hennessy, G. S., Kent, S. M., Lupton, R. H., & Ivezić, Ž. 2003, AJ, 125, 1559

[124] Plionis, M., & Basilakos, S. 2002, MNRAS, 330, 399

[125] Poggianti, B. M., Smail, I., Dressler, A., Couch, W. J., Barger, A. J., Butcher, H., Ellis, R. S., & Oemler, A. J. 1999, ApJ, 518, 576

[126] Popescu, C., Hopp, U., & Elaässer, H. 1997, A&A, 325, 881

[127] Postman, M., & Geller, M. J. 1984, ApJ, 281, 95

[128] Pustilnik, S. A., Martin, J. -M., Huchtmeier, W. K., Brosch, N., Lipovetsky, V. A., Richter, G. M. 2002, A&AS, 389, 405

[129] Quilis, V., Moore, B., & Bower, R. 2000, Science, 288, 1617

[130] Rojas, R. R., Vogeley, M. S., Hoyle, F. & Brinkmann, J., 2003, ApJ submitted

[131] Schlegel, D. J., Finkbeiner, D. P., & Davis, M. 1998, ApJ, 500, 525

[132] Sandage, A., & Binggeli, B. 1984, AJ, 89, 919

[133] Salpeter, E. E. 1955, ApJ, 121, 161

[134] Scranton, R. et al. 2002, ApJS, 579, 48

[135] Sersic J. L. 1968, Atlas de Galaxias Australes. Observatorio Astronómico, Cordoba.

[136] Shectman, S. A., et al. 1996, ApJ, 470, 172

[137] Shimasaku, K., et al. 2001, AJ, 122, 1238

[138] Solanes, J. M., Manrique, A., González-Casado , G., García-Gómez, C., Giovanelli, R., & Haynes, M. P. 2001, ApJ, 548, 97

[139] Sommerville, R. S. & Primack, J. R. 1999, MNRAS, 310, 1087

[140] Smith, J. A., et al. 2002, AJ, 123, 2121

[141] Starck, J. L., Siebenmorgen, R., & Gredel, R., ApJ, 482, 1011

[142] Staveley-Smith, L., Davies, R., & Kinman, T. D. 1992, MNRAS, 258, 334

[143] Stoughton, C. et al. 2002, AJ, 123, 485

[144] Strauss, M. A., et al. 2002, AJ, 124, 1810S

[145] Strateva, I., et al. 2001, ApJ, 122, 1874

[146] SubbaRao, M. 2004 in preperation

[147] Sung, E., Han C., Ryden, B. S., Chun, M., Kim, H. 1998, ApJ, 499, 140

[148] Tanaka, M. et al. 2003 in preparation

[149] Tegmark, M., Hamilton, A. J. S., & Xu, Y. 2002, MNRAS, 335, 887

[150] Tran, K. H., Simard, L., Zabludoff, A. I. & Mulchaey, J. S. 2001, ApJ, 549, 172

[151] Tresse, L., Maddox, S., Loveday, J., & Singleton, C. 1999, MNRAS, 310, 262

[152] Thuan, T. X., Gott, J. R. III, & Schneider, S. E. 1987, ApJ, 315, L93

[153] Vader, J.P., Vigroux, L., Lachieze-Rey, M., & Souviron, J. 1988, A&A, 203, 217

[154] Veilleux, S. & Osterbrock, D. E. 1987, ApjS, 63, 295

[155] Vennik, J., Hopp, U., Kovachev, B., Kuhn, B., & Elsässer, H. 1996, A&AS, 117, 261

[156] White, S. D. M. & Frenk, C. 1991, ApJ, 379, 52

[157] Yasuda, N. et al. 2001, AJ, 122, 110

[158] York, D. G. et al. 2000, AJ, 120, 1579

[159] Zabludoff, A. I. & Mulchaey, J. S. 1998, ApJ, 496, 39

[160] Zwicky, F., Herzog, E., & Wild, P. 1961, Catalogue of galaxies and clusters of galaxies, (Pasadena: California Institute of Technology) Vol. I

[161] Zwicky, F., & Herzog, E. 1962-1965, Catalogue of galaxies and clusters of galaxies, (Pasadena: California Institute of Technology) Vol. II-IV

[162] Zwicky, F., Karpowicz, M., & Kowal, C. 1965, Catalogue of galaxies and clusters of galaxies, (Pasadena: California Institute of Technology) Vol. V

[163] Zwicky, F., & Kowal, C. 1968, Catalogue of galaxies and clusters of galaxies, (Pasadena: California Institute of Technology) Vol. VI

Appendix A: Brief Review of Cosmology

A.1 Cosmology

Cosmology studies the behavior and large-scale structure of the universe with the aim of understanding the origin and evolution of cosmic structure. Observations have advanced the field of cosmology significantly thanks to the quality and quantity of data from galaxy surveys such as the Sloan Digital Sky Survey (York et al. 2000) and 2dF Redshift Galaxy Survey (Colless et al. 2001). When we observe the universe on large scales we immediately notice the presence of structures such as filaments and voids. A typical galaxy contains about 10^{11} stars, a cluster of galaxies about 10^3 galaxies, and a supercluster, which forms filaments and walls, about 10^4 galaxies. An interesting property of their distribution in space and time is that it appears to be highly uniform throughout the universe. This suggests that on large scales the universe is homogeneous and isotropic, i.e., looks the same at any given time and in every direction.

The cosmic microwave background radiation (CMBR) of the universe first observed by Penzias & Wilson (1965) provided evidence that universe expanded from a highly dense and hot small concentration of matter in what is known as the *Big*

Bang. More detailed observations from the Cosmic Background Explorer satellite (COBE; Mather et al. 1994) and recently by the Wilkinson Microwave Anisotropy Probe (WMAP; Bennett et al. 2003) suggest that the universe is geometrically flat, dominated by a cosmological constant[1] and radiating at a near black-body radiation tempertaure of 2.725 ± 0.002K (Bennett et al. 2003). Indpendent observations of Type Ia supernovae by Perlmutter et al. (1988) show that not only is the universe expanding but also accelerating. These properties of the universe based on compelling observations is what cosmologists attempt to explain by developing theoretical models that agree with observations.

A.1.1 Cosmological Principle

The fact that the universe appears to be homogeneous and isotropic on scales much larger than the average separation between galaxies is known as the *cosmological principle.* Much of the development of modern cosmology has been motivated by this principle in an attempt to construct a model(s) of the universe that is consistent with it. Such a model can be constructed within the framework of General Relativity. We can think of the universe as a continuous fluid in a four-dimensional (three spatial and one time-like coordinates) Riemannian space, where each fluid element is labeled by a general coordinate system $x^{\mu}(\mu = 0, 1, 2, 3)$. The temporal coordinate x^0 is the proper time measured by a clock moving with the fluid element. The remaining parameters are the three spatial coordinates $x^{\alpha}(\alpha = 1, 2, 3)$ known as the *comoving*

[1]The cosmological constant is discussed in detail in Section A.0.7 .

coordinates.

A homogeneous and isotropic space-time can be described by the Friedmann-Robertson-Walker (FRW) metric with line element:

$$ds^2 = g_{\mu\nu} dx^\mu dx^\nu \tag{A.1}$$

which in spherical coordinates (r, θ, ϕ) can be expressed as

$$ds^2 = c^2 dt^2 - R(t)^2 \left[\frac{dr^2}{1 - kr^2} + r^2 (d\theta^2 + \sin^2 \theta \, d\phi^2) \right] \tag{A.2}$$

The spatial coordinates (r, θ, ϕ) are called comoving coordinates and the time coordinate t, is the proper time measured by an observer with fixed comoving coordinates. In this case the mean rest frame of galaxies is in complete agreement with Eq. (A.2).

The constant k is the signature of space curvature, i.e.,

$$k = \begin{cases} 1, & \text{closed universe (Riemannian geometry)} \\ -1, & \text{open universe (Gauss} - \text{Lobachevski geometry),} \\ 0, & \text{flat universe (Euclidean geometry)} \end{cases} \tag{A.3}$$

$R(t) \equiv$ Scale factor [dimensions of length], where $R(t = t_o) = R_o$ at the present epoch, i.e. at $t = t_o$. Therefore, spatial separations at constant t are proportional to $R(t)$, and,

r = comoving radial distance coordinate and is constant with time for a given galaxy.

A.1.2 Horizons

An important question to ask is what portion of the universe is in causal contact at time t (i.e., the size of the *particle horizon*)? If we consider a light signal emitted at $r = 0$ at time $t = 0$ and integrate Eq. (A.2) for any radial path ($d\theta = d\phi = 0$) we can obtain the distance between 2 points ($d = \int_0^r ds$). Before doing so we must keep in mind that photons follow null geodesics $ds^2 = 0$, therefore, integrating up to a time t the light signal will reach a radial coordinate r_H given by:

$$\int_0^t \frac{c\,dt'}{R(t')} = \int_0^{r_H} \frac{dr}{\sqrt{1-kr^2}}. \tag{A.4}$$

A useful quantity to introduce is the *conformal time* $\eta(t)$ where,

$$\eta(t) \equiv \int_0^t \frac{c\,dt'}{R(t')} \tag{A.5}$$

Therefore the proper distance from $r = 0$ to $r = r_H$ is

$$d_H = R(t)\int_0^{r_H} \frac{dr}{\sqrt{1-kr^2}} = R(t)\int_0^t \frac{c\,dt'}{R(t')} \tag{A.6}$$

$$= \eta(t) - \eta(0) \tag{A.7}$$

If d_H is infinite at a given time, then all points in the universe are in causal contact. However, if d_H is finite, then there exists a causal horizon for an observer.

For a monotonically increasing $R(t)$, the behavior of $R(t)$ as $t \to 0$ determines whether horizons exist. For example, if $R(t) \propto t^n$ there is no horizon for $n \geq 1$.

At a fixed time t we can integrate an element of proper distance to obtain

$$d = R(t)r. \tag{A.8}$$

If we now take the derivative with respect to t of Eq. (A.8) and define the *recession speed* $v = \dot{d}$ we obtain:

$$v = \dot{R}(t)r = \frac{\dot{R}(t)}{R(t)}d, \quad \text{where} \quad r = d/R(t) \tag{A.9}$$

$$= Hd \tag{A.10}$$

Equation (A.10) is known as *Hubble's Law* (Hubble 1929), where H is the *Hubble parameter*. At the present $H(t = \text{now}) = H_o$ and can be expressed in terms of the dimensionless parameter h as $H_o = 100h\,\text{km s}^{-1}\,\text{Mpc}^{-1}$. The constant H_o is the *Hubble constant* and current observations from the WMAP satellite (Bennett et al. 2003) constrain h to $h = 0.71^{+0.04}_{-0.03}$.

The Hubble time ($t_H = 2/3H_o$) and distance ($d_H = c/H_o$) can easily be evaluated to constrain the age of the universe and particle horizon. In terms of h the respective values are: $t_H = 9.78h^{-1}\,\text{yr}$ and $d_H = 3000h^{-1}\,\text{Mpc}$, where 1 parsec (pc) equals 3.26 light years (ly). We can also make the scale factor dimensionless by redefining it as $a(t) = R(t)/R_o$ where $R(t = \text{now}) = R_o$ and therefore $a(t = \text{now}) = 1$.

A.1.3 Redshift

Consider an electromagnetic wave crest emitted from a luminous source at $r = r_{em}$ at time $t = t_{em}$ that arrives at a detector at $r = 0$ at time $t = t_{obs}$. Since radiation travels along null geodesics ($ds^2 = 0$) then

$$\int_{t_{em}}^{t_{obs}} \frac{c\,dt}{a(t)} = \int_0^{r_{em}} \frac{dr}{\sqrt{1-kr^2}}. \tag{A.11}$$

The next wave crest emitted at time $t_{em} + \delta t_{em}$ arrives at the detector at time $t_{obs} + \delta t_{obs}$, therefore,

$$\int_{t_{em}+\delta t_{em}}^{t_{obs}+\delta t_{obs}} \frac{c\,dt}{a(t)} = \int_0^{r_{em}} \frac{dr}{\sqrt{1-kr^2}} \tag{A.12}$$

$$= \int_{t_{em}}^{t_{obs}} \frac{c\,dt}{a(t)} \tag{A.13}$$

$$\Longrightarrow \int_{t_{obs}}^{t_{obs}+\delta t_{obs}} \frac{dt}{a(t)} = \int_{t_{em}}^{t_{em}+\delta t_{em}} \frac{dt}{a(t)}. \tag{A.14}$$

If δt_{em} and δt_{obs} are small then $a(t)$ ~constant and

$$\frac{\delta t_{obs}}{a(t_{obs})} = \frac{\delta t_{em}}{a(t_{em})}. \tag{A.15}$$

Since $\delta t_{obs} = 1/\nu_{obs}$ and $\delta t_{em} = 1/\nu_{em}$ (ν_{obs} and ν_{em} are the observed and emitted frequencies respectively) then,

$$\nu_{em} a(t_{em}) = \nu_{obs} a(t_{obs}) \tag{A.16}$$

$$\Longrightarrow \frac{\lambda_{obs}}{\lambda_{em}} = \frac{a(t_{obs})}{a(t_{em})} \equiv 1 + z, \tag{A.17}$$

where the *redshift* z of the luminous source is defined as

$$z = \frac{\lambda_{obs} - \lambda_{em}}{\lambda_{em}}, \quad \text{where} \quad -1 < z < \infty \tag{A.18}$$

and is therefore, a measure of the shift of spectral lines. This implies that the wavelength of light from e.g., a distant galaxy redshifts by an amount proportional to the expansion factor during propagation. As an interesting consequence, consider the energy of a photon moving freely in space $E = \hbar/\lambda \propto a^{-1}$ (Planck's constant $\hbar = 1.05 \times 10^{-34}\,\mathrm{J\,s}$). In the case of massive particles the same relation holds $|\vec{p}| \propto a(t)^{-1}$ (where $\vec{p}$ is the relativistic momentum). As $a(t)$ increases $|\vec{p}|$ decreases. Therefore, a particle in motion will eventually come to rest, i.e., objects moving freely approach the comoving frame.

A.1.4 Cosmological Distance Measures

Consider an observer at $r = 0$ and an object at comoving coordinate r. The object is observed at time t_o. Thus far in the previous sections we have introduced the:

- Coordinate distance r which is not physical because as light travels $a(t_o)$ changes and there is therefore no way of measuring it.
- Proper or comoving distance at t_o, $d = c\,a(t_o)\int_0^r \frac{dr'}{\sqrt{1-kr'^2}}$ which is not measurable since we can not travel with a beam of light. This distance is used for making

large-scale structure maps, because it preserves sizes and shapes of structures that are fixed in comoving coordinates.

A measurable distance is the *Luminosity Distance* d_L. Let L be the absolute luminosity (energy/time) emitted by a source at point P with coordinate distance r at time t and let F denote the flux (energy/time/area) received by an observer at P_o at time t_o. The luminosity distance is then defined as

$$d_L = \left(\frac{L}{4\pi F}\right)^{1/2} = R_o S_k(r)(1+z) \tag{A.19}$$

by conservation of energy, where

$$S_k(r) = \begin{cases} \sin r & (k=1) \\ \sinh r & (k=-1) \\ r & (k=0) \end{cases} . \tag{A.20}$$

Note that the total area over which the energy is spread is $4\pi(ra(t_o))^2$, and the flux is reduced by two factors of $1+z$: one from the energy of photons being reduced (redshifted) and one from *time dilation*[2]. If the luminosity of the emitting source is known (e.g., from standard candles like Type Ia supernovae) we can then measure d_L.

Another useful distance measure is the *Angular Diameter Distance* d_A which relates the physical size (D) of a standard rod to the angle (δ) it subtends

---

[2]From Eq. (A.16) and Eq. (A.17) we can see that events on distant galaxies time-dilate, in accordance with the expansion of the universe.

$$d_A \equiv \frac{D}{\delta} = \frac{R_o S_k(r)}{1+z} = \frac{d_L}{(1+z)^2}. \tag{A.21}$$

The angular diameter distance sets the angular scale of sizes of galaxies, the cosmic microwave background (CMB), strong gravitational lensing, etc. For a static Euclidean geometry in the limit $z << 1$ we recover the familiar relation $d = d_L = d_A$.

A.1.5 The $m - z$ Relation

The *apparent magnitude* (m) of a galaxy or star provides information on how bright the source appears as seen from Earth and is a measure the respective apparent flux. The scale used is a logarithmic scale such that the smaller the magnitude the brighter the source. In this scale a 1 magnitude difference corresponds to a factor of 2.512. The absolute magnitude (M) is related to the absolute luminosity of an object and is defined as the apparent magnitude an object would have if it were placed at a distance of 10pc from the Sun. The luminosity distance of a source is related to its apparent and absolute magnitudes by

$$m - M = 5 \log_{10} \left(\frac{d_L}{10pc} \right) + K(z). \tag{A.22}$$

When we observe light from a distant galaxy what we measure is its flux within a fixed bandpass. However, this galaxy is emitting light in a different band than that in which we are observing. Therefore, we need to apply a correction to the flux $K(z)$ known as the *K-correction*. For example, in the case of very red and distant galaxies the K-correction is large and positive. The quantity $m - M$ is the *distance modulus*.

In this thesis all magnitudes are K-corrected as discussed in Chapter 5.

A.1.6 Dynamics of the Expansion

Given a FRW metric and an undetermined scale factor $a(t)$ we would like to know the time evolution of $a(t)$ as determined by the energy content of the Universe. This can be accomplished within the framework of general relativity where the relation between the geometry of space-time and matter content of the universe are linked via the *Einstein Field equations*. For the case of zero cosmological constant ($\Lambda = 0$)[3] they are given by

$$R_{\mu\nu} - \frac{1}{2} g_{\mu\nu} R = \frac{8\pi G}{c^4} T^{\mu\nu}. \tag{A.23}$$

$R_{\mu\nu}$ is the Ricci tensor, $R = g^{\mu\nu} R_{\mu\nu}$ the Ricci scalar, G Newton's gravitational constant ($G = 6.67 \times 10^{-11} \mathrm{m}^3\,\mathrm{kg}^{-1}\,\mathrm{s}^{-2}$) and c the speed of light. The metric tensor $g_{\mu\nu}$ contains all the information about the gravitational field. The energy-momentum tensor $T^{\mu\nu}$ is diagonal in a comoving coordinate system and the respective space components are all equal by isotropy, therefore,

$$T^{\mu}{}_{\nu} = \begin{pmatrix} \rho(t) & 0 & 0 & 0 \\ 0 & -p(t) & 0 & 0 \\ 0 & 0 & -p(t) & 0 \\ 0 & 0 & 0 & -p(t) \end{pmatrix} \tag{A.24}$$

[3] The case $\Lambda \neq 0$ will be discussed later.

Where $\rho(t)$ and $p(t)$ are arbitrary positive functions of time, corresponding to the energy density and pressure respectively.

We can separate the time ($\mu = 0, \nu = 0$) and space ($\mu = i, \nu = i,\ i = 1, 2, 3$) components of the Einstein field equations to obtain,

$$\dot{a}^2 - \frac{8\pi G}{3} a^2 \rho = kc^2 \tag{A.25}$$

and

$$2a\ddot{a} + \dot{a}^2 + kc^2 = -\frac{8\pi G}{c^2} p a^2. \tag{A.26}$$

If we consider conservation of the energy-momentum tensor $\nabla^\nu T_{\mu\nu} = 0$ we get

$$d(\rho c^2 a^3) = -p d(a^3) \tag{A.27}$$

$$\Longrightarrow \dot{\rho} = -3\left(\rho + \frac{p}{c^2}\right)\frac{\dot{a}}{a} \tag{A.28}$$

Equations (A.25), (A.26), and (A.28) are know as the *Friedmann Equations*, of the three equations only two are independent. We can assume an equation of state of the form $p = w\rho c^2$ with constant w. Special cases for the choice of w are:

$$w = \begin{cases} 1/3, & \text{radiation} \\ 0, & \text{pressureless matter} \\ -1, & \text{vacuum} \end{cases} \tag{A.29}$$

Integrating Eq. (A.28) using the values for w in Eq. (A.29) yields,

$$\rho \propto a(t)^{-3(1+w)} = \begin{cases} a^{-4}, & \text{radiation} \\ a^{3}, & \text{pressureless matter} \\ \text{constant}, & \text{vacuum} \end{cases} \tag{A.30}$$

An important case to consider in Eq. (A.25) is that of a Euclidean geometry ($k = 0$) which reduces to $\dot{a}^2 = \frac{8\pi G}{3} a^2 \rho$. Recall from Eq. (A.9) that $H = \dot{a}/a$, therefore, we define the *critical density* ρ_c (for $\Lambda = 0$) as,

$$\rho_c = \frac{3H^2}{8\pi G} \tag{A.31}$$

such that if

- $\rho > \rho_c$ the universe is spatially closed, bounded and destined to recollapse
- $\rho < \rho_c$ the universe is spatially open, unbound and destined to expand forever
- $\rho = \rho_c$ the universe is spatially flat

Therefore ρ_c is the density required to make the universe flat. The three cases described above are also referred to as the *Friedmann Models*.

We can introduce the *Density parameter*

$$\Omega \equiv \frac{3H^2\rho}{8\pi G} = \rho/\rho_c \tag{A.32}$$

where ρ is the total density i.e., it includes contributions from matter, radiation and

vacuum. Similarly for the various components of Ω we can define $\Omega_i = \rho_i/\rho_c$, where the subscript i denotes matter(1), radiation(2), and vacuum(3). Using the density parameters Ω_i the Friedmann equation (A.25) can be expressed as

$$\rho = \frac{3H_o^2}{8\pi G}(\Omega_v + \Omega_m a^{-3} + \Omega_r a^{-4}) \tag{A.33}$$

In terms of k Eq. (A.33) is

$$\frac{kc^2}{H^2R^2} = (\Omega_v(a) + \Omega_m(a) + \Omega_r(a) - 1) \tag{A.34}$$

Note that for the case of a flat (k=0) universe, $\sum_i \Omega_i = 1$.

A parameter commonly encountered in cosmology is the *deceleration parameter* q given by

$$q_o \equiv -\frac{\ddot{a}_o}{a}\frac{1}{H_o^2} = \frac{1}{2}\Omega_o(1 + 3w) \tag{A.35}$$

where $\Omega_o = \Omega|_{\text{today}}$.

In terms of q_o we can express respectively the d_L, d_A and Hubble law as

$$d_L = \frac{c}{H_o}[z + \frac{1}{2}(1 - q_o)z^2 + ...] \tag{A.36}$$

$$d_A = \frac{c}{H_o}[z - \frac{1}{2}(3 + q_o)z^2 + ...] \tag{A.37}$$

$$t_o - t = \frac{1}{H_o}[z - (1 + \frac{1}{2}q_o)z^2 + ...] \tag{A.38}$$

demonstrating that all distance measures give the same linear relation at low z. Since

$$R_o = \frac{c}{H_o}\left[\frac{\Omega - 1}{k}\right]^{-1/2} \tag{A.39}$$

then Eq. (A.33) can be expressed as

$$H^2(a) = H_o^2[\Omega_v + \Omega_m a^{-3} + \Omega_r a^{-4} - (\Omega - 1)a^{-2}] \tag{A.40}$$

and since $R\,dr = c\,dt$ and $R_o/R = 1+z$, we can finally define the *Comoving Distance-Redshift* equation

$$R_o dr = \frac{c}{H_o}[(1-\Omega)(1+z^2) + \Omega_v + \Omega_m(1+z)^3 + \Omega_r(1+z)^4]^{-1/2}dz. \tag{A.41}$$

For a given cosmology (choice of Ω_i and H_o) Eq. (A.41) is the equation we use for converting redshifts of galaxies into a distance in physical units, where $R_o dr$ is the increment of comoving distance.

A.1.7 The Cosmological Constant, $\Lambda \neq 0$

In Einstein's original formulation of general relativity a static universe is not possible unless the energy-density or pressure are negative. At that time (1916) a universe in a dynamic state was not favored by theory nor observations. Therefore, to reconcile his field equations with a static universe, he introduced the cosmological constant term Λ:

$$R_{\mu\nu} - \frac{1}{2}g_{\mu\nu}R - \Lambda g_{\mu\nu} = \frac{8\pi G}{c^4}T_{\mu\nu} \tag{A.42}$$

where Λ has units of $[L^{-2}]$. If we define the *modified* energy-momentum tensor $T'_{\mu\nu}$ as

$$T'_{\mu\nu} = T_{\mu\nu} + \frac{\Lambda c^4}{8\pi G}g_{\mu\nu} \tag{A.43}$$

and introduce the effective p' pressure and effective density ρ' such that

$$p' = p - \frac{\Lambda c^4}{8\pi G} \tag{A.44}$$

and

$$\rho' = \rho + \frac{\Lambda c^2}{8\pi G} \tag{A.45}$$

then we can follow steps similar to those used in deriving the Friedmann equations (A.25) and (A.26) to obtain the modified versions as

$$\dot{a}^2 - \frac{8\pi G}{3}a^2\rho' = kc^2 \tag{A.46}$$

and

$$\ddot{a} = -\frac{4\pi G}{3}\left(\rho' + 3\frac{p'}{c^2}\right)a. \tag{A.47}$$

Clearly static but unstable solutions are possible if

$$\rho' = -3\frac{p'}{c^2} = \frac{3kc^2}{8\pi G a^2}. \tag{A.48}$$

Two cases worth considering are:

1. The *de Sitter* model. An empty ($p = 0, \rho = 0$) and flat ($k = 0$) universe. In this case integrating Eq. (A.46) yields $a \propto \exp[(\Lambda/3)^{1/2} tc]$. This implies that there is no singularity in the past i.e., $a \neq 0 \ \forall t$.

2. The *Lemaître* model (Lemaître 1927). A positively curved universe ($k = 1$). In this case $a(t = 0) = 0$ and at first a increases as $a \propto t^{2/3}$, the expansion begins to slow down reaching a *coasting period* after which the expansion then speeds up and eventually follows the de Sitter model.

In general, the effect of introducing a positive cosmological constant in the field equations is that it behaves as a repulsive force that balances the attractive force from matter. As the universe expands however, the attractive force weakens and the repulsive force from the cosmological constant term dominates, eventually leading to the de Sitter behavior. Therefore, the Friedmann models discussed earlier are no longer valid in a cosmology with $\Lambda > 0$, i.e., the simple relations between density, fate, and geometry of spacetime are broken. In the case of *anti-de-Sitter* space ($\Lambda < 0$) we can recover the properties of the $k = 0, \pm 1$ models, however, observations currently do not favor $\Lambda < 0$ cosmologies.

The most up to date values of Ω, Ω_m, Ω_Λ, and h obtained from WMAP Observations (Bennett et al. 2003) are

- $\Omega = 1.02^{+0.02}_{-0.02}$
- $\Omega_m = 0.27^{+0.04}_{-0.04}$

- $\Omega_\Lambda = 0.73^{+0.04}_{-0.04}$
- $h = 0.71^{+0.04}_{-0.03}$

In this thesis we adopt an $(\Omega_\Lambda, \Omega_m) = (0.7, 0.3)$ cosmology with $h \equiv H_o/100\text{km s}^{-1}\,\text{Mpc}^{-1}$ when converting redshifts into comoving distances. For a more detailed discussion on cosmology and the formulas described above, excellent references are Peebles (1993), Peacock (2000), and Coles & Lucchin (2002).

Appendix B: Complete List of Photometric and Spectroscopic Properties

As discussed in previous chapters, the properties of void and wall galaxies of similar luminosities and morphological type (as defined by their Sersic index) are compared. Here we present a summary of results for the distant and nearby samples for all the sub-samples being considered. The distant samples are split into 4 sub-samples: bright ($M_r \leq -19.5$), faint ($M_r > -19.5$), late ($n < 1.8$), and early ($n > 1.8$). The nearby samples are also split into 4 sub-samples but using a different absolute magnitude cut, therefore, we have: bright ($M_r \leq -17.0$), faint ($M_r > -17.0$), late ($n < 1.8$), and early ($n > 1.8$).

In Tables B.1 and B.2 we present photometric results for the nearby and distant samples respectively. The number of galaxies (void and wall) in each sample and sub-sample are listed next to the magnitude range heading as [N_V (void), N_W (wall)]. We can see that based on color ($g-r$, $u-g$, and $u-r$) and morphology (Sersic and concentration index) void galaxies (nearby and distant) are on average bluer and more disk-like than wall galaxies of similar luminosities and morphology. For the nearby and distant case the mean statistical significance of the differences is $\sim 2\sigma_\mu$ and $> 5\sigma_\mu$ respectively.

The spectroscopic results for the same samples and sub-samples discussed above are given in Tables B.3 and B.4 for the nearby and distant samples respectively. In this case void galaxies have larger mean emission line equivalent widths, specific star formation rates, smaller stellar masses and smaller 4000 Å Balmer strength than wall galaxies of similar intrinsic brightness and morphology. Once again we find that the mean statistical significance of the differences is about $2\sigma_\mu$ and more than $5\sigma_\mu$ for the nearby and distant samples respectively.

LIST OF PHOTOMETRIC PROPERTIES FOR THE NEARBY SAMPLE

Table B.1: Means, errors on the means and KS test probabilities that the void and wall galaxies are drawn from the same parent population for the photometric properties of void and wall galaxies in the nearby sample ($r < 72h^{-1}$Mpc). The number of galaxies (void and wall) in each sample and sub-sample are listed next to the magnitude range heading as [N_V (void), N_W (wall)]. Small values of P correspond to a low probability that the two samples are drawn from the same parent population. The KS test shows that void galaxies appear to have different colors to wall galaxies. The void galaxies appear bluer than the respective wall galaxies in all cases, where the average difference between the means of the colors is about $2\sigma_\mu$. However, the concentration and Sersic indices are not significantly different.

Full ($-19.9 \leq M_r \leq -14.5$)	[$N_V = 194$, $N_W = 2256$]			
Property	Void (VGD) $\mu \pm \sigma_\mu$	Wall (WGD) $\mu \pm \sigma_\mu$	KS (P) Probability	[N_V, N_W]
$g-r$	0.433 ± 0.014	0.490 ± 0.004	0.002	(194, 2225)
$u-g$	1.193 ± 0.035	1.289 ± 0.011	0.007	(191, 2200)
$u-r$	1.598 ± 0.040	1.764 ± 0.013	0.001	(190, 2176)
$r90/r50$	2.390 ± 0.024	2.390 ± 0.007	0.802	(194, 2256)
n	1.388 ± 0.034	1.456 ± 0.004	0.506	(194, 2256)
Bright ($M_r \leq -17.0$)	[$N_V = 76$, $N_W = 1071$]			
Property	Void (VGD_b) $\mu \pm \sigma_\mu$	Wall (WGD_b) $\mu \pm \sigma_\mu$	KS (P) Probability	[N_V, N_W]
$g-r$	0.510 ± 0.019	0.549 ± 0.006	0.207	(76, 1062)
$u-g$	1.303 ± 0.050	1.395 ± 0.016	0.392	(75, 1046)
$u-r$	1.810 ± 0.063	1.930 ± 0.019	0.104	(75, 1041)
$r90/r50$	2.429 ± 0.044	2.421 ± 0.011	0.424	(76, 1071)
n	1.518 ± 0.060	1.626 ± 0.004	0.605	(76, 1071)
Faint ($M_r > -17.0$)	[$N_V = 118$, $N_W = 1185$]			
Property	Void (VGD_f) $\mu \pm \sigma_\mu$	Wall (WGD_f) $\mu \pm \sigma_\mu$	KS (P) Probability	[N_V, N_W]
$g-r$	0.383 ± 0.018	0.436 ± 0.006	0.003	(118, 1163)
$u-g$	1.121 ± 0.046	1.193 ± 0.015	0.074	(116, 1154)
$u-r$	1.459 ± 0.047	1.611 ± 0.016	0.018	(115, 1135)
$r90/r50$	2.366 ± 0.027	2.361 ± 0.008	0.918	(118, 1185)
n	1.305 ± 0.039	1.304 ± 0.006	0.509	(118, 1185)
Late ($n < 1.8$)	[$N_V = 167$, $N_W = 1817$]			
Property	Void (VGD_l) $\mu \pm \sigma_\mu$	Wall (WGD_l) $\mu \pm \sigma_\mu$	KS (P) Probability	[N_V, N_W]
$g-r$	0.419 ± 0.015	0.456 ± 0.004	0.046	(167, 1791)
$u-g$	1.178 ± 0.038	1.245 ± 0.012	0.032	(164, 1766)
$u-r$	1.564 ± 0.041	1.687 ± 0.013	0.014	(163, 1748)
$r90/r50$	2.329 ± 0.023	2.306 ± 0.006	0.566	(167, 1817)
n	1.240 ± 0.021	1.211 ± 0.002	0.149	(167, 1817)
Early ($n > 1.8$)	[$N_V = 27$, $N_W = 439$]			
Property	Void (VGD_e) $\mu \pm \sigma_\mu$	Wall (WGD_e) $\mu \pm \sigma_\mu$	KS (P) Probability	[N_V, N_W]
$g-r$	0.521 ± 0.041	0.628 ± 0.011	0.006	(27, 439)
$u-g$	1.279 ± 0.086	1.147 ± 0.025	0.021	(27, 434)
$u-r$	1.801 ± 0.122	2.077 ± 0.032	0.005	(27, 428)
$r90/r50$	2.769 ± 0.056	2.735 ± 0.019	0.602	(27, 439)
n	2.304 ± 0.079	2.471 ± 0.010	0.465	(27, 439)

LIST OF PHOTOMETRIC PROPERTIES FOR THE DISTANT SAMPLE

Table B.2: Means, errors on the means and KS test probabilities that the void and wall galaxies are drawn from the same parent population for the photometric properties of void and wall galaxies in the distant sample ($100 \leq r \leq 260h^{-1}$Mpc). The number of galaxies (void and wall) in each sample and sub-sample are listed next to the magnitude range heading as [N_V (void), N_W (wall)]. Small values of P correspond to a low probability that the two samples are drawn from the same parent population. In this case, the KS test shows that the void and wall galaxies are drawn from different populations based on both color and morphology (concentration index and surface brightness profile). The differences between the means of the different parameters measured are on average $> 5\sigma_\mu$, except for the concentration index in the faint and late sub-samples, where the difference is $\sim 2\sigma_\mu$. Void galaxies are on average bluer and more disklike than wall galaxies.

Full ($-22.5 \leq M_r \leq -17.77$) [$N_V = 1010, N_W = 12732$]

Property	Void (VGD) $\mu \pm \sigma_\mu$	Wall (WGD) $\mu \pm \sigma_\mu$	KS (P) Probability	[N_V, N_W]
$g-r$	0.615 ± 0.007	0.719 ± 0.002	$< 10^{-4}$	(1005, 12714)
$u-g$	1.359 ± 0.014	1.509 ± 0.004	$< 10^{-4}$	(1002, 12594)
$u-r$	1.958 ± 0.018	2.219 ± 0.005	$< 10^{-4}$	(997, 12541)
$r90/r50$	2.449 ± 0.011	2.571 ± 0.004	$< 10^{-4}$	(1010, 12732)
n	1.718 ± 0.024	2.051 ± 0.002	$< 10^{-4}$	(1010, 12732)

Bright ($M_r \leq -19.5$) [$N_V = 409$, $N_W = 7831$]

Property	Void (VGD_b) $\mu \pm \sigma_\mu$	Wall (WGD_b) $\mu \pm \sigma_\mu$	KS (P) Probability	[N_V, N_W]
$g-r$	0.686 ± 0.009	0.765 ± 0.002	$< 10^{-4}$	(409, 7825)
$u-g$	1.457 ± 0.021	1.589 ± 0.005	$< 10^{-4}$	(407, 7767)
$u-r$	2.126 ± 0.026	2.343 ± 0.006	$< 10^{-4}$	(404, 7724)
$r90/r50$	2.505 ± 0.019	2.656 ± 0.004	$< 10^{-4}$	(409, 7831)
n	1.908 ± 0.042	2.285 ± 0.003	$< 10^{-4}$	(409, 7831)

Faint ($M_r > -19.5$) [$N_V = 601$, $N_W = 4901$]

Property	Void (VGD_f) $\mu \pm \sigma_\mu$	Wall (WGD_f) $\mu \pm \sigma_\mu$	KS (P) Probability	[N_V, N_W]
$g-r$	0.567 ± 0.009	0.645 ± 0.003	$< 10^{-4}$	(601, 4889)
$u-g$	1.292 ± 0.019	1.381 ± 0.007	$< 10^{-4}$	(595, 4827)
$u-r$	1.844 ± 0.024	2.020 ± 0.009	$< 10^{-4}$	(593, 4817)
$r90/r50$	2.411 ± 0.013	2.435 ± 0.005	0.211	(601, 4901)
n	1.589 ± 0.028	1.677 ± 0.003	$< 10^{-4}$	(601, 4901)

Late ($n < 1.8$) [$N_V = 659$, $N_W = 6037$]

Property	Void (VGD_l) $\mu \pm \sigma_\mu$	Wall (WGD_l) $\mu \pm \sigma_\mu$	KS (P) Probability	[N_V, N_W]
$g-r$	0.530 ± 0.007	0.584 ± 0.002	$< 10^{-4}$	(659, 6023)
$u-g$	1.232 ± 0.016	1.286 ± 0.005	$< 10^{-4}$	(655, 5965)
$u-r$	1.747 ± 0.019	1.863 ± 0.007	$< 10^{-4}$	(652, 5951)
$r90/r50$	2.274 ± 0.009	2.275 ± 0.003	0.293	(659, 6037)
n	1.266 ± 0.010	1.287 ± 0.001	0.109	(659, 6037)

Early ($n > 1.8$) [$N_V = 351$, $N_W = 6695$]

Property	Void (VGD_e) $\mu \pm \sigma_\mu$	Wall (WGD_e) $\mu \pm \sigma_\mu$	KS (P) Probability	[N_V, N_W]
$g-r$	0.774 ± 0.010	0.841 ± 0.002	$< 10^{-4}$	(351, 6691)
$u-g$	1.599 ± 0.020	1.711 ± 0.005	$< 10^{-4}$	(347, 6629)
$u-r$	2.357 ± 0.026	2.540 ± 0.006	$< 10^{-4}$	(345, 6590)
$r90/r50$	2.777 ± 0.015	2.838 ± 0.004	0.0001	(351, 6695)
n	2.567 ± 0.036	2.739 ± 0.002	$< 10^{-4}$	(315, 6695)

LIST OF SPECTROSCOPIC PROPERTIES FOR THE NEARBY SAMPLE

Table B.3: Means, errors on the means and KS test probabilities that the void and wall galaxies are drawn from the same parent population for the spectroscopic properties of void and wall galaxies in the nearby sample ($r < 72h^{-1}$Mpc). The number of galaxies (void and wall) in each sample and sub-sample are listed next to the magnitude range heading as [N_V (void), N_W (wall)]. Small values of P correspond to a low probability that the two samples are drawn from the same parent population. The KS test shows that void galaxies appear to have stronger emission line EWs than wall galaxies in all cases. The average difference between the means of the EWs and D_n4000s is about $2\sigma_\mu$. However, the SFRs and stellar masses are not significantly different. Only the bright void galaxy sub-sample shows a larger S-SFR(Hα) than wall galaxies.

Full ($-19.9 \leq M_r \leq -14.5$) [$N_V = 194$, $N_W = 2256$]

Property	Void (VGD) $\mu \pm \sigma_\mu$	Wall (WGD) $\mu \pm \sigma_\mu$	KS (P) Probability	[N_V, N_W]
EW(Hα) [Å]	35.31 ± 0.262	26.18 ± 0.645	0.0021	(187, 2202)
EW(Hβ) [Å]	7.317 ± 0.738	5.702 ± 0.242	0.0007	(192, 2226)
EW([NII]) [Å]	5.175 ± 0.338	4.298 ± 0.097	0.0611	(191, 2232)
EW([OIII]) [Å]	18.50 ± 2.111	14.17 ± 0.548	$< 10^{-4}$	(188, 2211)
$\mathrm{Log}_{10}(\mathrm{Mass}/M_\odot)$	8.692 ± 0.060	8.803 ± 0.018	0.0592	(194, 2256)
SFR(Hα) [$M_\odot/yr$]	0.162 ± 0.012	0.146 ± 0.006	0.3410	(183, 2020)
S-SFR(Hα) [yr^{-1}]	$(25.55 \pm 0.353) \times 10^{-11}$	$(31.70 \pm 0.169) \times 10^{-11}$	0.0001	(182, 2005)
D_n4000	1.261 ± 0.019	1.314 ± 0.005	$< 10^{-4}$	(119, 1545)

Bright ($M_r \leq -17.0$) [$N_V = 76$, $N_W = 1071$]

Property	Void (VGD_b) $\mu \pm \sigma_\mu$	Wall (WGD_b) $\mu \pm \sigma_\mu$	KS (P) Probability	[N_V, N_W]
EW(Hα) [Å]	33.316 ± 3.74	21.91 ± 0.809	0.0005	(76, 1060)
EW(Hβ) [Å]	5.939 ± 0.769	3.770 ± 0.210	0.0006	(76, 1055)
EW([NII]) [Å]	7.223 ± 0.733	5.203 ± 0.157	0.0034	(76, 1062)
EW([OIII]) [Å]	11.615 ± 2.41	8.276 ± 0.525	0.0133	(76, 1056)
$\mathrm{Log}_{10}(\mathrm{Mass}/M_\odot)$	9.333 ± 0.066	9.390 ± 0.018	0.4123	(76, 1071)
SFR(Hα) [$M_\odot/yr$]	0.323 ± 0.048	0.194 ± 0.011	0.0009	(73, 933)
S-SFR(Hα) [yr^{-1}]	$(17.57 \pm 3.222) \times 10^{-11}$	$(12.57 \pm 0.958) \times 10^{-11}$	$< 10^{-4}$	(73, 933)
D_n4000	1.287 ± 0.032	1.371 ± 0.008	$< 10^{-4}$	(50, 792)

Faint ($M_r > -17.0$) [$N_V = 118$, $N_W = 1185$]

Property	Void (VGD_f) $\mu \pm \sigma_\mu$	Wall (WGD_f) $\mu \pm \sigma_\mu$	KS (P) Probability	[N_V, N_W]
EW(Hα) [Å]	36.68 ± 3.60	30.14 ± 0.977	0.3740	(111, 1142)
EW(Hβ) [Å]	8.220 ± 1.111	7.443 ± 0.412	0.2920	(116, 1171)
EW([NII]) [Å]	3.821 ± 0.378	3.477 ± 0.121	0.4446	(115, 1170)
EW([OIII]) [Å]	23.17 ± 3.073	19.55 ± 0.905	0.0481	(112, 1155)
$\mathrm{Log}_{10}(\mathrm{Mass}/M_\odot)$	8.279 ± 0.060	8.273 ± 0.019	0.3589	(118, 1185)
SFR(Hα) [$M_\odot/yr$]	0.054 ± 0.006	0.098 ± 0.005	0.1725	(109, 1066)
S-SFR(Hα) [yr^{-1}]	$(29.19 \pm 4.527) \times 10^{-11}$	$(46.37 \pm 2.713) \times 10^{-11}$	0.0269	(109, 1066)
D_n4000	1.243 ± 0.022	1.253 ± 0.007	$< 10^{-4}$	(69, 753)

Late ($n < 1.8$) [$N_V = 167$, $N_W = 1817$]

Property	Void (VGD_l) $\mu \pm \sigma_\mu$	Wall (WGD_l) $\mu \pm \sigma_\mu$	KS (P) Probability	[N_V, N_W]
EW(Hα) [Å]	32.82 ± 2.613	25.75 ± 0.648	0.0367	(162, 1788)
EW(Hβ) [Å]	6.748 ± 0.755	5.165 ± 0.204	0.0060	(166, 1792)
EW([NII]) [Å]	4.610 ± 0.353	3.905 ± 0.090	0.1647	(165, 1801)
EW([OIII]) [Å]	16.49 ± 1.943	13.67 ± 0.554	0.0023	(162, 1791)
$\mathrm{Log}_{10}(\mathrm{Mass}/M_\odot)$	8.627 ± 0.061	8.698 ± 0.018	0.1116	(167, 1817)
SFR(Hα) [$M_\odot/yr$]	0.131 ± 0.018	0.139 ± 0.006	0.2801	(158, 1656)
S-SFR(Hα) [yr^{-1}]	$(23.42 \pm 3.245) \times 10^{-11}$	$(33.15 \pm 1.826) \times 10^{-11}$	0.0013	(159, 1658)
D_n4000	1.261 ± 0.017	1.278 ± 0.005	$< 10^{-4}$	(102, 1227)

Early ($n > 1.8$) [$N_V = 27$, $N_W = 439$]

Property	Void (VGD_e) $\mu \pm \sigma_\mu$	Wall (WGD_e) $\mu \pm \sigma_\mu$	KS (P) Probability	[N_V, N_W]
EW(Hα) [Å]	51.45 ± 9.494	28.03 ± 1.994	0.0165	(25, 414)
EW(Hβ) [Å]	10.96 ± 2.483	7.919 ± 0.901	0.0166	(26, 434)
EW([NII]) [Å]	8.759 ± 1.623	5.941 ± 0.341	0.1338	(26, 431)
EW([OIII]) [Å]	31.04 ± 9.042	16.29 ± 1.663	0.0035	(26, 420)
$\mathrm{Log}_{10}(\mathrm{Mass}/M_\odot)$	9.093 ± 0.171	9.237 ± 0.423	0.1640	(27, 439)
SFR(Hα) [$M_\odot/yr$]	0.364 ± 0.105	0.162 ± 0.016	0.1823	(24, 343)
S-SFR(Hα) [yr^{-1}]	$(31.82 \pm 8.411) \times 10^{-11}$	$(18.29 \pm 2.101) \times 10^{-11}$	$< 10^{-4}$	(24, 343)
D_n4000	1.263 ± 0.073	1.449 ± 0.017	$< 10^{-4}$	(17, 318)

LIST OF SPECTROSCOPIC PROPERTIES FOR THE DISTANT SAMPLE

Table B.4:

Means, errors on the means and KS test probabilities that the void and wall galaxies are drawn from the same parent population for the spectroscopic properties of void and wall galaxies in the distant sample ($100 \leq r \leq 260h^{-1}$Mpc). The number of galaxies (void and wall) in each sample and sub-sample are listed next to the magnitude range heading as [N_V (void), N_W (wall)]. Small values of P correspond to a low probability that the two samples are drawn from the same parent population. In this case, the KS test shows that the void and wall galaxies are drawn from different populations based on emission line EWs, stellar masses, Hα and [OII] derived SFRs and S-SFRs, and D_n4000. The differences between the means of the different parameters measured are on average $> 5\sigma_\mu$, except for the SFR(Hα) and SFR([OII]) in the faint sub-sample, where the difference is $\sim 2\sigma_\mu$. Void galaxies on average have higher S-SFRs, larger EWs, smaller stellar masses and smaller D_n4000.

Full ($-22.5 \leq M_r \leq -17.77$) [$N_V = 1010$, $N_W = 12732$]

Property	Void (VGD) $\mu \pm \sigma_\mu$	Wall (WGD) $\mu \pm \sigma_\mu$	KS (P) Probability	[N_V, N_W]
EW(Hα) [Å]	19.14 ± 0.680	11.77 ± 0.158	$< 10^{-4}$	(1005, 12636)
EW([OII]) [Å]	14.26 ± 0.395	9.441 ± 0.093	$< 10^{-4}$	(1006, 12301)
EW(Hβ) [Å]	2.571 ± 0.146	0.828 ± 0.035	$< 10^{-4}$	(997, 12544)
EW([NII]) [Å]	6.553 ± 0.181	5.065 ± 0.049	$< 10^{-4}$	(1006, 12586)
EW([OIII]) [Å]	4.694 ± 0.335	2.197 ± 0.061	$< 10^{-4}$	(994, 12373)
$\mathrm{Log}_{10}(\mathrm{Mass}/M_\odot)$	10.13 ± 0.015	10.43 ± 0.004	$< 10^{-4}$	(1010, 12732)
SFR(Hα) $[M_\odot/yr]$	0.734 ± 0.025	0.747 ± 0.007	$< 10^{-4}$	(850, 8930)
SFR($[OII]$) $[M_\odot/yr]$	0.448 ± 0.015	0.488 ± 0.006	$< 10^{-4}$	(841, 8764)
S-SFR(Hα) $[yr^{-1}]$	$(3.744 \pm 0.108) \times 10^{-11}$	$(2.629 \pm 0.034) \times 10^{-11}$	$< 10^{-4}$	(850, 8930)
S-SFR([OII]) $[yr^{-1}]$	$(4.892 \pm 0.890) \times 10^{-11}$	$(3.020 \pm 0.251) \times 10^{-11}$	$< 10^{-4}$	(841, 8764)
D_n4000	1.515 ± 0.011	1.649 ± 0.003	$< 10^{-4}$	(714, 9862)

Bright ($M_r \leq -19.5$) [$N_V = 409$, $N_W = 7831$]

Property	Void (VGD_b) $\mu \pm \sigma_\mu$	Wall (WGD_b) $\mu \pm \sigma_\mu$	KS (P) Probability	[N_V, N_W]
EW(Hα) [Å]	14.47 ± 0.932	8.542 ± 0.175	$< 10^{-4}$	(406, 7774)
EW([OII]) [Å]	9.338 ± 0.429	6.884 ± 0.089	$< 10^{-4}$	(399, 7548)
EW(Hβ) [Å]	1.246 ± 0.201	0.018 ± 0.038	$< 10^{-4}$	(401, 7699)
EW([NII]) [Å]	6.606 ± 0.332	4.711 ± 0.066	$< 10^{-4}$	(407, 7743)
EW([OIII]) [Å]	2.706 ± 0.531	1.172 ± 0.055	$< 10^{-4}$	(401, 7574)
$\mathrm{Log}_{10}(\mathrm{Mass}/M_\odot)$	10.52 ± 0.016	10.70 ± 0.004	$< 10^{-4}$	(409, 7831)
SFR(Hα) $[M_\odot/yr]$	1.136 ± 0.063	0.920 ± 0.016	$< 10^{-4}$	(306, 4956)
SFR([OII]) $[M_\odot/yr]$	0.736 ± 0.051	0.626 ± 0.013	$< 10^{-4}$	(304, 4876)
S-SFR(Hα) $[yr^{-1}]$	$(3.133 \pm 0.169) \times 10^{-11}$	$(2.137 \pm 0.004) \times 10^{-11}$	$< 10^{-4}$	(306, 4956)
S-SFR([OII]) $[yr^{-1}]$	$(3.061 \pm 0.279) \times 10^{-11}$	$(2.192 \pm 0.053) \times 10^{-11}$	$< 10^{-4}$	(304, 4876)
D_n4000	1.602 ± 0.017	1.711 ± 0.004	$< 10^{-4}$	(287, 6069)

Faint ($M_r > -19.5$) [$N_V = 601$, $N_W = 4901$]

Property	Void (VGD_f) $\mu \pm \sigma_\mu$	Wall (WGD_f) $\mu \pm \sigma_\mu$	KS (P) Probability	[N_V, N_W]
EW(Hα) [Å]	22.31 ± 0.929	16.93 ± 0.287	$< 10^{-4}$	(599, 4862)
EW([OII]) [Å]	17.57 ± 0.554	13.50 ± 0.178	$< 10^{-4}$	(593, 4753)
EW($H\beta$) [Å]	3.452 ± 0.202	2.095 ± 0.067	$< 10^{-4}$	(531, 4334)
EW([NII]) [Å]	6.517 ± 0.204	5.630 ± 0.074	$< 10^{-4}$	(599, 4843)
EW([OIII]) [Å]	6.038 ± 0.423	3.817 ± 0.128	$< 10^{-4}$	(593, 4799)
$\mathrm{Log}_{10}(\mathrm{Mass}/M_\odot)$	9.873 ± 0.015	10.02 ± 0.005	$< 10^{-4}$	(601, 4901)
SFR(Hα) $[M_\odot/yr]$	0.508 ± 0.0237	0.530 ± 0.009	0.0254	(544, 3974)
SFR([OII]) $[M_\odot/yr]$	0.286 ± 0.017	0.316 ± 0.007	0.0298	(537, 3888)
S-SFR(Hα) $[yr^{-1}]$	$(4.146 \pm 0.137) \times 10^{-11}$	$(3.349 \pm 0.005) \times 10^{-11}$	$< 10^{-4}$	(544, 3974)
S-SFR([OII]) $[yr^{-1}]$	$(5.725 \pm 1.375) \times 10^{-11}$	$(4.058 \pm 0.147) \times 10^{-11}$	0.0034	(537, 3888)
D_n4000	1.456 ± 0.013	1.551 ± 0.004	$< 10^{-4}$	(427, 3793)

Late ($n < 1.8$) [$N_V = 659$, $N_W = 6037$]

Property	Void (VGD_l) $\mu \pm \sigma_\mu$	Wall (WGD_l) $\mu \pm \sigma_\mu$	KS (P) Probability	[N_V, N_W]
EW(Hα) [Å]	23.95 ± 0.771	20.15 ± 0.226	$< 10^{-4}$	(658, 6002)
EW([OII]) [Å]	16.99 ± 0.458	13.73 ± 0.139	$< 10^{-4}$	(655, 5950)
EW($H\beta$) [Å]	3.778 ± 0.155	2.831 ± 0.047	$< 10^{-4}$	(652, 5956)
EW([NII]) [Å]	7.615 ± 0.200	7.211 ± 0.065	0.01955	(658, 5992)
EW([OIII]) [Å]	5.272 ± 0.413	3.435 ± 0.089	$< 10^{-4}$	(655, 5957)
$\mathrm{Log}_{10}(\mathrm{Mass}/M_\odot)$	10.02 ± 0.017	10.20 ± 0.006	$< 10^{-4}$	(659, 6037)
SFR(Hα) $[M_\odot/yr]$	0.654 ± 0.028	0.793 ± 0.012	0.0013	(622, 5316)
SFR([OII]) $[M_\odot/yr]$	0.478 ± 0.025	0.571 ± 0.009	0.0002	(621, 5304)
S-SFR(Hα) $[yr^{-1}]$	$(4.495 \pm 0.114) \times 10^{-11}$	$(3.928 \pm 0.04) \times 10^{-11}$	0.0133	(622, 5316)
S-SFR([OII]) $[yr^{-1}]$	$(5.488 \pm 1.191) \times 10^{-11}$	$(3.872 \pm 0.069) \times 10^{-11}$	0.0324	(621, 5304)
D_n4000	1.399 ± 0.087	1.449 ± 0.027	$< 10^{-4}$	(463, 4676)

Early ($n > 1.8$) [$N_V = 351$, $N_W = 6695$]

Property	Void (VGD_e) $\mu \pm \sigma_\mu$	Wall (WGD_e) $\mu \pm \sigma_\mu$	KS (P) Probability	[N_V, N_W]
EW(Hα) [Å]	10.01 ± 1.18	4.189 ± 0.176	$< 10^{-4}$	(347, 6634)
EW([OII]) [Å]	8.944 ± 0.657	5.420 ± 0.099	$< 10^{-4}$	(337, 6351)
EW($H\beta$) [Å]	0.289 ± 0.261	-0.982 ± 0.039	$< 10^{-4}$	(345, 6588)
EW([NII]) [Å]	4.546 ± 0.337	3.115 ± 0.065	$< 10^{-4}$	(348, 6594)
EW([OII]) [Å]	3.576 ± 0.570	1.048 ± 0.082	$< 10^{-4}$	(339, 6416)
$\mathrm{Log}_{10}(\mathrm{Mass}/M_\odot)$	10.35 ± 0.022	10.65 ± 0.005	$< 10^{-4}$	(351, 6695)
SFR(Hα) $[M_\odot/yr]$	0.433 ± 0.058	0.369 ± 0.015	0.0456	(228, 3614)
SFR([OII]) $[M_\odot/yr]$	0.364 ± 0.047	0.360 ± 0.014	$< 10^{-4}$	(220, 3460)
S-SFR(Hα) $[yr^{-1}]$	$(1.801 \pm 0.189) \times 10^{-11}$	$(1.015 \pm 0.005) \times 10^{-11}$	0.0883	(228, 3614)
S-SFR([OII]) $[yr^{-1}]$	$(2.711 \pm 0.331) \times 10^{-11}$	$(1.713 \pm 0.145) \times 10^{-11}$	$< 10^{-4}$	(220, 3460)
D_n4000	1.728 ± 0.015	1.830 ± 0.003	$< 10^{-4}$	(251, 5186)